Dielectrophoresis of human tumor spheroids on a microfluidic chip

TECHNISCHE UNIVERSITÄT WIEN

Diploma Thesis

Dielectrophoresis of human tumor spheroids on a microfluidic chip

under supervision of

Ao. Univ. Prof. Dipl.-Ing. Dr. techn. Wanzenböck Heinz

Univ. Ass. in Dr.in Prado Lopez Sonia

by

Max Schimpf

12009669

……. …….

Wanzenböck Heinz Prado Lopez Sonia

TECHNISCHE UNIVERSITÄT WIEN

Affidavit

I have taken note that I am only authorized to publish my work under the designation:

Diploma-Thesis (Diplomarbeit)

with the approval of the examination committee. I solemnly declare that the present work was created by myself independently, with the assistance of artificial intelligence as for the state of today no regulations for the use of AI exist. This work was created in accordance with the recognized principles for academic papers. All used resources, especially the underlying literature, are mentioned and listed in this work. The passages taken verbatim from the sources are clearly identified as such.

The topic of this work has not been submitted for evaluation in any form as an examination paper, neither domestically nor internationally, by any examiner. This work corresponds to the work evaluated by the examiners.

I acknowledge that the submitted work will be electronically and technically reviewed using appropriate tools, including plagiarism detection software, in line with the current state of technology. This ensures, on one hand, that the high quality standards within the framework of the applicable rules for safeguarding good scientific practice, "Code of Conduct" at TU Wien, have been adhered to in creating the submitted work. On the other hand, by comparing with other student theses, violations of my personal copyright are avoided.

28.8.2023 *Max Schimpf*

Giving Thanks

First, I want to express my gratitude to Professor Heinz Wanzenböck, you were a true guiding light on my research journey. My deepest gratitude for your unwavering support, boundless patience, and all the hours of training and teaching within the clean room. I am truly grateful for your support and guidance.
Secondly, I want to thank Prof. Sonia Prado Lopez for your expertise, help, and the provision of biological samples. I truly enjoyed the experiments with you in the laboratory.
Appreciated also are the members of the Biomedical Microsystems Group. Without you, this thesis wouldn't have been a success.
Furthermore, I am thankful to Heinz Redl, for opening my eyes to the vast possibilities of dielectrophoresis in microfluidic. And let us not forget Peter Ertl, who introduced me to lab-on-a-chip technology.

Next, I want to appreciate my family, especially my ever-loving mother, Tatiana; your unwavering support carried me through the many challenges of life. I would like to thank my girlfriend, Sonja; your presence has prevented me from overworking and provided care during stressful situations. I also want to express my gratitude to my brother Christian; you serve as a reminder of life's true priorities, and you bring so much joy through all your entertaining ways. As I delve further into this thesis, I am driven by the desire to articulate my thoughts in a way that all of you can understand.

Lastly, I will use this opportunity to advise future readers. Feel free to use the information gathered in this thesis to follow your passions to ignite a sense of purpose within you.

Dedicate time and explore creation.

"The only way to do great work is to love what you do." - Steve Jobs.

Abstract

In the last few years, *spheroids* and *organoids* have significantly improved the accuracy and convenience of *in vitro* studies compared to conventional cell monolayers and animal models. *Spheroids* are three-dimensional cell aggregates that closely mimic the characteristics of tumors in the human body, making them valuable tools for studying cancer biology and testing potential therapies. *Organoids* are *in vitro* 3D cell culture micro physiological systems of organ-like structures. *Spheroids* and *Organoids,* and their electrophysiological reaction to therapies or conditions are usually recorded via integrated electrodes.

In this thesis, the potential application of dielectrophoresis in positioning *human tumor spheroids* via these integrated electrodes is presented. "Dielectrophoresis" is the movement of particles based on their insulating properties in an inhomogeneous field. Positioning *human tumor spheroids* using dielectrophoresis can become an additional tool in automated cell cluster manipulation. Furthermore, being able to precisely position *human tumor spheroids* on biological activity recording electrodes using dielectrophoresis can enhance our understanding of tumor behavior and improve the development of personalized cancer treatments. The current problem is that *human tumor* spheroids placement on sensing electrodes is difficult, as the electrodes are specifically located, and the *human tumor spheroids* are arranged randomly in cell media on top of the chip. Therefore, the question asked in this study is whether DEP has a sufficient translational effect on *human tumor spheroids* and can be effectively used to selectively micro-position them. To answer these questions, simulations and experiments were conducted utilizing specifically developed tools. Glass wafer hosted electrodes created through photolithography, on top of the electrode glass substrate were lab-on-a-chip devices manufactured using PDMS casting and Xurography techniques. Frequency generators were interlinked to the lab-on-a-chip via tailor-made adapters. Subsequently *human tumor spheroids* were introduced into the apparatus, a predetermined electric field frequency spectrum was applied and the dielectrophoresis of *human tumor spheroids* was subsequently examined. The results of the study revealed key findings, which include the successful movement of *human tumor spheroids* using DEP, but also side appearances like electrolysis.

At 2 MHz and 10 V a successful DEP positioning of approx. 150 µm big human tumor spheroids between 300µm distant electrodes was achieved. This study concludes that DEP can be an effective solution for positioning *human tumor spheroids* on electrodes, which opens possibilities to improve further research and advancements in cancer diagnostics and therapeutics.

Kurzfassung

In den letzten Jahren haben Sphäroide und Organoiden die Genauigkeit und Bequemlichkeit von *In-vitro*-Studien im Vergleich zu herkömmlichen Zell- und Tierversuchen erheblich verbessert. Sphäroide sind dreidimensionale Zellaggregate, die den Eigenschaften von Tumoren im menschlichen Körper sehr nahekommen und somit wertvolle Forschungssubjekte für die Krebsforschung und Testung potentieller Therapien darstellen. Organoide sind ebenfalls in-vitro-3D-Zellkulturen, die organähnliche Strukturen bilden und als vergleichende mikrophysiologische Systeme dienen. Die elektrophysiologische Reaktion der 3D-Zellkulturen auf verschiedene Therapien und Zustande wird meistens über integrierte Elektroden aufgezeichnet.

In dieser Diplomarbeit wird die potentielle Anwendung der Dielektrophorese zur Positionierung von menschlichen Tumorsphäroiden mittels diesen integrierten Elektroden vorgestellt. "Dielektrophorese" ist die Bewegung von Partikeln aufgrund ihrer elektro-physikalischen Eigenschaften in einem inhomogenen Feld. Die Positionierung von menschlichen Tumorsphäroiden mittels Dielektrophorese kann ein zusätzliches Werkzeug zur automatischen Manipulation von 3D-Zellkulturen sein. Darüber hinaus kann die präzise Positionierung dieser Sphäroide auf Elektroden mittels DEP unser Verständnis des Verhaltens von Tumoren verbessern und die Entwicklung personalisierter Krebstherapien vorantreiben. Das aktuelle Problem ist, die Platzierung der Sphäroide auf den Fingern der Sensorelektroden, da die Elektroden spezifisch positioniert sind und die Sphäroide sich zufällig auf dem Chip anordnen. Daher lautet die Fragestellung in dieser Studie, ob DEP eine ausreichende translatorische Wirkung auf Sphäroide hat und effektiv zur selektiven Mikropositionierung verwendet werden kann. Um diese Fragen zu beantworten, wurden Simulationen und Experimente durchgeführt. Auf Glass Chips wurden Elektroden Micro fabriziert, mittels Photolithographie. Aus diesem Chips wurden Lab-on-a-Chip-Plattformen mit Hilfe von PDMS und Xurographie-Techniken hergestellt. Die Frequenzgeneratoren wurden dann über speziell angefertigte Adapter mit dem Lab-on-a-Chip verbunden. Anschließend wurden Sphäroide in die Vorrichtung eingebracht und ihre dielektrische Bewegung über ein vordefiniertes Frequenzspektrum unter mikroskopischer Beobachtung untersucht. Die Ergebnisse der Studie zeigen neue wichtige Erkenntnisse, darunter die erfolgreiches rollen von Sphäroiden mittels Dielektrophorese, aber auch unerwünschte Nebeneffekte wie Elektrolyse in bestimmten Frequenzbereichen. Bei 2 MHz und 10 V wurde eine erfolgreiche DEP-Positionierung von ca. 150 µm großen menschlichen Tumor-Sphäroiden zwischen 300 µm entfernten Elektroden erreicht. Das Fazit dieser Studie ist, dass die Dielektrophorese eine wirksame Lösung zur Positionierung von menschlichen Tumorsphäroiden auf Elektroden ist, was Möglichkeiten eröffnet, weitere Forschung zu verbessern.

Table of contents

1. Introduction

"The most incomprehensible thing about the world is that it is comprehensible." - Albert Einstein. The major topics such as dielectrophoresis (DEP), multi-electrode arrays (MEA), and *spheroids* are comprehensively introduced along with the motivation, research question, and experimental approach.

Herbert A. Pohl discovered in 1978, translational and oriental behavior of neutral particles inside a non-uniform electric field and termed it "dielectrophoresis".[1] The term "dielectrophoresis" itself is derived from the combination of two terms: "dielectric" and "phoresis." "dielectric" refers to the insulating properties of a material, while "phoresis" refers to movement or transport. DEP has been widely used for microfluidic separation of cells based on their dielectric properties like membrane capacitance and conductivity within the cell.[2] Microfluidics is the science of small amounts of liquids in laminar flow. It has been employed for a considerable amount of time in microfluidic devices known as Lab-on-a-Chip (LoC) for biological and chemical analyses.[3] Even though DEP techniques are already in use, applying dielectrophoresis to *human cell spheroids* or *organoids* is new.

Spheroids are 3-dimensional aggregates composed of single cell types while *organoids* are growing cell clusters that are able to self-organize in laboratory conditions outside the human body and differentiate into a variety of functional cell types, mimicking the 3D structure and function of an organ.[4] They are rapidly gaining importance in research because they can be utilized for fundamental investigations on human tissue formation, regeneration, repair, drug discovery, disease modeling, and personalized medicine.[5] A related approach to imitate the 3D structural functions of organs are organ-on-a-chip (OoC) platforms. These are platforms that involve the generation of tissue inside a microfluidic chip.[6] OoC with *organoid* technology results in organoid-on-a-chip platforms, microfluidic cell culture devices, designed to model the functional units of human organs.[7] These devices often include integrated MEA, for cellular activity measurement with bioelectronic means.[8]

MEA and interdigitated electrodes (IDEs) were previously utilized to measure the cellular activity of conventional 2D cell cultures. [9-10] To measure the cellular activity of 3D-cell-cluster-cultures, they need to be positioned on the electrode fingers for measurement. The common solution is positioning by size restriction in around 250 µm wide wells [8]. However, this method carries poor accuracy with smaller-sized *spheroids* and requires the spheroid to fall into the well. More complicated ways include forming either a cave with electrodes[11] to place the *spheroids* in or self-folding electrodes around *organoids* termed “shell MEA”[12]. In these cases, the cell cluster can’t easily be retrieved for later analyses. To improve these measurements, micro-positioning cell clusters directly on the electrode fingers of an MEA by DEP is investigated. Therefore, the objective of this study is to explore the feasibility of utilizing dielectrophoresis techniques on *human tumor cell spheroids*.

The motivation behind the study is that dielectrophoretic micropositioning *spheroids* on electrodes can not only enhance *spheroid* impedance measurements but become an additional automation tool for high-throughput microprocessor-controlled machines[13] for cancer therapeutic evaluation in tumor sensitivity studies and genetic therapy trials. The device could be reused, reducing waste products, and improving laboratory sustainability. An additional incentive of this study is achieving size exclusion which could likely later enable the distinction between *spheroid* mutants and non-mutants by fine-tuning the frequency of the applied DEP field, as already realized with *E. coli*.[14]

But first, the fundamentals of *spheroid* dielectrophoresis must be established. Therefore, the research questions of this study are:

- **Does DEP have a sufficient translational effect on *spheroids*?**
- **Is it feasible to micro-position *spheroids*?**
- **Are *spheroids* of a certain size selectively influenced by DEP?**

The experimental approach can be quite challenging as all proteins and cells of any size and composure as well as their by-products are affected by direct current DEP[15] and by contact change the electrode surface confirmation and resulting field. To prevent this, alternating current (AC) is used. A biophysical mathematical model can determine a specific separation frequency that corresponds only to the electro-physical parameter of interest, which may include cell size, membrane, and cytoplasmic composition. The resultant alternating current field at a specific frequency already enables the possibility to selectively separate a cell from its mutant.[14] This observation leads to the assumption that a frequency may exist that specifically induces responses to spheroids of particular sizes. Considering this, the hypothesis is formulated: DEP can significantly positively deflect *spheroids* of a certain size, by using an electric AC field at a certain frequency generated at the electrodes of a MEA. A mathematical model based on the electrophysiological *spheroid* parameter is used to guide the design and fabrication of a DEP device. *Spheroid* dielectrophoresis via integrated electrodes is investigated by establishing a frequency generator connection and recording the resulting motion via microscope.

2. Theoretical Foundations

"The greatest enemy of knowledge is not ignorance; it is the illusion of knowledge." - Stephen Hawking. This chapter provides an overview of the current knowledge of dielectrophoresis as the main separation principle, *spheroids* as a research subject, and lab-on-a-chip technology as a research platform.

2.1 Dielectrophoresis

Dielectrophoresis is the manipulation of particles in an inhomogeneous electric field. It finds application in biomedicine as it can be used for organic samples. This technique's core principle of differential handling allows precise sorting and isolation of specific particles, making it the fundamental method in the separation processes of *human cell spheroids*. The phenomena can be described as a translational force, known as the dielectrophoretic force (1), whose magnitude and direction depend on the electrical properties of the particle and its surrounding medium. This force also depends on the magnitude and frequency of the applied electric field. [14] For spherical particles the time-average DEP Force is [16]

$$F_{DEP} = 2\pi r^3 \varepsilon_0 \varepsilon_m Re[K(\omega)] \nabla |E_{rms}|^2, \tag{1}$$

Where:

- r is the particle radius. [m]
- ε_0 is the permittivity of free space: $8{,}854 * 10^{-12}$ $[F/m]$.
- ε_m is the real part of the permittivity of the suspending medium: $\mathrm{Re}(\varepsilon_m) = \frac{\varepsilon_m + \overline{\varepsilon_m}}{2}$ $[F/m]$.
- E_{rms} is the root-mean-square of the electric field at a certain position. [V/m]
- $K(\omega)$ (Clausius-Mossotti factor) depends on the complex permittivity of both the particle and the surrounding medium. It is a measure of the effective polarizability of the particle. In the case of spherical particles, this factor is given by:

$$K(\omega) = \frac{(\varepsilon_p^* - \varepsilon_m^*)}{(\varepsilon_p^* + 2\varepsilon_m^*)}$$

$$\varepsilon_{i\,(i=p,m)}^* = \varepsilon_i - j\frac{\sigma_i}{\varepsilon_0 \omega}, \tag{2,3}$$

Where:

- Indices refer to the particle (p) and the medium (m), respectively.
- ε and σ are, respectively, the permittivity $[F/m]$ and the conductivity [S/m] of the dielectric.
- ω is the angular frequency of the applied electric AC field *(ω=2πf),* and $j = \sqrt{-1}$.

Two different experimental conditions can be established. **When $Re[K(\omega)] > 0$, the particles move toward regions with maximum electric field density. This phenomenon is called positive dielectrophoresis (p-DEP). Alternatively, when the particle polarizability is low enough that $Re[K(\omega)] < 0$ becomes negative, then the particles move towards regions with minimum electric field density. This case is called negative dielectrophoresis (n-DEP).**[14] Positive and negative DEP is often employed for the effective movement of biological samples, such as *spheroids* in the thesis.

2.2 Spheroids and Organoids

Figure 1: Artistic Illustrations of a Spheroid (Left) and an Organoid (Right) designed by DALL-E (OpenAI). The spheroid represents the aggregation of single cells, while the organoid represents natural self-organized growth.

The advent of *induced pluripotent stem cells* (*iPSC*) derived from somatic cells like *adult human dermal fibroblasts* with the so-called "Yamanaka factors" (Oct3/4, Sox2, Klf4, and c-Myc) eased the overall generation of *in vivo* tissue-like cell arrangements.[17] Further innovations in biomaterials have enabled the creation of complex 3D structures such as *spheroids* and *organoids*, which have significantly improved the accuracy and convenience of in vitro studies compared to conventional cell monolayers and animal models.[18] Illustrations for spheroids and *organoids* are provided in Fig. 1.

Spheroids are multicellular, three-dimensional aggregates consisting of a single cell type and allow studying interactions between cells and the extracellular matrix (ECM) *in vitro*.[4] Aggregation methods include cultivation on non-adherent substrates, cultivation in a rotating spinner flask, hanging drop method, and mixing with magnetic nanoparticles.[18] To achieve high density packing acoustic waves can be utilized to push the cells into 3D-printed micro cages.[19] Furthermore, Jin. H. J. et al have shown for the first time that forming a spheroid can also take place inside a lab-on-a-chip. [20]

Organoids are *in vitro* 3D cell culture micro physiological systems of organ-like structures.[17] They follow intrinsic developmental programs and develop from self-organizing stem cells to reproduce the key structural and functional properties of their *in vivo* counterparts.[7] They can contain multiple cell types and range in size between 0.1 to 1 mm (often non-spherical).[4] There are several methods used to create *organoids*, including the use of extracellular matrix scaffolds, spinning bioreactors, the hanging drop method, and microfabrication techniques such as micropatterning and microfluidics. Each method provides a unique environment that allows cells to self-organize and form complex structures that resemble specific organs.[18]

Alternative methods for characterizing and analyzing 3D spheroids and organoids, beyond conventional microscopic techniques, are examined in the subsequent section. It encompasses the utilization of electrophysiological, bioelectrical, and biophysical approaches, through the application of multielectrode arrays for recording and sensing.

2.3 Multi-Electrode Arrays

Bioelectrical changes in cultured cells can be assessed by utilizing micro-structured electrodes that are deposited onto a glass substrate. This approach allows for the measurement of potential alterations of adjacent fields and sensing modifications in the electrical properties of the cell culture.[9] Gold (Au) is often the electrode metal of choice due to its exceptional corrosion resistance. Cell to cell interactions can be measured with a special type of MEA called interdigitated electrodes (IDEs) which are utilized for precise impedance measurements between electrode finger pairs.[10] Interdigitated electrodes are a microelectrode structure of two or more sets of parallel electrodes that are interdigitated with each other. Each set of electrodes is separated by a small gap typically with widths ranging from tens to hundreds of micrometers. Combining MEA with DEP can be used for the movement and positioning of cells.[21] Furthermore the electrodes can be utilized for stem cell sorting.[22]

MEA are micro-structured metal electrodes on a chip. Just like computer processor microchips, they can be fabricated via a combination of photolithography, sputtering, plasma-enhanced chemical vapor deposition (PECVD), and reactive ion etching (RIE). The process begins with a clean glass wafer or glass substrate. The finished electrodes on the glass wafer consist of a thin film of sputtered gold.

Sputtering is a process where high-energy ions, typically derived from a gas like argon, collide with a solid material like gold, chromium, and others in a vacuum chamber. This collision causes atoms or ions from the target material to be emitted or sputtered. The sputtered atoms or ions then travel through the chamber and deposit onto a substrate like glass or silicon to form a thin metal film layer. To enhance the bonding of metals like gold, which doesn't adhere well to glass, chromium or titanium is sputtered first onto the glass as an adhesion supporter for the electrode gold layer.[23] Photolithography is a process that transfers the micro- to nanostructure patterns onto the substrate surface. It involves coating the substrate with a photosensitive material called photoresist. The photoresist is then exposed to light through a mask that contains the desired electrode pattern. By utilizing temperature, light, and developer solution chemical changes take place. As a result, the photoresist can be selectively removed, to create a desired pattern. For example, in an etching step, the previously deposited chromium adhesion support can be selectively removed by utilizing a developed photoresist protection layer for areas that should not encounter the oxidizing remover. There are several photolithography procedures. The process most used in this study for microfabrication is an “image reversal” process. In this process, a negative image of the desired electrode pattern is created with a photoresist. In other words, at the location where the electrodes are supposed to be, the surface shall be photoresist-free. When a thin film of e.g., gold is deposited on top of the patterned wafer, the film adheres to the previously deposited adhesion supporter and the photoresist on the glass wafer. During the “lift-off” step, the photoresist is dissolved using a suitable solvent like acetone, and the adhered gold on top of the photoresist gets removed. Only in areas without photoresist, a thin gold layer remains, and the electrode structure is created. After structuring the Au electrodes by a “lift-off” process, the chip surface is free of photoresist and can be further structured. The structure can be selectively insulated using PECVD (Plasma-Enhanced Chemical Vapor Deposition), a process involving plasma generated from gases like silane (SiH4) and a back etching process. The plasma reacts and forms a thin film over the entire surface, which is then etched back to leave the film only on desired areas of the electrodes. In conjunction with photolithography, this film removal process can be precisely controlled. As a result, the designated regions of the electrode structure are once again accessible for connections with voltage and/or cells. This capability of integrating microelectrodes finds particular significance in applications such as lab-on-a-chip platforms

2.4 Lab-on-a-chip

The shift from traditional laboratory-based diagnostics to point-of-care (PoC) settings in the last few years took place due to advantages like miniaturization, portability, integration, and automated processing of multiple assays.[24] The class of these PoC devices is the lab-on-a-chip technology. This technology integrates laboratory functions, such as sample preparation, analysis, and detection, onto a single microchip by utilizing microfluidics. Microfluidics is the analysis of small microliter volumes at specific rates in microchannels, where fluid mechanical effects can be employed. Due to a low Reynolds number associated with small dimensions, laminar flow is prevalent, the fluid flows without turbulences in parallel lines with little to no mixing between them.[25] The high surface-to-volume area inside the microfluidic channel can then be employed for fast efficient mixing or accurate molecule detection. This is due to the increased interaction between the fluid and the microchannel walls. Furthermore, inside the device cell cultures can be cultivated for diagnostics. The utilization of DEP analysis within a PoC framework is also a viable option. Imagine a visit to the doctor's office where you provide a liquid biopsy sample. This sample is inserted into a microfluidic device. The device adeptly isolates circulating tumor cells from the sample and positions them within specialized pockets. Subsequently, these cells are subjected to a variation of tests involving various medications, all while sensors surrounding the pockets meticulously monitor the tumor's response. This innovative approach, merging the power of liquid biopsy with advanced microfluidics, presents a transformative way to enhance medical diagnostics. Therefore, it's worth investigating if DEP can be applied to spheroids in microfluidic flow. However, Microfluidics plays a secondary role in this study because free fluidic flow separation of *spheroids* won't directly answer any of the thesis objectives but might be valuable for later high throughput or continuous applications. Even though the development of a microfluidic chip is necessary as these devices provide the platform for investigating DEP of human tumor spheroids by establishing an enclosure for the *spheroid* containing fluid.

Additionally, to in section 2.2 explained *spheroid* aggregation methods, capturing *hMSCs* and cultivating them in dimensional restrictions of a microfluidic chip can be employed to generate *spheroids* within a chip.[20] This device can be linked to a device fabricated from the outcome of this study like e. g. an automated sensitivity testing device explained before. It's important to note that LOC technology encompasses not only *spheroids* or cells but also *organoids*. This LOC technology in combination with *organoid* knowledge has the potential of creating tissue-like structures resembling organs directly within a microfluidic chip. These devices are referred to as "organ-on-a-chip" platforms and will be introduced in the following section.

2.5 Organ-on-a-chip

Introducing a brief digression on the significance of *organoids* within the context of Lab on a Chip technology. On December 29, 2022, President Biden signed into law the FDA Modernization Act 2.0. He approved that studies with validated organ-on-a-chip devices are equal to animal testing.[26] Organ-on-a-chip is a technology that consists of a micro-physiological system within an *in vivo-like* microenvironment designed for the specific research of (human) organ activity at the smallest level.[27] Cell culture microsystems and microfluidic are combined to mimic the absorption, distribution, metabolism, and excretion (ADME) of the corresponding organ-vesicle interaction. The microfluidic channel in the chip mimics the microenvironment of an organ, by providing nutrients and oxygen to the *organoid* and removing its waste. This enables the study of organ-tissue physiology and response to external stimuli, such as drugs or toxins.[6] OoC devices hold the potential for automated toxicological studies and can be mass-produced. Therefore, they are more cost- and time-effective than animal testing by trained lab personnel. Typically, they emulate the characteristics of a single organ, although it is also possible to model interactions between different organs. [28] Organ-on-a-chip technology generally relies on the current knowledge of human organs, to engineer constructs in which cells and their microenvironment are precisely controlled.[7] Unlike *organoids* these tissues inside the devices are not assembled by cellular self-organization, but the constructs in the chip assist *organoid* or specific tissue formation.

Organoids can be generated externally, and inserted in a microfluidic chip for further cultivation which results in the creation of an organoid-on-a-chip platform with improved differentiation for the study of certain diseases, like e.g. Parkinson's.[8] The microfluidic channel mimics a microvascular hydrostatic pressure-driven fluid flow such as blood and lymphatic 3D microcapillaries.[29] By the precise control of small samples in microfluidic, complex laboratory processes with *organoids* can then be automated inside an incubator.[13]

This study prioritizes *spheroids* over *organoids*, despite acknowledging the potential for extending this technology. The finalized techniques developed from this study could be interconnected with organoids as well. Following the introduction of all the subjects encompassed by this study, the existing advancements or state-of-the-art in these domains are now being elucidated.

3. State-of-the-Art Literature Review

"The task is ... not so much to see what no one has yet seen; but to think what nobody has yet thought, about that which everybody sees." - Erwin Schrodinger. To date, there is limited evidence suggesting the utilization of dielectrophoresis of *organoids* or *spheroids*, potentially attributed to their relatively recent emergence in the scientific research field. [18] Given this context, the central aim of this thesis is to address this research gap by investigating the role of DEP in the research domain of organoids and spheroids. To achieve this objective, it becomes essential to draw insights from similar approaches involving single cells, particles, and related entities. These parallels not only provide valuable information but also play a pivotal role in shaping devices and creating an effective methodology for studying the influence of DEP on *human tumor cell spheroids*.

3.1 Similar Approaches

In 2021 Giesler et al. published a paper about separating microparticles by material and size using dielectrophoretic chromatography. In traditional chromatography, the separation of particles is achieved based on the differential interaction of components with a stationary phase and a mobile phase. This separation approach contains a polydimethylsiloxane (PDMS) layer above the electrodes to stop particles from getting stuck between the electrodes because, at a constant applied high voltage field, no particles would exit the channel. Therefore, they incorporated a MATLAB script to switch the electrodes on and off and enhance the mobility of the particles and by that improve the separation.[30] To prevent this, the current study employs a two-channel separation system was incorporated in the design.

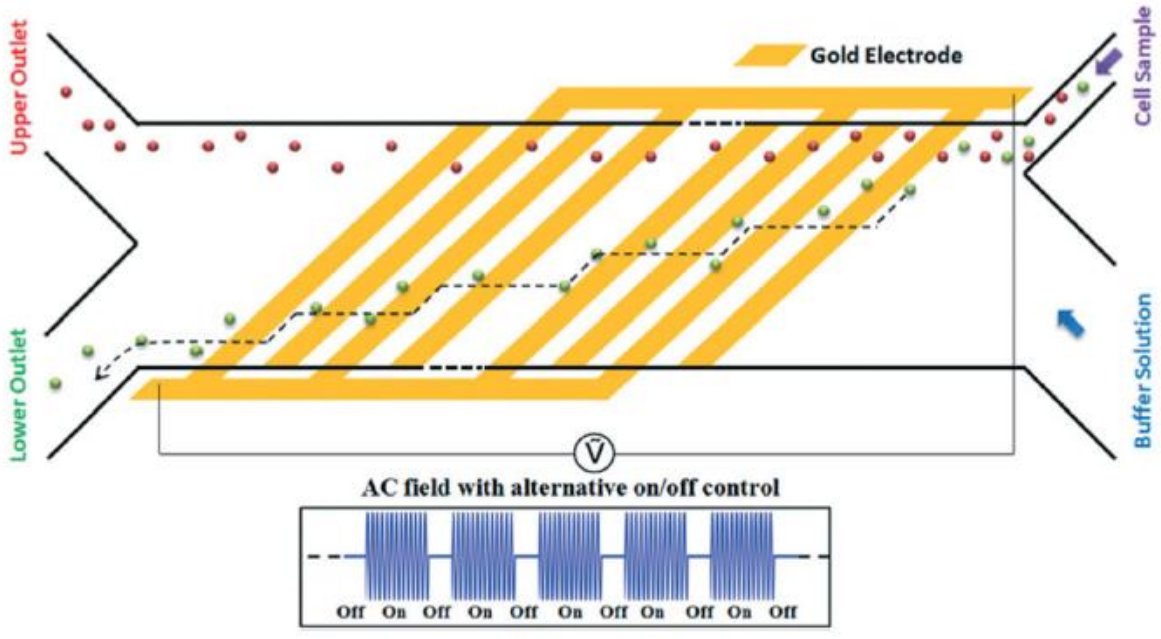

Figure 2: The microfluidic single-cell separation system schematic by Song. et al. employs a microchannel with alternating size inlets for cell sample and buffer solution, as well as outlets. Inside the microchannel, there's an array of inclined interdigitated electrodes with a 50µm gap in between (45° angle to flow direction). These electrodes generate a 1-second pulse DEP using an alternating AC field for separation. [31]

Transitioning from microparticles to single cells leads to the information that the basic DEP movement of biological cells is already industrialized by utilizing a three-dimensional grid system.[21] Furthermore, Song et al. already established the feasibility of the microfluidic DEP sorter for continuous, label-free sorting of *hMSCs* and their differentiation products.[31] Their schematic is visible in Fig. 2. Similar results were accomplished by D. Lee et al. what he termed "dielectrophoresis activated sorting". They achieved cell sorting using a traveling wave dielectrophoresis.[32] Another lab-on-a-chip liquid biopsy device successfully separated protein-labeled breast cancer cells with planar interdigitated transducer electrodes.[33]

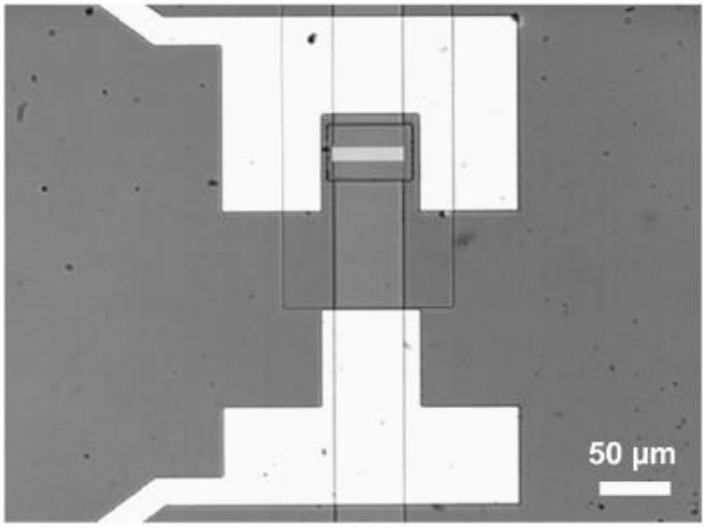

Figure 3: Optical microscopy image of a pair of electrodes arranged in both U- and T-configurations, designed for cell manipulation using DEP by Castellarnau et al. to distinguish isogenic E.coli. based on their electrophysiological properties.[14]

Castellarnau et al. demonstrated that an electric field at certain frequencies can label-free distinguish different mutants of *Escherichia coli (E. coli.)*, based on their membrane or cytoplasmic electrophysiological properties.[14] The electrode structure visible in Fig. 3, shows an electric field density variation by employing shapes with edges. However, these works concentrate on single cells, not three-dimensional cell culture microstructures. For cell cluster, C. I. Trainito et al. accomplished trapping of a *spheroid* in between four electrodes for electro-rotation measurements.[34] The resulting parameters are the inspiration for the electrophysiological model of the spheroid in the next chapter.

Given the significant size differences between spheroids and individual cells, the pursuit of achieving selective attraction based on size differences calls for an in-depth investigation into liquid biopsy approaches. *Circulating tumor cells* (*CTC*) show a significant size difference compared to other cells found in human blood and microfluidic devices are already in use to capture *CTCs* out of blood samples.[35] Current liquid biopsy in microfluidic involves collecting a small sample of easily accessible bodily fluids, such as blood urine, or saliva, and screening it for circulating tumor cell markers.[36] Epithelial cell adhesion molecule (EpCAM) is one of the most used labels for *CTC* tracing and isolation.[37] Fluorescence-Activated Cell Sorting (FACS) and CellSearch® are enrichment strategies based on fluorescence molecule labeling, but these devices struggled with data quality issues, a hindrance for suggesting therapeutic targets in clinical applications.[38] In light of this, replacing labeling with dielectrophoresis opens avenues for novel techniques that can potentially overcome these limitations and enhance the precision of therapeutic investigations. A label-free capture device based on microfluidic channel narrowing capture has already been developed for *CTC* capture [39] and shows promising suggestions of equivalent therapeutic targets when compared to the matching primary tumor samples.[38] DEP is utilized in *CTC* analysis as dielectrophoretic field-flow-fractionation (DEP-FFF) with an isolation efficiency of 90%.[40] Clinical studies confirm that DEP is an antibody-independent isolation method permitting the capture of *CTCs*.[41] This validation indicates a potential avenue for utilizing DEP to effectively manipulate *human tumor cell spheroids* within the scope of this study.

3.2 Related Approaches

The subsequent methodologies share a common thread of sorting spheroids and employing electric fields, yet they do not directly apply DEP to human tumor spheroids. Up front *spheroids* and *organoids* can already be sorted by size. The company Union Biometrica Inc. developed a large particle flow cytometer for *spheroids* and *organoids*, utilizing multiple lasers and air sorting.[42] Even though they sort successfully by size the bioelectrical properties cannot be chosen as sorting parameters, which makes this approach only related. This distinction highlights the relevance of investigating DEP's influence on spheroids' bioelectrical behavior.

Electrotaxis

Zhao et al. published 2014 a paper about a device called electrotaxis-on-a-chip platform that utilizes an electric field for wound healing in microfluidic.[43] While both electrotaxis and dielectrophoresis involve the interaction between electric field and organisms, electrotaxis is a biological response that occurs in living organisms, whereas dielectrophoresis is a physical phenomenon used for particle or cell manipulation. Electrotaxis is specific to organisms and their behavioral responses, while dielectrophoresis is a technique applied in a laboratory setting for various purposes. The discussion on electrotaxis and dielectrophoresis underscores the noteworthy biological characteristic change that can permit employing electrical fields on biological entities, suggesting the importance of post-DEP treatment investigation.

Digital Microfluidics

Liquids, especially droplets can be moved by an electromechanic force called ponderomotive force. [44] By liquid DEP droplets can be created. These droplets can be moved by a process called electrowetting from one electrode to the next by applying a voltage to the electrode nearby.[44] These techniques are like particle DEP but focused on small liquid samples. It might be interesting to observe these mechanisms on spheroids in nanoliter droplets, but it has better utilization in genetics as of the possibility of isolating single strands of DNA in picoliter droplets and then transporting them to electrowetting devices.[44] Furthermore, the convergence of Digital Microfluidics and DEP of *spheroids* presents an intriguing avenue for future research, highlighting the potential to harness both techniques collaboratively.

3.3 Research Integration

A broad overview of the possibilities of DEP on *spheroids*, equipment, and techniques was determined by this literature review. The function generator most researchers used had low output resistance like the Agilent model No. 33250A[14] or the Rigol DG4062 [30], a common frequency generator with a 10-volt cap and high available frequencies up to 20 MHz. Fortunately, they can be found in most electronics laboratories. Two successful DEP cell motion techniques were chosen for integration. Castellarnaus's approach, which examines cellular responses by studying the effects of different frequencies [14,] and Songs approach, which employs continuous flow systems to sort biological entities in a constant electrical AC field. [31] are incorporated in the study.

Two MEA chips were consequently developed, both are combinations of their successful designs. Furthermore, a new design is being explored in a third chip. The expected *spheroid* behavior was incorporated in the design based on a biophysical model called the single shell model.

3.4 Single Shell Model

With the underlying mechanisms introduced in chapter 2.4, it is now elucidated that the particle's response is determined through advanced modeling techniques. Particularly, the utilization of the state-of-the-art Single Shell Model, a robust biophysical model, plays a pivotal role in accurately deciphering the spheroid's behavior. The single shell model in biophysics simplifies a biological system, typically a cell or vesicle, by assuming it is a single spherical shell with electric properties. The dielectric behavior of a cell is mostly dominated by the cellular membrane composing the outer shell, due to their insulating properties. The permeability of a cell can then be described as: [34]

$$\varepsilon_{sp}^{*} = \varepsilon_{out}^{*} \frac{(\frac{Rp}{Rp-e})^{3}+2\frac{(\varepsilon_{in}^{*}-\varepsilon_{out}^{*})}{(\varepsilon_{in}^{*}+2\varepsilon_{out}^{*})}}{(\frac{Rp}{Rp-e})^{3}-\frac{(\varepsilon_{in}^{*}-\varepsilon_{out}^{*})}{(\varepsilon_{in}^{*}+2\varepsilon_{out}^{*})}}, \quad (4)$$

Where:

- R_p is the radius of the particle (*hMSC*: 10-30μm, *spheroid*: 100 - 250μm).
- e is the thickness of the equivalent membrane (*hMSC*: 5 nm, *spheroids*: 9 nm).
- ε_{out}^{*} and ε_{in}^{*} are, respectively, the inner compartment and outer shell transformed permeabilities (3).

The electrophysiological parameters for a *spheroid* and a *human mesenchymal stem cell* were previously determined through electro-rotation measurements conducted by C. I. Trainito et al. [34] and by T. Adams et al.[45]. The derived parameters used in the calculation are presented in the table below.

Table 1: Electrophysiological *Spheroid*- and *hMSC*-Parameter.

	σ_{out} [S/m]	$\varepsilon_{out,rel}$	σ_{in} [S/m]	$\varepsilon_{in,rel}$
Single cells	10^{-6}	1.1	0.5	60
Spheroids	$1.5*10^{-7}$	4.9	0.45	16.7

Single Cells (untreated *hMSCs* in 0.1 S/m dextrose puffer solutions).[45]
Spheroids (*Human U87MG glioblastoma* in 0.1 S/m isotonic solution).[34]
The dielectric constant of water (which is the primary component of the solution) is about 80.

These parameters constitute the cornerstone for the initial expectation modeling, guiding the predictions of particle behavior. Furthermore, the actual medium employed in this thesis, Dulbecco's Modified Eagle's Medium, possesses a measured conductivity of 1.8 S/m but differences seen in from these parameter resulting frequencies aren't caused by the medium's composition or conductivity, but rather are connected to how the cells are shaped.[46] Furthermore, not *human U87MG glioblastoma* but *human HT29 Colon Adenocarcinoma Cell Spheroids* are used in the experiments of this study. This makes the model only an expectation of what frequency range shall be considered and what deflection force might be present. The resulting force will be used for microfluidic considerations.

3.5 Microfluidics

As stated in chapter 2.4, microfluidics considerations are essential because they facilitate the creation of a microfluidic chip that encloses human tumor *spheroids* in fluids, allowing for the investigation of dielectrophoresis (DEP) effects on the spheroids. Furthermore, the device can later be turned into a *spheroid* sorting device like Song et al. cell sorting device. [31] Therefore parallel flow lines are necessary and turbulences in the fluid channel would distort the DEP deflection results as it cannot be observed if the cluster is attracted by DEP, or the turbulence moves the spheroid. Hence, a stable laminar flow must be established through the design of the channel dimensions. Generally, if the Reynolds number of a system is below 1500, it can be assumed that the flow is laminar.[25] The Reynolds number (Re) can be calculated using the following formula:

$$Re = (\rho * v * D) / \mu \qquad (5)$$

Where:

- ρ is the density of the fluid (kg/m^3).
- v is the velocity of the fluid (m/s).
- D is the fluidic diameter of the channel (m) = $2 \cdot r$.
- μ is the dynamic viscosity of the fluid ($kg/m \cdot s$).

These parameters must be considered when designing the microfluidic channel for the Lab on a chip. Additionally, a fluid transportation device is chosen based on the necessary velocity for the DEP sorting or inserting process for later high throughput or continuous application. Hagen-Poiseuille's law can be applied to determine the fluid velocity parameter. The flow rate can be calculated by:

$$Q = \frac{\pi \Delta P r^4}{8 \eta L} = Av \qquad (6)$$

Where:

- ΔP = Pressure difference (Pa).
- η = Dynamic viscosity of the fluid ($kg/(m \cdot s)$).
- L = Length of the channel (m).
- A is the cross-sectional area (m^2).
- v is the velocity of the fluid (m/s).
- r = Radius of the channel (m) = $\frac{D}{2}$.

In a rectangular cross-sectional area, the radius is approximated by $r = \sqrt{(A/\pi)}$

The fluid velocity influences DEP sorting efficiency because the *spheroid* needs time to travel between the parallel streamlines. For better understanding Fig.2 can be consulted. If the flow is too fast the *spheroids* won't get sorted. Next detailed in the Methods is how the reviewed principles are applied practically and how based on them, the design and simulation of the microfluidic chip and the MEA pave the way for effective DEP exploration.

4. Methods

"What I cannot create, I do not understand." - Richard Feynman. This chapter provides an in-depth explanation of the methods employed, including mathematical modeling, simulation, and fabrication. It details the progression from initial calculations to determine design parameters, followed by the microfabrication of electrodes to match the design specifications. Additionally, it covers the fabrication of the lab-on-a-chip, the adapter design facilitating the chip-to-frequency generator connection, and concludes with a thorough breakdown of the experimental procedures conducted.

4.1 Clausius Mossotti Factor Modeling

A MATLAB symbolic math (Symbolic Math Toolbox / R2023a / MathWorks) model was developed to determine the frequency range to observe *spheroids* movement and separation by implementing equation four and table one. Furthermore, the electrode distances to be observed were determined by using the DEP Force equation (Eq. 1), the Newtonian equation of motion, and the estimated Clausius-Mossotti factor magnitude, the final distance traveled by the cells and *spheroids* can then be calculated in alternating electrode distances with an estimated mass of 1 µg and a radius of 100 µm. An AC Voltage of 20 V peak-to-peak was considered, which represents the highest voltage achievable by standard frequency generators. The resulting force field is directly proportional to the square of the electric field gradient and therefore directly proportional to the square of the voltage applied. Decreasing the voltage leads to an exponentially extended transition time. Following *spheroid*/*organoid* parameters were selected: a mean radius of r = 100 µm and a mass of m = 1 mg. The self-written code can be accessed in the Appendix. The code initially defines constant parameters, followed by defining symbolic variables, performing symbolic calculations, and subsequently transforming these symbolic equations across a specified numerical range for visualization purposes. The choice to use MATLAB's symbolic math capability facilitated convenient parameter adjustments for subsequent model fitting and resulted in enhanced computational efficiency compared to numerical calculations. The resulting electrode distance parameters were incorporated into the design.

4.2 Fluid Dynamics Modeling

A pressure-driven pump is chosen in microfluidics to enable precise control of fluid flow, particularly for delicate biological samples. The pressure range of the pressure driven microfluidic flow controller OB1 MK4 (ELVEFLOW/ELVESYS) is 0 to 200 mbar and has a minimal flow rate of 0.1 nanoliters/min.[47] The Reynolds number was consistently considered during the iterative process of reducing the channel width to determine the required pressure for achieving laminar flow. This calculation was subsequently verified and visualized through a computational fluid dynamics (CFD) simulation using Autodesk CFD 2023. In the simulation a simple straight flow profile was used instead of a parabolic flow profile to focus more on the goal of visualizing the deflection of the spheroid flow traces.

4.3 CAD Design

The microelectrode and microfluidic channel designs were meticulously crafted using Autodesk Fusion 360. This strategic choice capitalizes on Fusion 360's extensive capabilities in modeling and rendering, enabling the creation of intricate designs. Additionally, the mask design process was executed with precision through the utilization of K-layout and AutoCAD (Autodesk) software, because of data compatibility. The subsequent section elucidates the process of transforming the finalized designs into masks, followed by the microfabrication of the electrodes.

4.4 Fabrication

4.4.1 Micro Structuring

The micro structuring process was carried out at the clean-room facility of TU Wien, Center for Micro and Nano Structuring. Within the work area, the air is constantly recirculated through fan units containing high-efficiency particulate absorbing filters (HEPA), and yellow lighting is installed for photolithography, to prevent unwanted exposure of photoresist to light of shorter wavelengths. The micro-structuring process is explained in the following. Initially, the electrode design is integrated into a photolithography mask using a laser mask writer. A glass substrate is cleaned and coated with adhesion supporters, followed by applying a photoresist. The sample undergoes multiple exposure and baking steps, resulting in a cross-linked resist pattern. After development, a gold structure is formed through a lift-off process. A passivation layer of Si3N4 is added, and positive photolithography in combination with reactive ion etching is employed to expose electrode contacts. The finished multi-electrode array (MEA) is then further processed. The process is described in detail further, for detailed operation description of the individual process a step-by-step description is attached in the appendix containing further specific machine parameter. A box graph containing the fabrication steps is visualized in Fig. 4.

Figure 4: Box graph visualizing the steps in the micro structuring process.

First, the electrode design was integrated into a photolithography mask with a laser mask writer. In the mask writing process, a focused light beam removed the chromium layers on a mask blank according to the desired electrode pattern. The resulting mask contains a negative image of the electrode structure.

Second, A glass substrate (SCHOTT® D263) was chosen as chip wafer. It was cleaned with acetone first and isopropanol after in an ultrasonic bath for 30 seconds each. To increase gold adhesion on the glass surface, the glass wafer was sputtered with Chromium respectively Titanium by a magnetron sputterer (VON ARDENNE). Spin coating an adhesion supporter like Titanium prime resulted in similar adhesion support without the need for a chromium back etching process. In the next step, a photoresist (AZ® 5214) was dispensed on the wafer placed in a spin coater. After spin coating the glass wafer at 3500 rpm for 35 s, the sample was placed on a 100 °C preheated plate for 60 seconds, this process is called „Soft bake“. The fabricated mask was installed below the UV lamp in a mask aligner, the sample was aligned to the mask, exposed for 5 seconds, and placed on a 120 °C plate. After this “post-exposure

bake" the exposed areas are now cross-linked, which makes them more resistant to dissolution in the developer solution. Next, the sample was flood exposed without a mask for 15 seconds. Due to this exposure step, the areas of the photoresist, that were not exposed to light during the first exposure, become completely soluble to the developer solution. The glass substrate was placed in a metal ion free (MIF) developer for 75 to 90 seconds and cleaned with deionized water. The resist layer was measured with a profilometer (Dektak®) and resulted in a 1500 nm solid resist height. One layer of titanium and two layers of gold were sputtered on the plate to reach a nominal height of 150 nm. The plate was bathed in Acetone and with a low-pressure acetone stream from a pipette, the resist was washed off along with the sputtered metal on top. This process is called "Lift-off". A gold structure remains in the areas where no photoresist remained after the photolithographic development and the gold multi-electrode array is created. A passivation layer of 300 nm Si_3N_4 was introduced on top by PECVD (Plasma Pro / Oxford Instruments) to create electric flux barriers between the electrodes, protect the surface from oxidation, and insulate the electrode lead.[49] Positive photolithography was applied, to create a photoresist protective layer on the electrode leads but expose the electrodes at desired contacts. Positive photolithography involves UV-exposing areas where the resist should remain. In the unprotected layers, the electrodes were exposed by etching back the Si_3N_4 in the Cobra ICP Etching System (Oxford Instruments). The subsequent development of a microfluidic channel on top of the finalized MEA is detailed hereafter. The exploration further encompasses two distinct approaches for microfluidic channel fabrication: Xurography and PDMS.

4.4.2 Xurography

Xurography, a microfabrication technique, intricately carves microfluidic channels on different adhesive foils using controlled cutting tools. Xurography was employed for half of the chips even though it's not as precise as lithography because the channel geometry isn't too complex, and the process is faster than PDMS casting.[50] The procedure usually begins with drilling holes in a microscope slide.

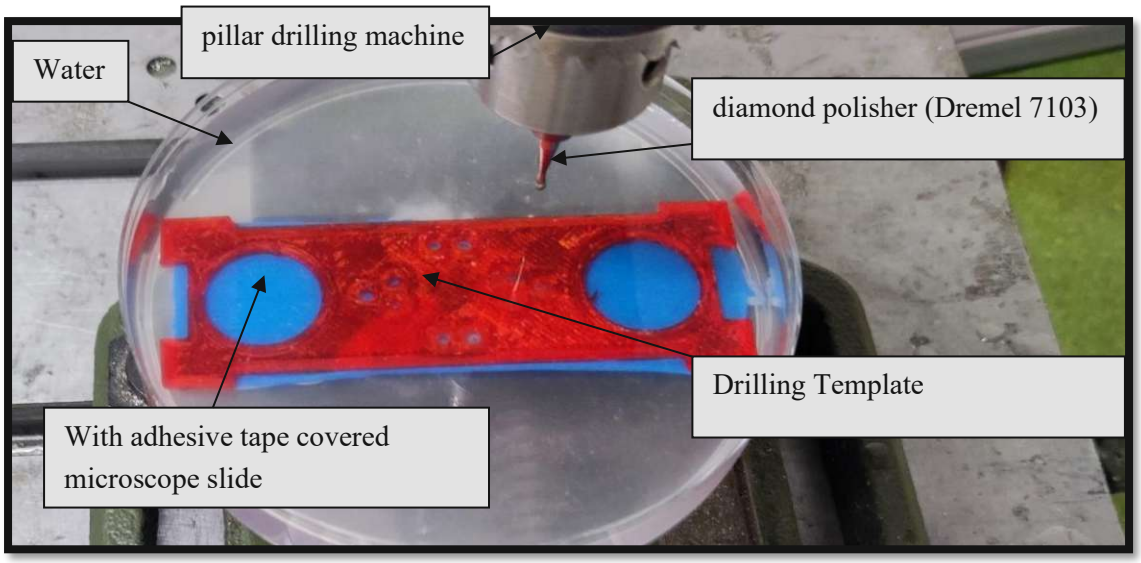

Figure 5: Protected microscope slide drilling with a drilling template for exact positioning the holes. The whole slide is proceeded with adhesive tape to improve the tensile strength of the glass to prevent glass shattering. The slide is submerged to prevent overheating.

Holes were submerged drilled in a microscope glass slide (Bresser) via diamond polisher (Dremel 7103 or DRILAX) in a culture plate. Most microscope glass slides show a high ductility, after trying various brands the Bresser and Avantor microscope slides showed the best results in terms of fragility. To ensure stability and open the possibility to drill holes close to the edges of the microscope slide, the glass is covered with adhesive tape, and a specific drilling template is used, and depicted in Fig. 5. The surrounding water is subjected to absorb the extensive heat produced during drilling glass. After drilling, the slides were bathed in Isopropanol and washed in deionized water afterward, the remaining water particles were removed with impregnated wipes and air pressure. The material used for microchannel fabrication was considered for designing the channel dimensions. One layer height of hydrophobic ARCare foil (90106NB /Adhesive Research) is 140 µm.[51] This might be suitable for cell experiments but for *spheroids* or *organoids* in diameters exceeding 140 µm multiple layers are needed. Single pass cutting of the desired channels with a blade depth of 10, a force of 33, speed of 3 with a cutting plotter (America Silhouette) in the double adhesive foil (ARcare® 90106NB) resulted in microfluidic channels. The foil was placed on top of the slide with the drilled holes as alignment markers.

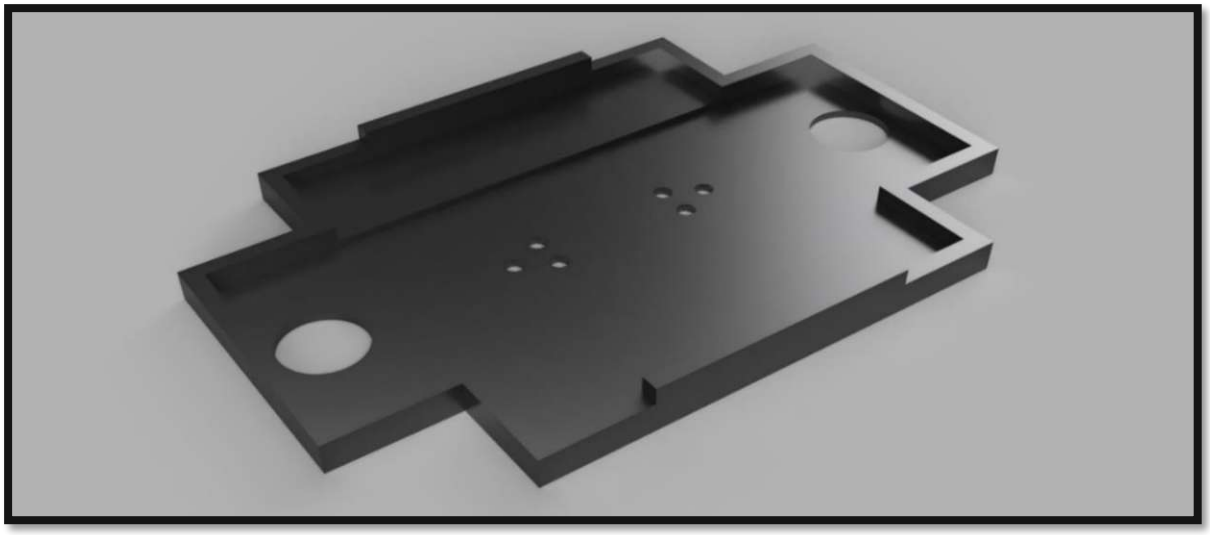

Figure 6: Rendered CAD model of the Assemble Case /Drilling Template for attaching microscope slide with MEA containing glass substrate via double adhesive foil.

A positioning case was designed (Autodesk Fusion 360), 3D printed (Ender 5 / Creality) in Polyethylene Terephthalate Glycol (PETG), visualized in Fig. 6. The microscope slide with the double adhesive foil on top is then bonded with the MEA chip inside the positioning case, resulting in the creation of a lab-on-a-chip device shown in the results chapter in Fig. 37. For the connection with a microfluidic pump, ports were attached by epoxy gluing on tubing (Ismatec IDEX Health & Science, Tygon LMT-55, standard Part No. SC0029T). As already mentioned all microfluidic chips were fabricated in two styles. Xurography and PDMS. Now that Xurography has been described, let's step into the PDMS fabrication style.

4.4.3 PDMS Casting

Microfluidic PDMS casting is a technique used to create tiny channels that handle small fluid volumes. The process is described in the following. Molds containing the channel structure were (Autodesk Fusion 360), 3D printed (Ender 5 / Creality) in PETG- The CAD models of the channels are visualized in Fig. 28 and Fig. 34. A mixture of 20 g PDMS and 2 g of curing agent was prepared and degassed to remove any trapped bubbles. The PDMS mixture was then poured into the 3D printed PETG mold and heated at 110 °C for one hour on a heat plate. Using a razor blade, the PDMS structure was gently separated from the mold, and reservoir wells with a diameter of 1mm were introduced using a common biopsy puncher. The hardened PDMS structure and the MEA Chip were subjected to oxygen plasma activation at 300 W for 3 minutes. The MEA glass slide was aligned and firmly pressed on the plasma-enchanted side of the PDMS block. Afterward, the glass slide, with the attached PDMS, was placed on a heat plate for one hour to promote adhesion. The resulting device can be observed in Fig. 39 in the Results chapter.

4.4.4 Fabrication of Chip Periphery

To create an electric field inside the chip, a frequency generator, the Wavetek Phase-lock Generator, Model 186 (5MHz), and the RIGOL function generator Modell DG822 (20MHz) were utilized. To connect the MEA with the frequency generator a 60-pin adapter was designed, additive printed in Polylactic Acid (PLA) via 3D-Printer (Ender 5 / Creatlity), assembled, and tested. The plug is visible in Fig. 40 in the results chapter 6.2.1 The pogo pins possess a 1 mm diameter, and a total length of 9.5 mm. Twisted pair cable was crimped and soldered to female and male DuPont adapters. The female end was then soldered to the pogo pins. Design specifications according to DIN 7154 resulted in an ISO–press fit between the case and the pogo pins. On the edges of the adapter, 4 inserts are located for M4 screw nuts to apply pressure to the adapter and press the pogo pin heads on the sample electrodes. To test the functionality, the junction adapter was connected to the RIGOL function generator DG822. The resulting sinusoidal wave and voltage in peak-to-peak amplitude were investigated using a common Oscilloscope. The breadboard, the cable length, and the various adapters result in good frequency transfer but carry resistance.

Another designed adapter was designed for the xurography version of the chips. An design with 36 pins was considered. The same standards explained before were used for fabrication, except the pins only had a height of 2 mm and instead of DuPont adapters and twisted pair cable, a VB-cable (HiFi - cable) was directly soldered on the pins and to the coaxial cable. The Junction adapter carries smaller resistance, but the device needs to be pressed on the chip to ensure proper contact between the adapter and the electrodes. This results in good microscope imaging because of matching focal height but makes it complicated to use and the voltage connection to the electrode pads of the MEA looser.

A third adapter was designed as a result: The Spider Adapter which is in Fig. 45 of the results in chapter 6.2.2 observable. The third connection device carries single short cables for individual electrode activation, 9.5 mm long pogo pins, M4 screws, and bolts to apply pressure via the pins on the electrodes. The device was designed, 3D printed, and the pins were soldered via DuPont adapters to cable and press-fit inserted. Next, its explained how the fabricated devices were set up and the experiments conducted.

5. Implementation

„Ideas alone have little value. An innovation's importance lies in its practical implementation.” - Werner von Siemens. The set up of the experiments and the execution of predefined steps with determined paremeters and actions inside the laboratory are described in this chapter.

5.1 Experimental Set Up for DEP Analysis

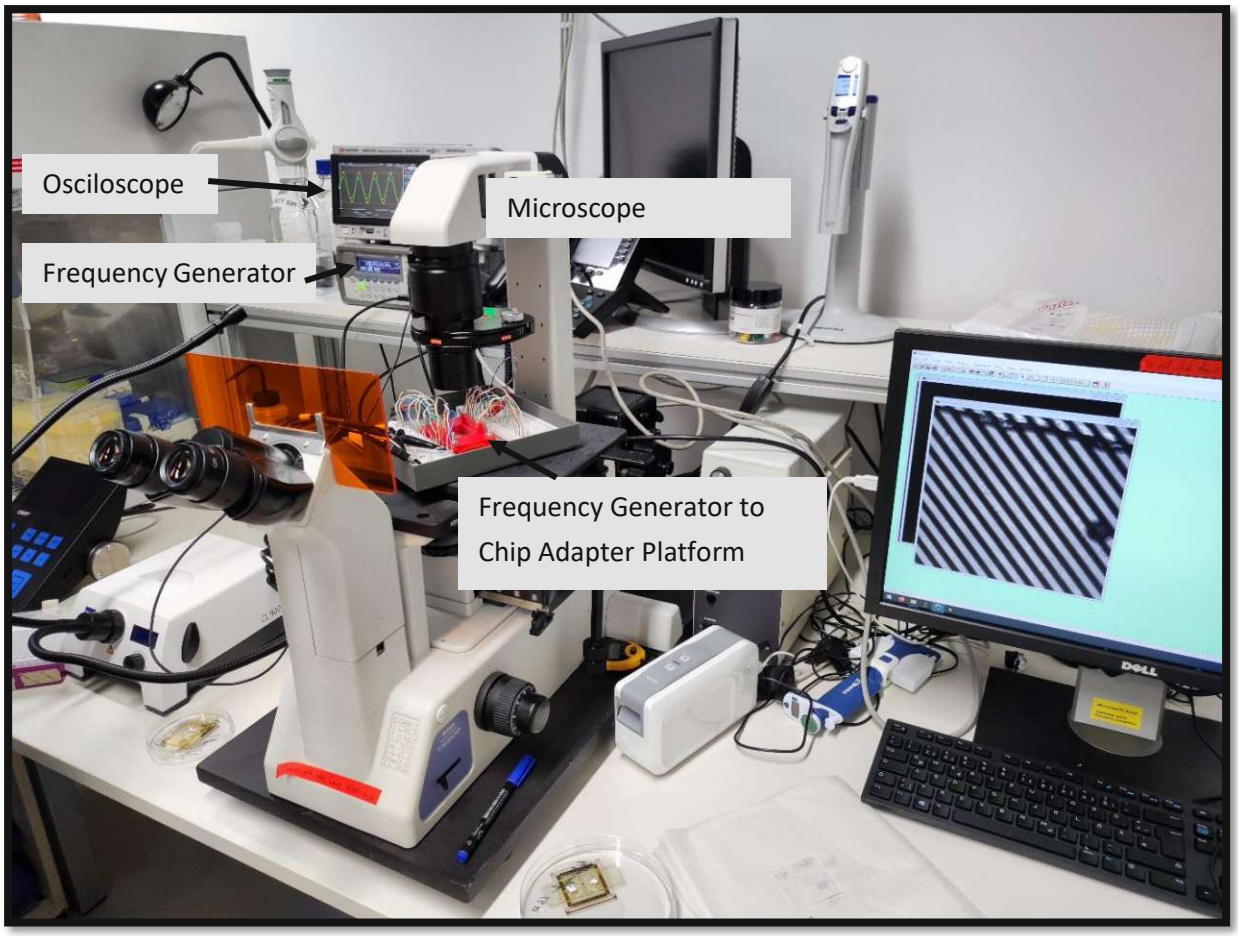

Figure 7: Photograph of the experimental set-up for DEP analysis of biological samples, Components for Experimental Analysis: Nikon Eclipse TE200 microscope and software Hokawo (Hamatsu). Electric connectivity is established through an Agilent 33220A frequency generator, connected via a dual-port BNC adapter. This adapter links the system to a Keysight DSOX1102G oscilloscope through a direct BNC connection, while also interfacing with the pin adapter through BNC to crocodile clamps.

The experimental setup, as depicted in Fig, 7, consists of several key components. A Nikon Eclipse TE200 microscope to capture both videos and images through the software Hokawo (Hamatsu). To establish the electric connections, a frequency generator, specifically the Agilent 33220A model with a maximum frequency of 20 MHz and 10 V, was linked to the setup via a two-way port BNC adapter. The adapter was connected at one side to the oscilloscope, a Keysight DSOX1102G, through a direct BNC connection and at the other side to the LOC periphery via BNC to crocodile clamps. The LOC periphery is explained in chapter 6.3. The Xurography version of the chips was subject to microfluidic analysis.

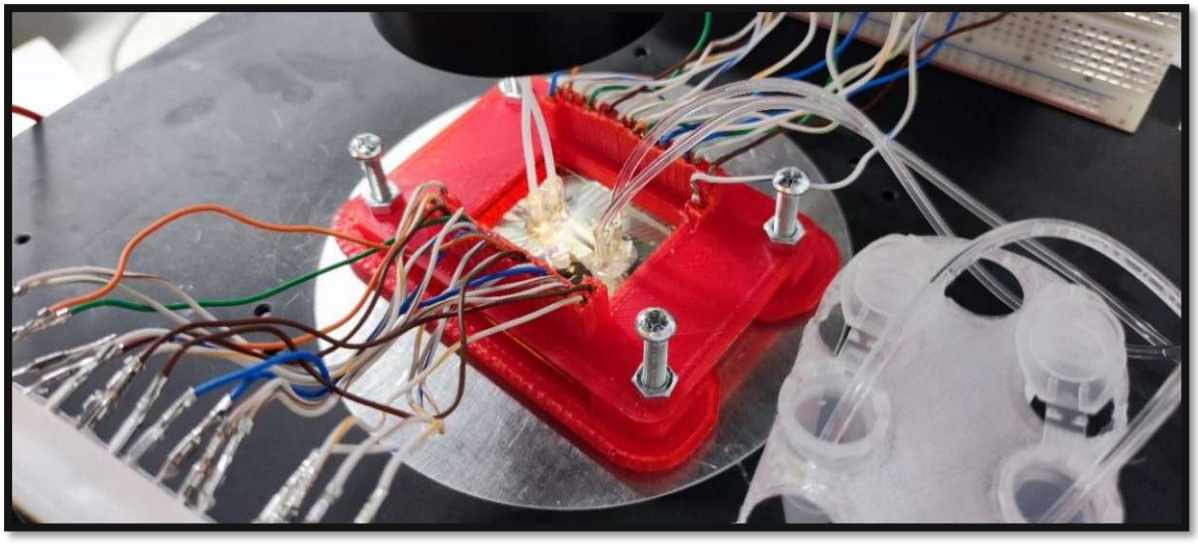

Figure 8: Close view photograph of the Spider Adapter in the microfluidic set-up with inserted DEP Diversion Chip 1. Falcon tubes were connected to the Outlets

The microfluidic setup is shown in Fig. 8. Additionally, to the set up explained before, the microfluidic set up contained the Elveflow OB1 pressure-driven pump, which is described in detail in the Methods section 4.2, connected by tubes. The pump was used to generate the required fluidic flow with a pressure of 9 Pa. Two Elveflow-connected falcon tubes were connected to the lab-on-a-chip system and outlet tubes were connected to Eppendorf flasks through epoxy glued ports.

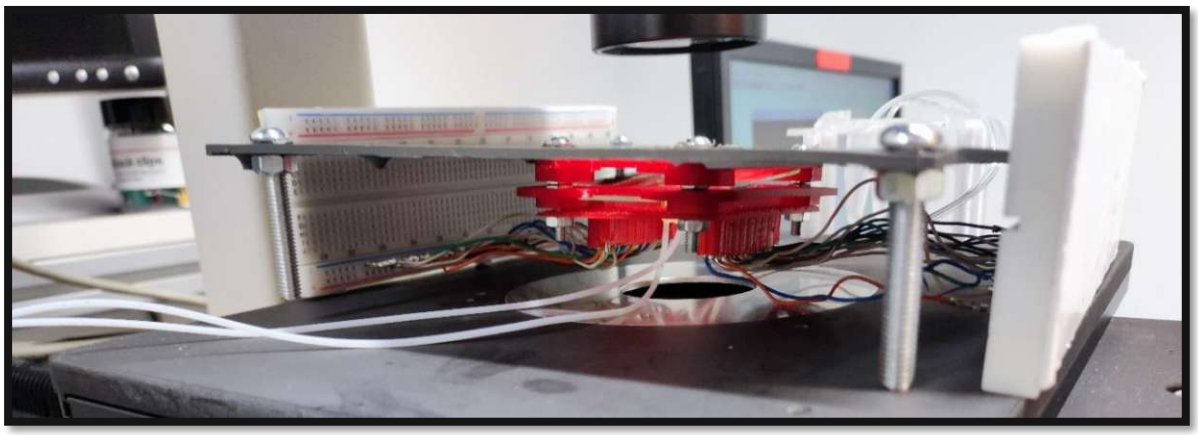

Figure 9: Photograph of the Spider Adapter in the microfluidic set-up with inserted DEP Diversion Chip 1 in an overhead set-up.

Alternatively, the chip periphery including the chip device can be mounted overhead using four M6 screws, allowing the platform to be flipped over so that the electrodes are positioned on top of the channel, as shown in Fig. 9. This configuration is useful for high-throughput system setups as it helps prevent cells from getting stuck between the electrodes, but imaging via common microscopes might be challenging. The microfluidic set up is quite challenging, mainly because of the port and friction considerations, therefore most of the experiments in this study were conducted in static. The static set up is more convenient as it just requires pipetting the organic subject into the PDMS reservoirs.

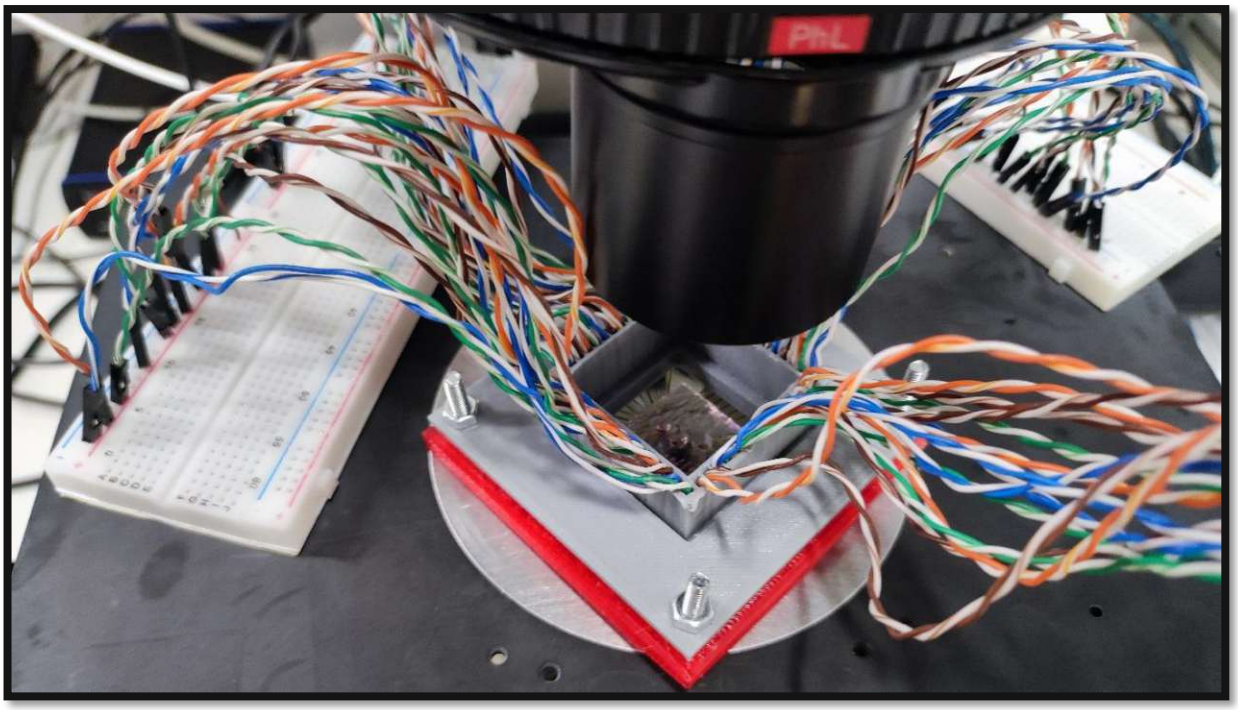

Figure 10: Close view photograph of the Plant Adapter in the microfluidic set-up with inserted DEP Diversion Chip 1.

The static set up depicted in Fig. 10 consists of the same set up explained earlier this chapter except for the use of the plant adapter

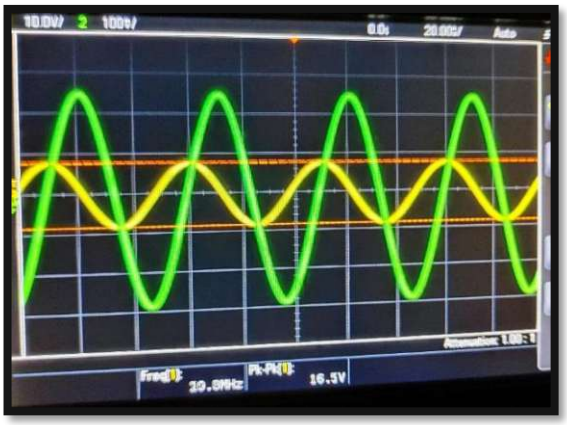

Figure 11:Photograph of the oscilloscope sinusoidal voltage during the experiment. Measured to chip applied voltage (Green), measured behind 2 Ohm (Yellow).

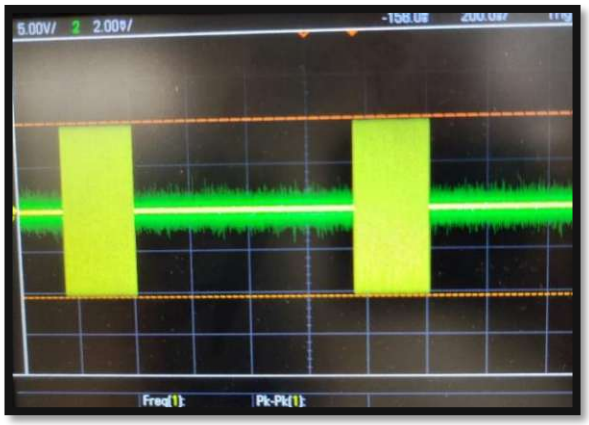

Figure 12: Oscilloscope Sinosiodial 1s Pulses to replicate Song et al. AC field with alternate on/off control. [31]

To measure the current flow through the spheroid containing Dulbecco's Modified Eagle Medium (DMEM), a parallel circuit consisting of two two-ohm resistors was employed. As the current flows through these resistors, a voltage drop occurs across each resistor. By measuring the remaining voltage after the voltage drop, the current value can be determined using Ohm's law. In the specific experimental conditions, the measured current at a frequency of 200 kHz was 75 mA. In Fig. 11 are the sinusoidal wave at 20 MHz and the voltage drop by two 2 Ohm resistors is shown. At a frequency of 20 MHz, the measured current was 200 mA, which corresponds to the maximum output current. It's important to note that 200 mA represents the upper limit of the output current in this setup. Fig. 12 shows the 1s pulse configuration output to test the impulse reaction of the subject of investigation based on Song et al. AC field with alternate on/off control. [31] The investigation subject: *spheroids* and cells are explained next.

5.2 Sample Preparation and Experimental Procedure

The ensuing section delves into the experimental preparation, with detailed protocols for preparation and analysis.

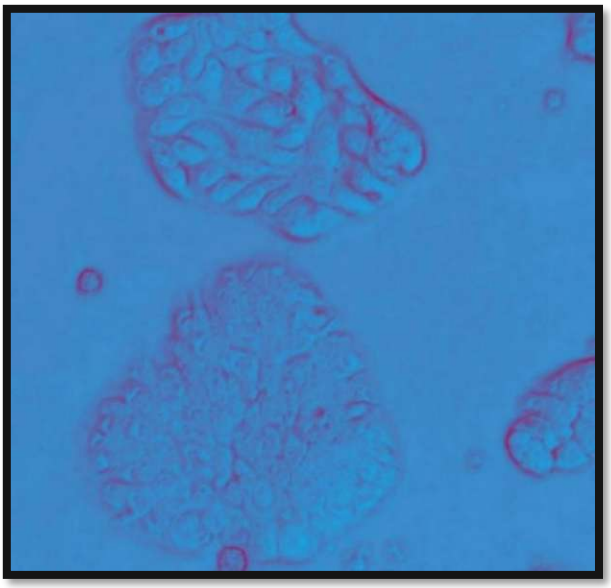

Figure 13: Microscope image of human colon adenocarcinoma cells (HT29)

This study used aggregated human colon adenocarcinoma cells (HT29) provided by Prof. Dr. Sonia Prado Lopez. Fig. 13 is a microscope image of HT29. They were among others the main subject of analysis either in single cell form or in spheroidal structure. All experiments were conducted at room temperature (20 – 22 °C). During static tests, chips without ports were used. The biological samples were prepared by thawing the frozen cells in a water bath, centrifuging at 1,3 rpm for 5 min and resuspending in DME if dimethyl sulfoxide (DMSO) was used for cryopreservation. The cells were diluted to a concentration of 450 cells/µl to avoid clogging the channel or tubes, stained with Hoechst (working conc. = 2µg/ml) and treated with trypsin. The *spheroids* were previously aggregated in culture well plates. Centrifugating them wasn't necessary because Bambanker (Nippongenetics) was used for cryopreservation. The experimental procedure involved pipetting 5µl of DMEM directly into the inlet of the chip or reservoir, followed by 5µl of *human mesenchymal stem cells, human colon adenocarcinoma cells, caco- 2 cell clusters* or *spheroids* provided by Prof. Dr. Sonia Prado Lopez. To rearrange the cells, suction was applied via pipette. The behavior and movement of the cells were then observed at three different frequencies: 20 kHz, 200 kHz, and 2 MHz. The purpose of these observations was to determine if the observed cell and *spheroid* movement aligned with the switch of motion direction predicted by the DEP calculations presented in Chapter 4. For example, at a frequency of 200 kHz, the cells were expected to move towards a lesser electrical field location, parting from the electrodes due to a negative Clausius-Mossotti factor. Conversely, at a frequency of 20 MHz, the cells were expected to move towards the electrodes. By examining the cell and spheroid movement under these different frequency conditions, the experimental results could be compared to the theoretical predictions. Additionally, the voltage applied to the LOC stayed constant at a peak-to-peak voltage of 10V. To investigate the phenomenon of electrolysis, a DC voltage was introduced using the same experimental setup and procedure. In the fluidic test, 10 ml of DMEM and 10 ml of diluted cells at a concentration of 450 cells/µl were filled into Falcon Tubes. These Falcon Tubes were inserted into the Elveflow pumping system. Gradually increasing pressure, ranging from 0.2 mbar to 200 mbar, to transport the cells from the Falcon Tubes into the microfluidic chip and out to be collected in Eppendorf flasks.

6. Results

"The most exciting phrase to hear in science, the one that heralds new discoveries, is not 'Eureka!' but 'That's funny...'" - Isaac Asimov. The Results chapter provides a comprehensive overview of the study's findings, encompassing various stages of investigation. It begins by showcasing the outcomes of simulation and mathematical modeling, where the estimation of the Clausius-Mossotti factor is employed to identify optimal frequencies and the deflection of *spheroids* is determined in inhomogeneous electric fields to estimate a range of electrode gap distances. The chapter then transitions to the presentation of designed chips, integrating electrode grid distances derived from simulations. These chips, three in total, include two designed for minimal deflection and one for spheroid insertion within a pocket. Subsequently, the focus shifts to the physical realization of LOC devices, fabricated using both PDMS and xurography techniques. The chapter also features the introduction of realized adapters, such as the spider adapter for the xurography-fabricated chip and the plant adapter for the PDMS chip, connecting the LOC to the frequency generator. The experimental results section follows, offering insights into the achievement of the thesis objectives, such as successful spheroid movement, as well as addressing side effects such as electrolysis. These outcomes contribute to the fitting of the spheroid Clausius-Mossotti factor model, concluding this extensive exploration of the study's experimental outcomes.

6.1 Simulations

6.1.1 Clausius Mossotti Factor Simulation

As stated in Chapter 2 the frequency-dependent Clausius-Mossotti factor K(ω) (Eq. 2) determines if the cell is attracted or expelled by the electrodes (Eq. 3) and is thereby the major selection tool. The following graphs display the factor evolution for *hMSCs* and *spheroids* respectively *organoids* over the frequency range. The fundamental model for the interpolation is described in Chapter 4.1. The underlying code used for calculation and plotting can be accessed in the Appendix.

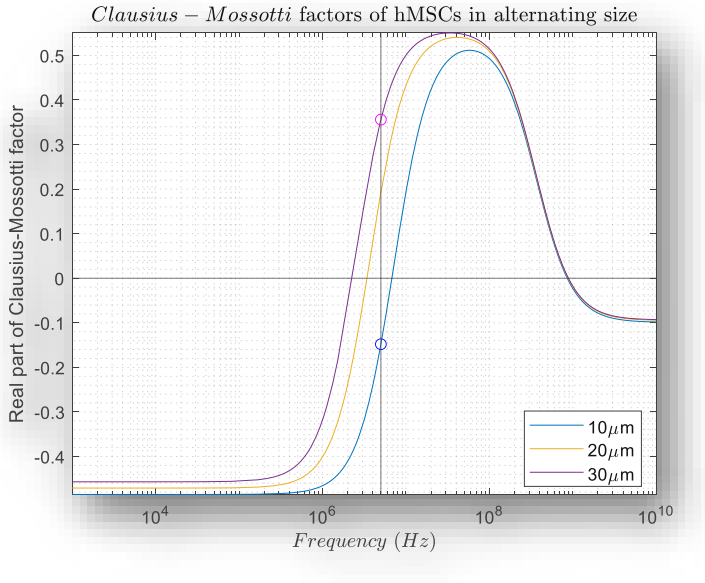

Figure 14: MATLAB simulation of C-M factors of hMSCs in alternating diameter over a frequency range.

The simulation results depicted in Fig. 14 reveal that at a frequency of 5 MHz (horizontal line), stem cells exceeding diameter sizes of 20 µm are expected to encounter a force that moves them toward electrode, where the maximum electric field occurs (p-DEP). In contrast, cells below 10 µm are expected to experience a momentum towards regions lesser electric field (n-DEP), while cells within the size range of 10-20 µm in between exhibit minimal movement.

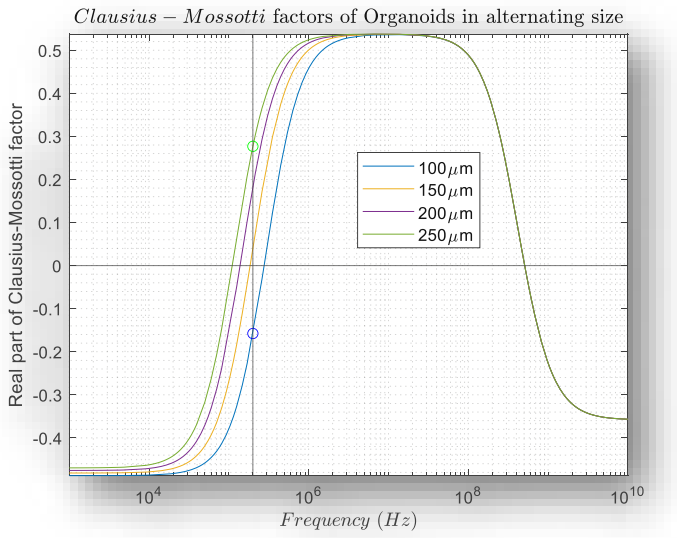

Figure 15: MATLAB simulation of C-M factors of organoids/spheroids in alternating diameter over a frequency range.

As depicted in Fig. 15, the same behavior for *organoids/spheroids* in sizes 100 µm and 250 µm can be expected at 200 kHz and utilized to e. g. move only the *organoids/spheroids* and cells above 150 µm toward the electrode.

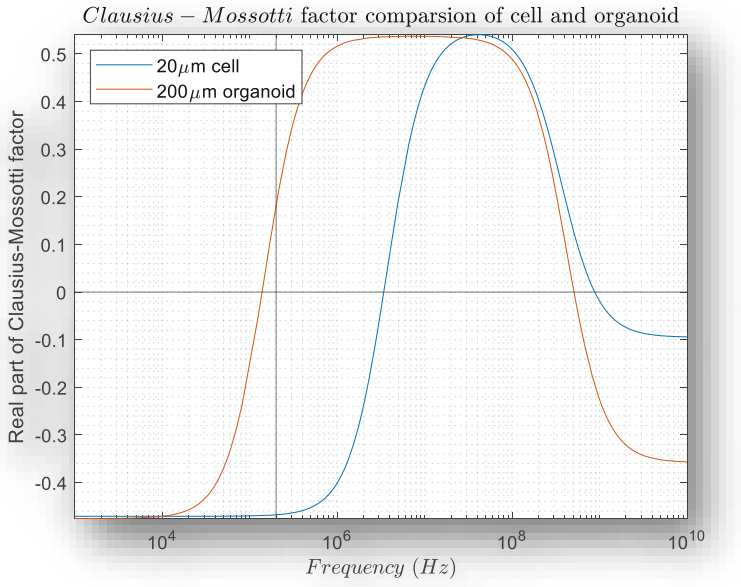

Figure 16: MATLAB Simulation of C-M factor correspondences of 20µm cell and 200µm organoid/spheroid over a frequency range.

Comparing the two models presented before in Fig. 16 leads to the assumption that at 200 kHz (vertical line) *stem cells* are expected to be repelled while *organoids/spheroids* measuring a size of 200 µm in diameter are expected to be attracted by the electrodes. On the other hand, at 2 MHz exclusively, spheroids are expected to be attracted, as the Mossotti factor for cells at this frequency is approximately zero. Therefore, it can be said that the investigation is best suited within the frequency range of 200 kHz to 20 MHz, the range within which the experiments with *spheroids* were conducted. Now that the frequency range is interpolated the distance of the electrodes needs to be determined.

6.1.2 DEP Spheroid Deflection Simulation

Understanding the electrode distance holds significance as it provides insight into the potential movement that can be anticipated from the 3D cell culture aggregate in the electric AC field and the expected speed of such movement. Notably, Fig. 2 and 3 in chapter 3.2 employed an electrode distance of 50µm. However, this specific distance cannot be applied in the current study due to the larger size of the organoid/spheroid under investigation. Therefore, the movement of the Organoid/Spheroid is modeled in the following.

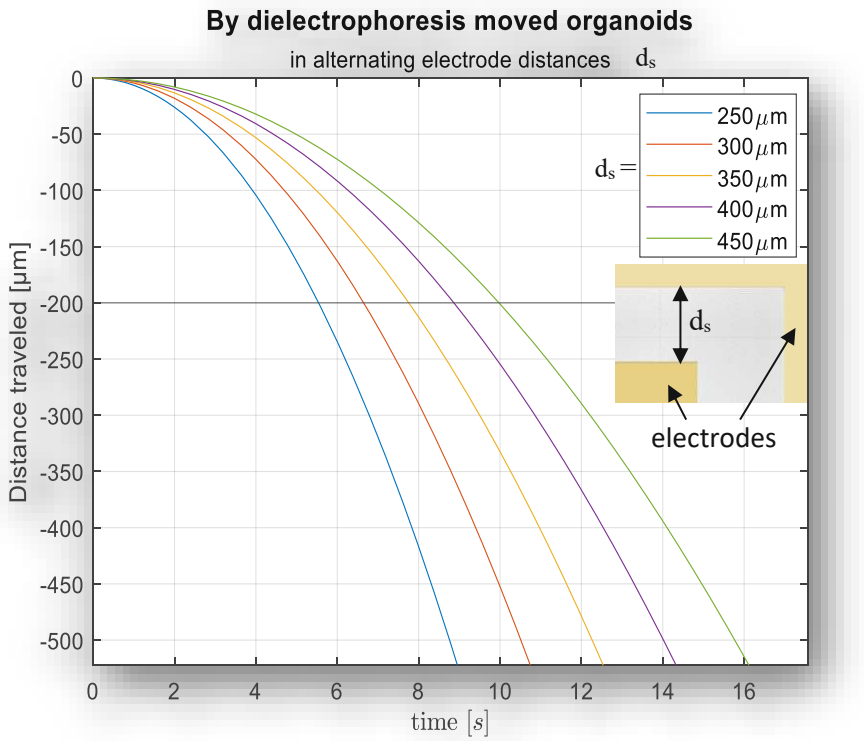

Figure 17: MATLAB simulation of the DEP organoid/spheroid deflection in 250 µm – 450 µm electrode gaps over time.

The parameter for the calculation can be accessed in chapter 4.1. The resulting final deflection with an average velocity of 20 µm/s is shown in Fig. 17. This is a relatively slow deflection velocity when compared to the 1 second DEP pulse velocity used by Song et al. on single cells. [31] Even though this study concentrates on biological matter exceeding the size of single cells. Upon closer inspection of Fig. 5, it can be approximated that a period of 4 to 6 seconds could potentially initiate movement within the spheroid. Notably, this simulation focuses on 3D cell culture aggregates measuring 200 µm in diameter; thus, smaller sizes might yield even more pronounced deflection. Continuing with our endeavors, the time window of 4 to 6 seconds, along with an electrode distance not exceeding 350 µm, remains a central focus for ongoing design.

To adapt to the larger size of the *organoid* compared to cells, the distance between the electrodes was increased to at least 200 µm in the previous simulation. However, this led to a lower electric field, resulting in prolonged movement. As already stated, in an electrode gap width of 400 µm, it takes approximately 15 seconds to move the cell clusters by 200 µm, which is a long time for an electric pulse reaction. The biophysical quasi-membrane DEP response of a cell cluster with electrodes, which do not cover the entire quasi membrane of the *spheroid* or *organoid*, has not been investigated yet but is simulated now in the following.

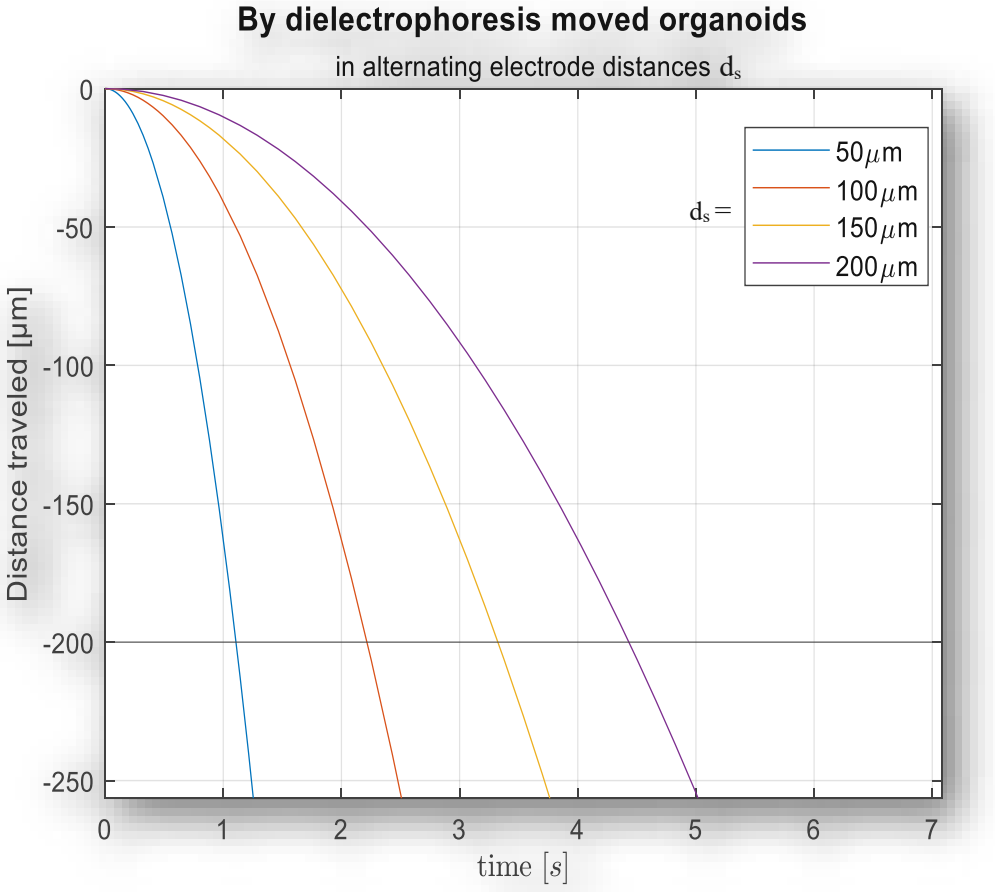

Figure 18: MATLAB simulation of the DEP organoid/spheroid deflection in 50µm – 200µm electrode-gaps over time.

The results in Fig. 18. shown lead to the assumption that there could be an even stronger effect with an average velocity of 200 µm/s on the *organoids*, than by positioning them in between the electrodes. The extrapolated time for a translation of 200 µm is expected to be five seconds. Here it must be said that the resulting motion cannot be safely interpolated with the single shell model described in chapter 3.4 as the electrode gap doesn't cover the entire outer shell and therefore the effect can even be nullified.

The the simulation investigated electrode gap distances ranging from 50µm to 400µm were integrated into the microelectrode design for experimental confirmation. Furthermore, the resultant deflection velocities of 20µm/s and 200µm/s were included in the following CFD simulation.

6.1.3 Microfluidic Channel CFD Simulation

The microfluidic channels' dimensions must be estimated before designing. The equations in chapter 3.5 were used to determine the width and height of the main channels. The height was partly limited to the highest accessible double adhesive foil height used during xurography. The Xurography process, the materials and devices used are in more detail in subchapter 4.4.2. When assembling the chip with PDMS the channel's nominal height is set to 420 µm to enable higher diameter spheroid observation. This height can be achieved using three overlays of the double adhesive foil. Therefore, 420µm is chosen for the calculation of the Reynolds number estimation. As simplification water was used instead of the cell culture media used. Water at room temperature has a density of 1000 kg/m^3 and a viscosity of 0,001 $kg/m \cdot s$. The width dimension estimated trough iteration of 2mm resulted in a cross-sectional area of $A = 0.84\ mm^2$ and effective channel radius of $r = \sqrt{(A/\pi)} = 517\ \mu m$. The deflection modeling in the previous chapter showed that four to twenty seconds are needed to deflect the cell cluster 200µm. In the 10 mm long and 2 mm wide main channel the time needed for a full deflection from the upper side to the lower would take 40 to 200 seconds. This means the spheroid should at least stay 200 seconds in the 10 mm long channel which results in a flow velocity of 50 $\mu m/s$. Therefore with Eq. (6) the maximal flow rate is 25.85 $\mu l/s$ and the resulting pressure is 9.2 Pa (9.2 μbar). Laminar flow is unavoidable at this flow velocity with a Reynolds number close to zero. The chosen pressure-driven microfluidic pump OB1 MK4 [47] with the minimal flow rate of 0.1 is therefore applicable. The estimated pressure difference was implemented in a CFD analysis visualized below.

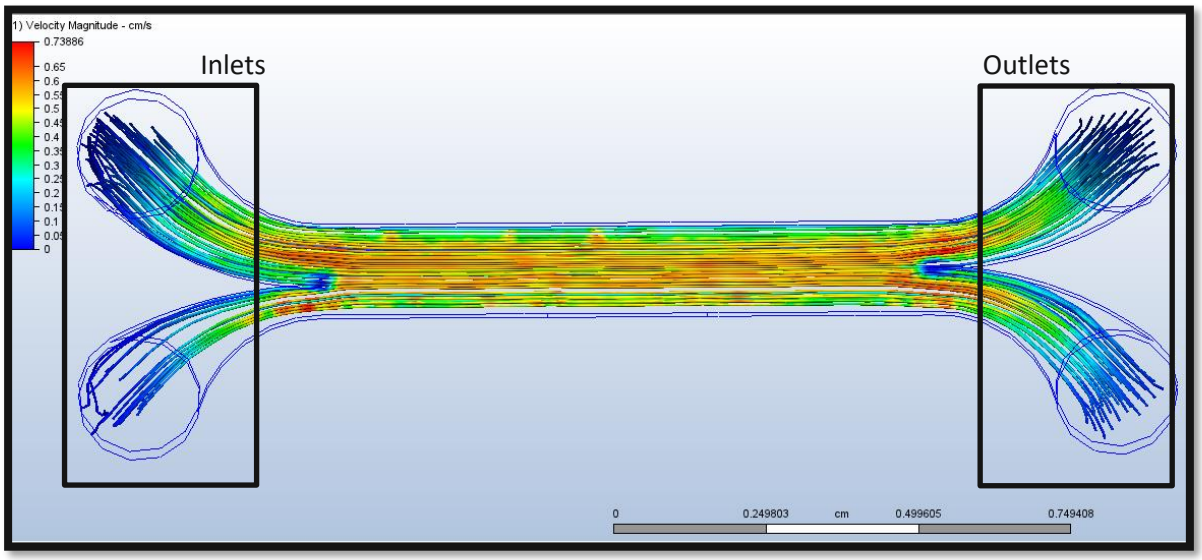

Figure 19: CFD simulation results of the Diversion Chip Channel. Visible are the parallel streamline traces representing the spheroids traveling. The left inlets both have a pressure applied of 9.2 Pascal, the outlets have 0 Pa

The purpose of the simulation is to estimate *spheroids'* streamline behaviors rather than determining numeric results. Furthermore, It must be noted that on the outlets a perfect vacuum of zero Pa is set which further distorts the results. Nevertheless, the results of the first CFD simulation, shown in Fig. 19 demonstrate that none of the streamlines in the lower channel are migrating to the upper channel due to the low Reynolds number. Next the DEP deflection velocities estimated in chapter 6.1.2 are introduced in the simulation.

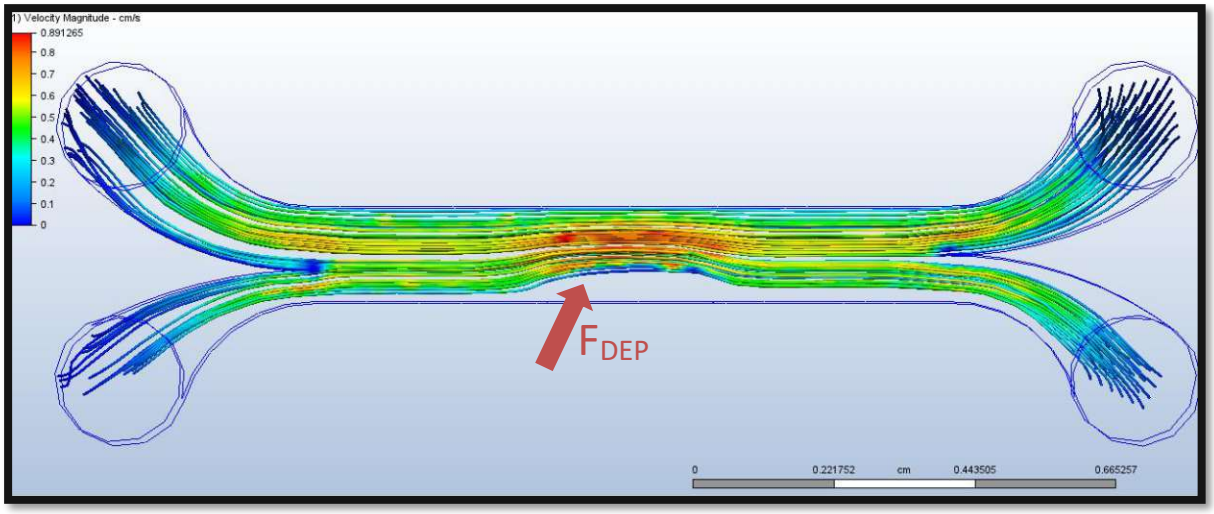

Figure 20: CFD simulation results of the Diversion Chip Channel. Visible is a shift of the streamlines traces caused by positive DEP force translation (deflection velocity of 20 µm/s) along positions of the electrode rails and the absence of microfluidic mixing.

The expected migration of *spheroids* from one channel to another due to DEP is now being investigated. To approve this in the simulation, the average deflection velocities calculated in 6.1.2 of Diversion Chip one and two were incorporated. At first the deflection velocity of 20 µm/s is introduced over a length of 2 mm. This resulted in a slight deflection for the larger electrode grid, as depicted in Fig. 21. This might not be enough shift to realize a good separation percentage.

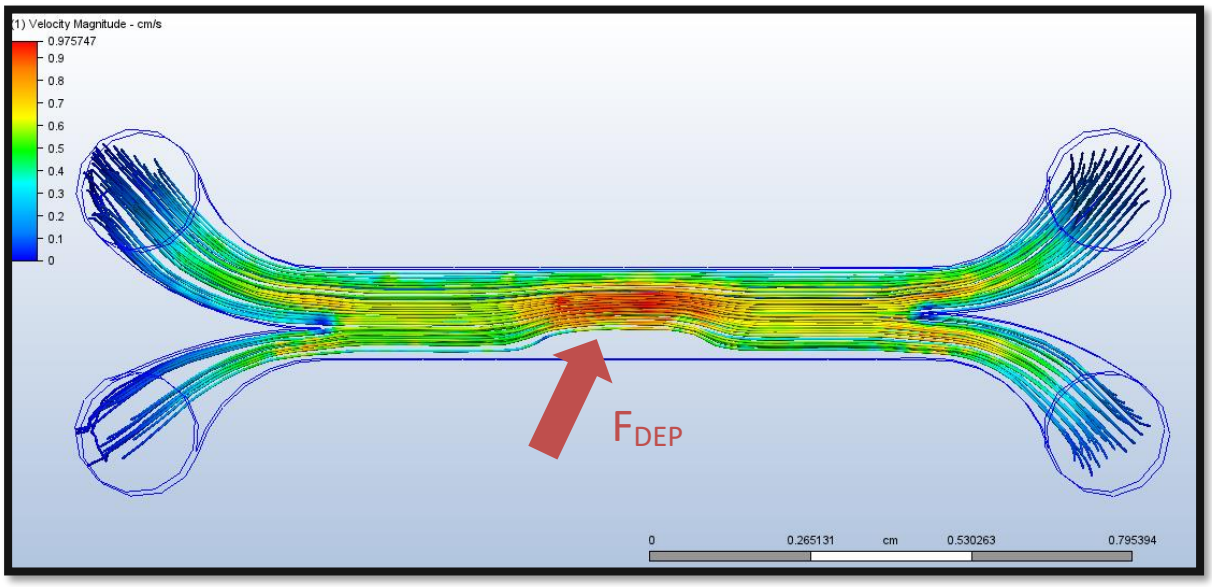

Figure 21: CFD simulation results of the Diversion Chip Channel. Visible is a greater shift of the spheroid streamlines traces caused by stronger positive DEP force translation (deflection velocity of 200 µm/s) along positions of the electrode rails and the absence of microfluidic mixing.

However, a satisfactory p-DEP deflection was simulated for the smaller electrode grid of DEP diversion chip one, as shown in Fig. 21. It is shown that the deflection is almost sufficient to shift the spheroids from the lower stream to the upper stream with velocities up to 40 % higher than in the first simulation shown in Fig.19. This might prove the feasibility of the DEP Diversion channel. Next the DEP Insertion Channel is simulated again with the pressures determined before and the DEP deflection velocity of

20µm/s to investigate if the spheroid can be inserted. Therefore, the whole upper side of the inner and outer channels are conditioned with 2 Pa, which is a rough estimation to simulate the DEP force.

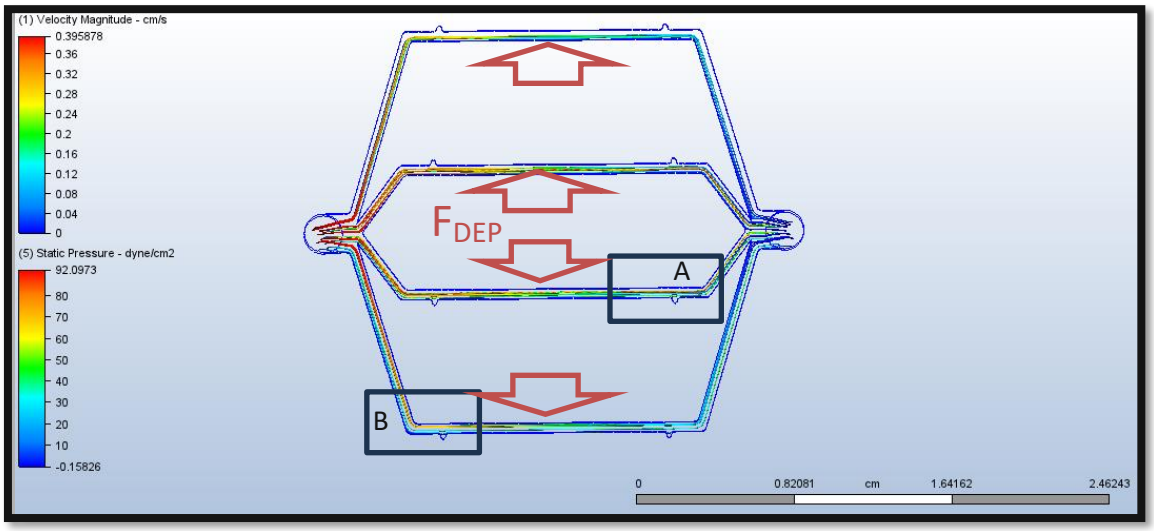

Figure 22: CFD simulation results of the DEP Insertion microfluidic channel. An equal separation is of spheroids into all four channels is visible.

Previous studies showed that 300 µm hemispherical pockets have no direct attachment to the microfluidic flow.[48] Therefore a spheroid or organoid can be placed in the pocket securely for cultivation without getting ejected out of the pocket. Fig. 22 shows the full fluid trace line breakdown. The pocket design in this study and their electrodes are further illustrated in Fig. 33. The CAD model of the Insertion Chip channel can be observed in Fig. 34.

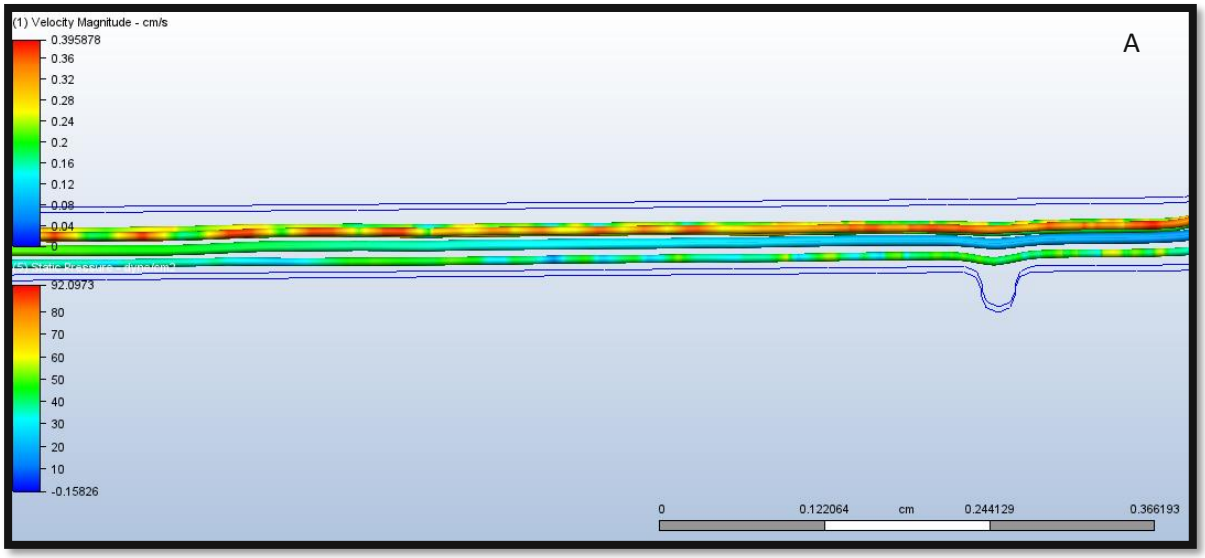

Figure 23: Section view A of the CFD simulation results of the DEP Insertion microfluidic inner channel.

The inner streamlines representing the spheroids are shown in Fig. 23. It is observable that the streamlines don't reach into the pocket. The inner channels carry higher velocities than the outer channels and therefore higher shear stress at the walls. The spheroid might not be successfully inserted in the pocket by DEP. The outer channel spheroid streamline traces are shown below.

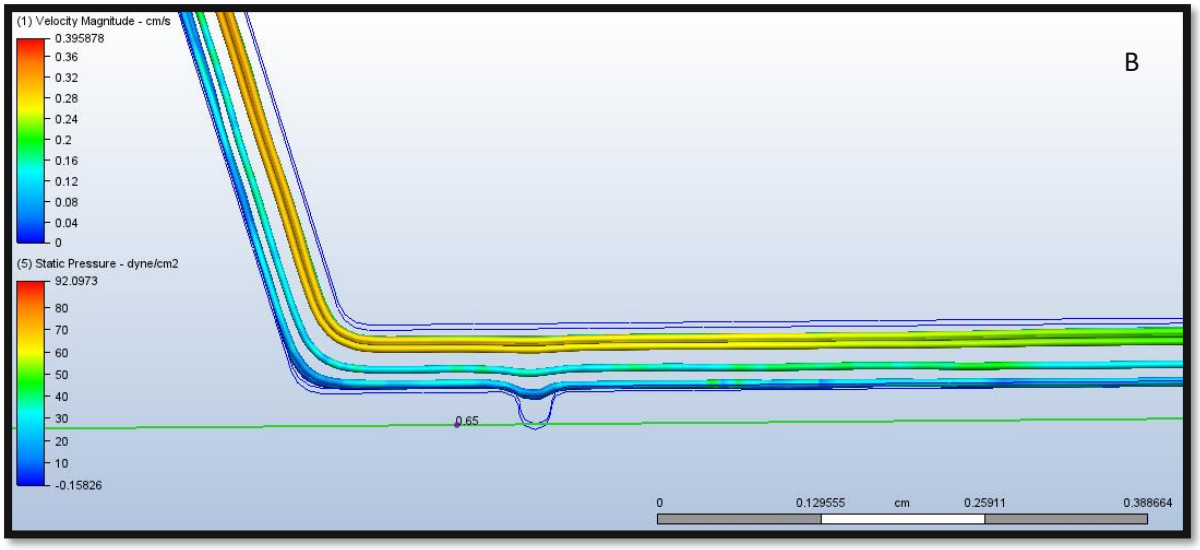

Figure 24: Section view B of the CFD simulation results of the DEP Insertion microfluidic outer channel.

In Fig. 24 the spheroid streamline traces reach slightly into the hemispherical pocket. This hints that the cell cluster can be detached from the streamlines when slightly pushed in via DEP. Having an active AC field on while inserting the cell cluster will result in sliding at the lower side of the channel caused by p-DEP and result in lower spheroid velocity caused by hydrodynamical shear stress at the walls. The deflection velocity is the same as in Diversion Chip 2 which was 20 µm/s. In conclusion, inserting the cluster into the outer channels may present a comparatively more feasible option when compared to the inner channels. The design of the inner channels must be altered to the same length as the outer to have the same result. Notably, this is a rough estimation, the actual area of deflection is only 4 mm to 6mm long and *spheroids* might encounter boundary surface friction.

6.2 Designs

Based on the electrode distance Simulations three lab-on-a-chip devices were designed. Each chip electrode and microfluidic channel design is presented separately and explained in this Chapter. At the end of section 6.2 a table overview of the chips is presented.

6.2.1 DEP Diversion Chip 1

As stated in Chapter 3.1, a continuous-flow microfluidic device for sorting stem cells had already been developed by Songs et al. [31]. The "DEP Diversion Chip 1" device goal is to investigate the accumulation of multiple dielectrophoresis force impacts of an alternating on/off electric field to laterally deflect *spheroids*, by incorporating an integrated electrode array with two electrodes, each having 50 fingers and measuring 50 µm in width, with a distance gap of 50 µm.[31]

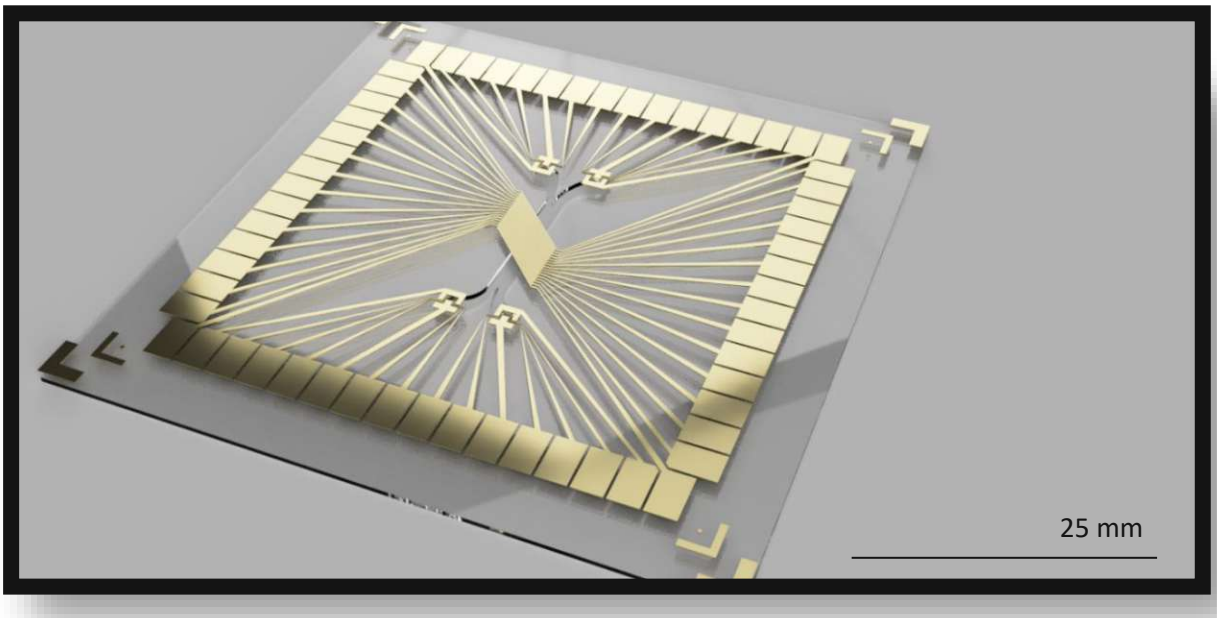

Figure 25: Rendered CAD Model of the DEP Diversion Chip 1. The outline of the chip is 49mm x 49mm, the design is based on the result that a 50µm electrode gap might have the highest DEP effect. Each electrode is induvidualy accesible.

The first chip design, illustrated in Fig. 25, is based on this lab-on-a-chip device, in an experimental approach with individual electrodes that can be turned active by choice. This opens the possibility for individual electric field creation. Every following electrode chip has a dimension of 49 mm x 49 mm, based on the original glass wafer dimensions used for microfabrication, as well as every following chip contains 60 electrodes. All DEP chips were successfully fabricated using microfabrication techniques explained in chapter 2.3. The fabrication process determines the height of the electrode. Throughout this chapter, all electrodes have been designed to maintain a uniform height of 100µm.

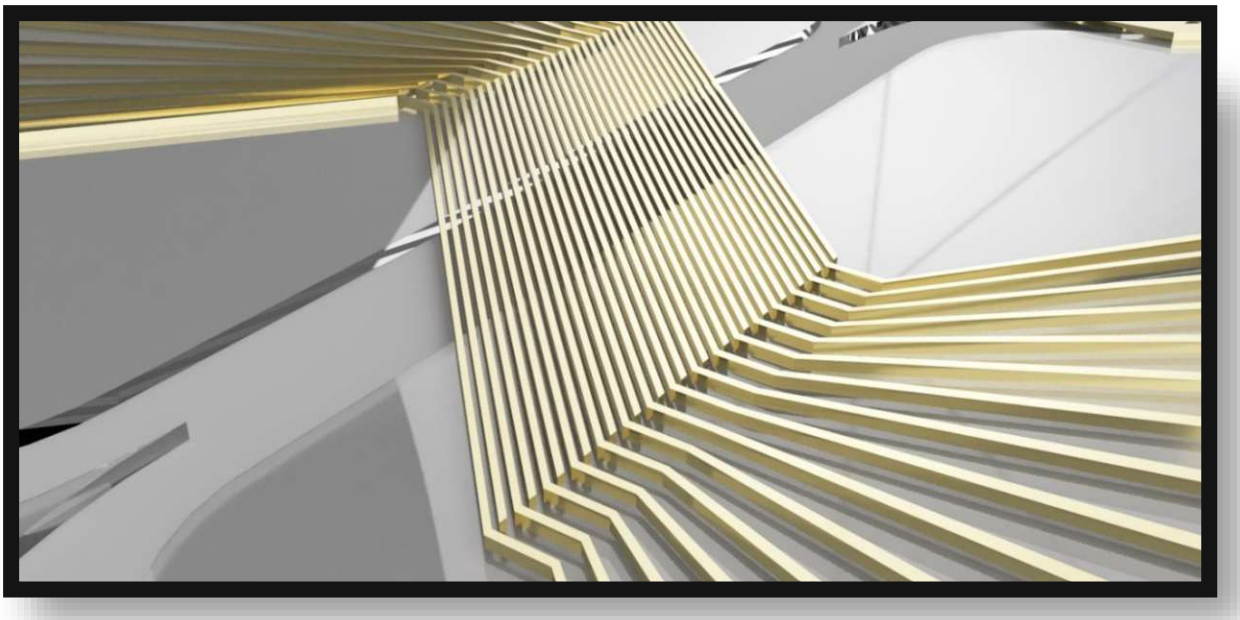

Figure 26: Focus in the rendered CAD-Model of DEP Diversion Chip 1, 50 µm IDES like electrode structures for DEP parameter estimation and later continuous flow deflection or sensing.

Within the zoom in the schematic CAD Model of the DEP Diversion Chip 1 in Fig. 26, the 50 µm IDES structure can be observed. It's worth noting that the purpose is the employment of DEP parameter observation, continuous flow deflection and later sensing. The electrodes lay over the chip but in the final fabricated lab-on-a-chip, the channel will be located above the electrodes.

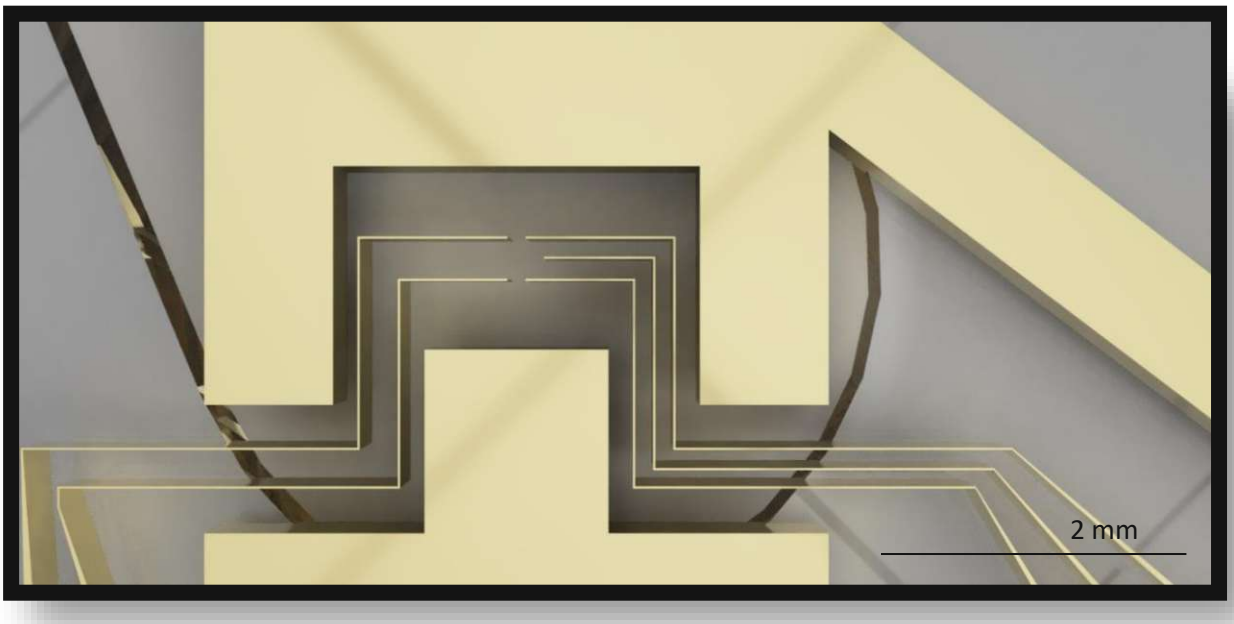

Figure 27: Zoom in the CAD-Model of the DEP Diversion Chip at the T- and U-Shape big Micropostioning Electrodes with a gap distance of 400 µm based on the design by Castellarnau et al.[14] The small electrodes in between are determined to measure the bioelectric activity of the spheroid.

A closer look at the CAD Model of the DEP Diversion Chip 1 is shown in Fig. 27, specifically focusing on the T- and U-shaped large micro positioning electrodes. These electrodes are designed according to the concept introduced by Castellarnau et al. [14], featuring a gap distance of 400 µm to prove the simulation results. Positioned amidst these larger electrodes are smaller ones, strategically placed to measure the bioelectric activity of the spheroid after positioning.

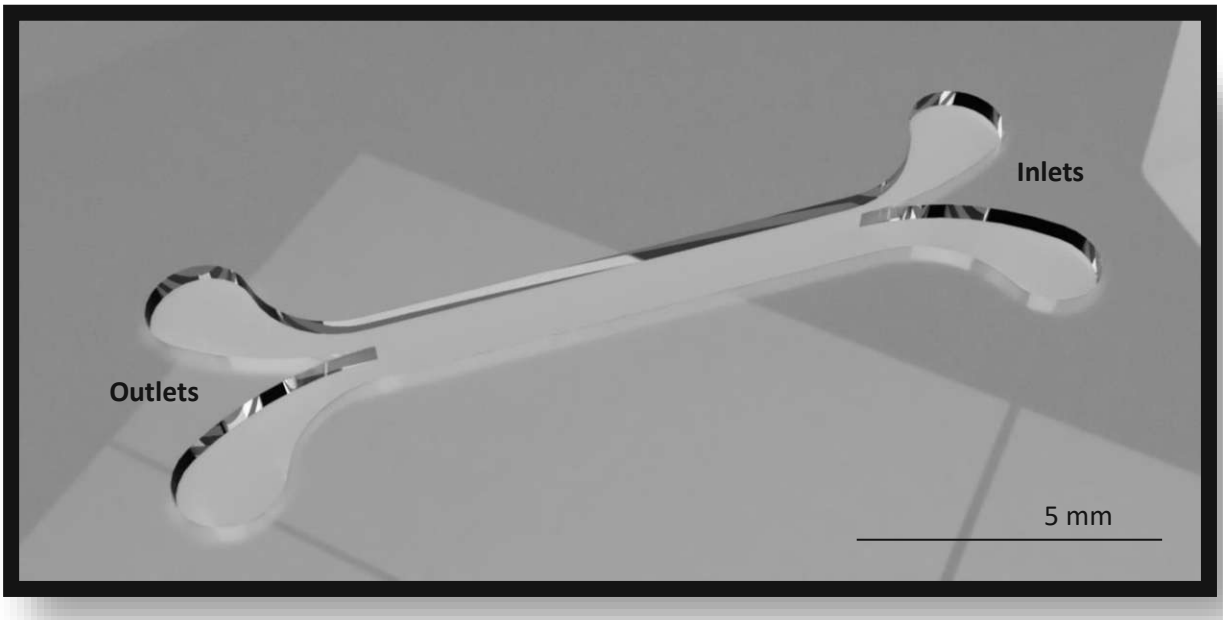

Figure 28: CAD Model of the DEP Diversion Microfluidic Channel. Inlets are shown on the right. The sample inlet is the smaller upper inlet and the bigger is for the buffer solution medium like in the schematic of Song et al. [31] The height of the channel is 420µm. The length of the junction is 10 mm.

The final microfluidic channel design observable in Fig. 28 consists of three layers which results in a height of 420µm. Furthermore, the channel carries two, in and outlets of 2 mm nominal diameter, followed by a junction on the left-hand side of Fig. 28 where the sample inlet is 50 µm and the buffer inlet 150 µm. The main channel is designed to be 1 mm wide, 140 µm high and 10 mm long. The disjunction visible in Fig. 28 on the left, equally divides the channel into two exits of 1 mm width. It is chosen to be wide to prolong the DEP effect and by that increase the quality of separation in fluidic flow.

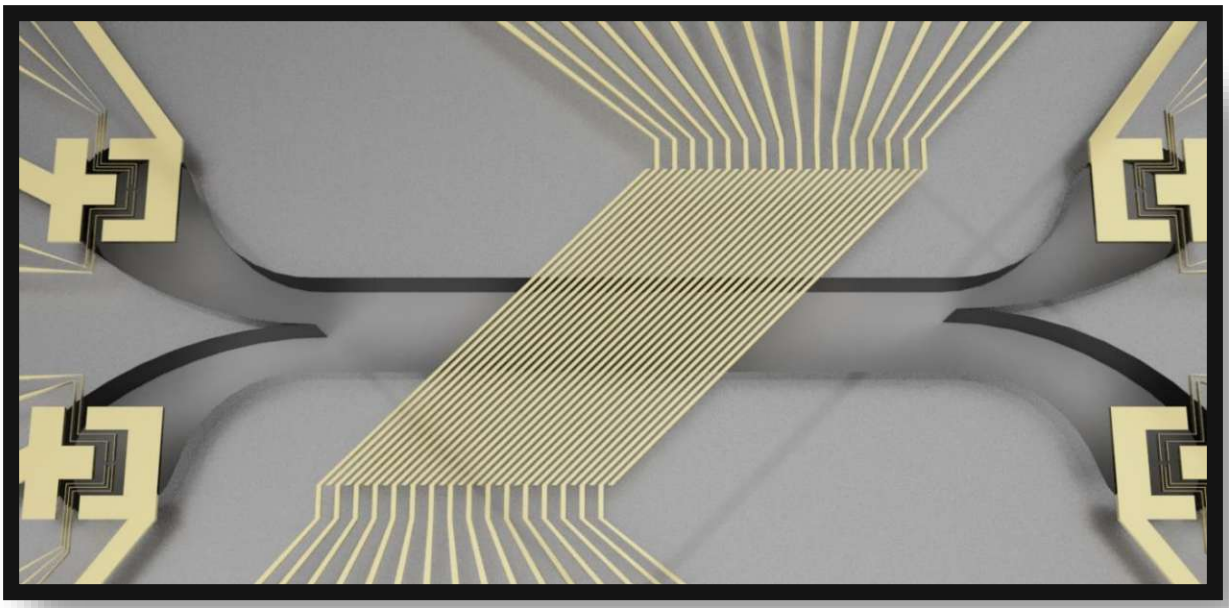

Figure 29: Rendered CAD Model of the DEP Diversion Chip 1 in Top View. The 45° angle between can be observed, like in the schematic by Song et al. [31]

In Fig. 29 the Schematic depiction of DEP Diversion Chip 1 in a top-view orientation, showcasing the electrode at a 45° angle to the microfluidic channel as in the schematic presented in Fig.2 by Song et al. [31] Here again the 50µm gap between the parallel electrode grid is visible what might have according to the results of the simulation in chapter 6.2.2 either have a good effect on the spheroids or no effect at all, therefore, a second chip was designed with a parallel electrode gap of 400µm, the "DEP Diversion Chip 2".

6.2.2 DEP Diversion Chip 2

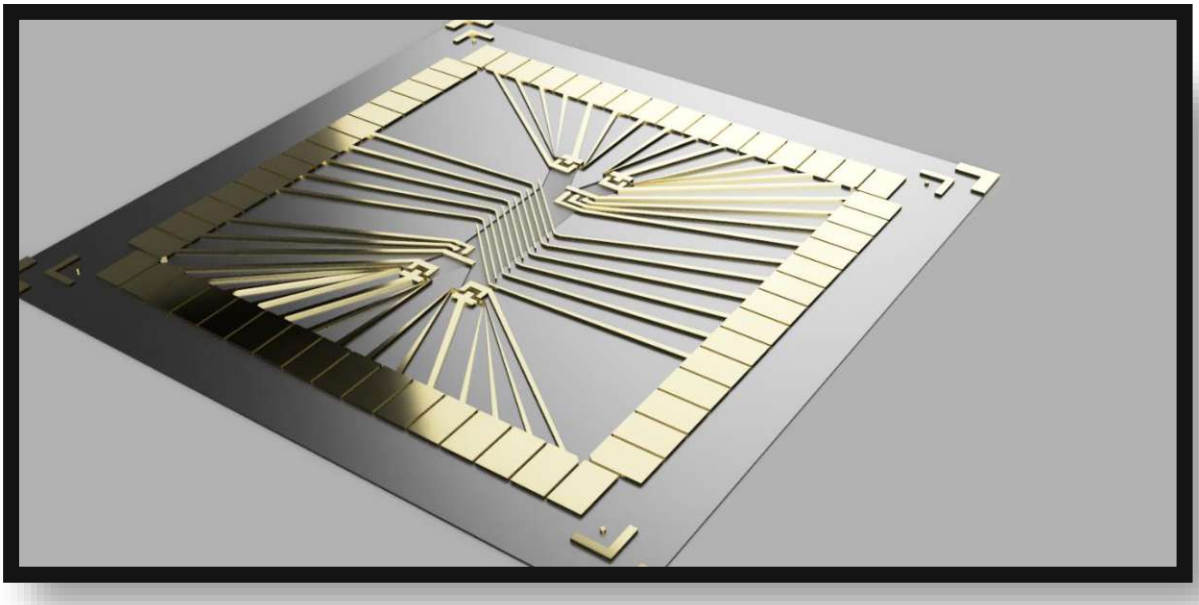

Figure 30: Rendered CAD Model of the DEP Diversion Chip 2. The outline of the chip is 49mm x 49mm, the design is based on the simulation result that a 400µm electrode gap should have a sufficient DEP effect. Each electrode is induvidual accesible.

The second chip's dimensions encompass a width and length of 49mm x 49mm like the first. Its design is derived from simulation results indicating that an electrode gap of 400µm should yield a satisfactory DEP effect. Therefore the parallel electrode gap is 400µm. Notably in addition to the U- and T-shaped electrodes described in the previous chip design, the chip incorporates an additional needle-like structure, strategically positioned to facilitate the determination of specific parameters. Each electrode on the chip is again designed to be individually accessible for enhanced versatility and experimentation.

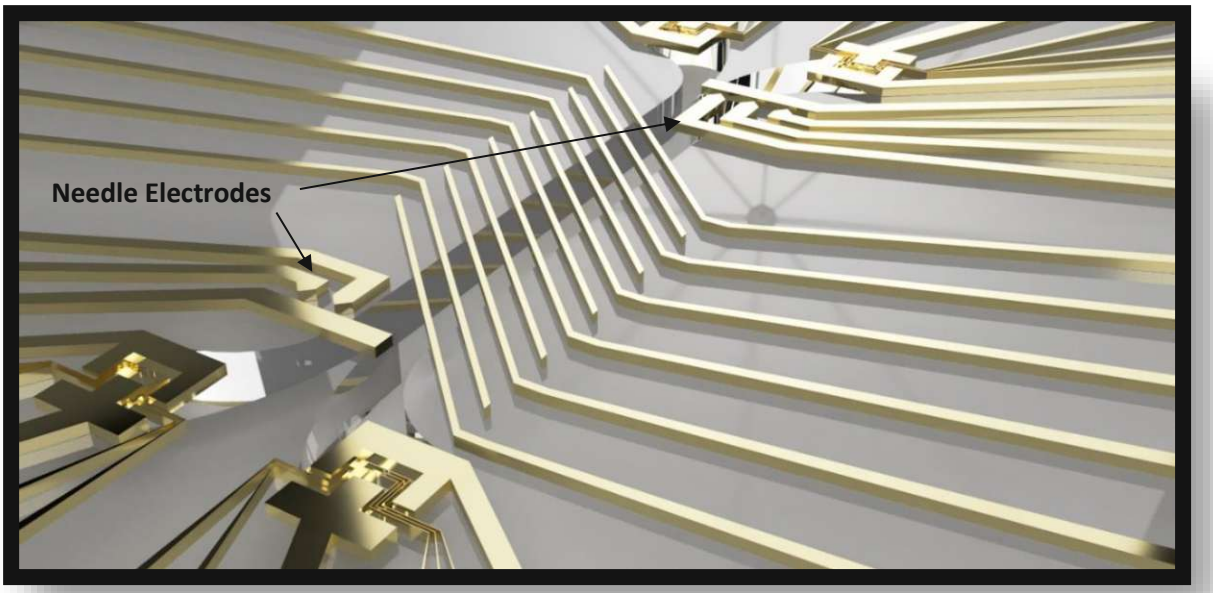

Figure 31: Rendered CAD Model of the DEP Diversion Chip 2 with scoping into the 400 µm distance gap of parallel electrodes and the thicker heavier needle like electrodes, once with two and once with three. The bridge to the needle tip is edgy, with the smallest electrode distance at their back (300 µm), a side needle to needle distance of (350 µm) and from edge to edge 460 µm. The needle tip to parallel bar distance is 250µm.

The provided Fig. 31 depicts the DEP Diversion Chip 2, offering a closer look at the 400 µm distance gap between parallel electrodes. This rendered CAD model also emphasizes thicker needle-like electrodes, showcasing two on the left and three on the upper right of Fig. 31. These needle-like electrodes feature multiple edges. The way to the needle tip is described as a bridge, based on the T- and U-shaped electrode principle to employ edges for a high electric field density investigation. The narrowest distance of 300 µm is at their back, the side-to-side distance between needles is 350 µm, with an overall edge-to-edge span of 460 µm. The distance from the needle tip to the parallel bar measures 250 µm. Especially, the needles shall help investigate the motion response of the spheroids by just placing spheroids on top in a surrounding 1mm PDMS well. The two DEP Diversion Chips are strategically designed for multiple purposes. At first, they serve to investigate the effects of DEP on spheroids and organoids, aiming to answer the research questions outlined in the goals of the thesis. The second purpose is for later investigation in fluid flow separation by deflecting only the subject with parameters of choice, explained in chapter 3.5 Microfluidics. The third chip is also designed to enable subsequent investigations, primarily focusing on the insertion of spheroids into small pockets.

6.2.3 DEP Insertion Chip Design

The third chip, the "DEP Insertion Chip," paves the way for further groundwork in subsequent studies. This chip is designed to facilitate the insertion and stabilization of spheroidal subjects into 250µm pockets. This setup is intended for therapeutic sensitivity testing and continuous recording of the bioelectrical response, expanding the potential applications for later research.

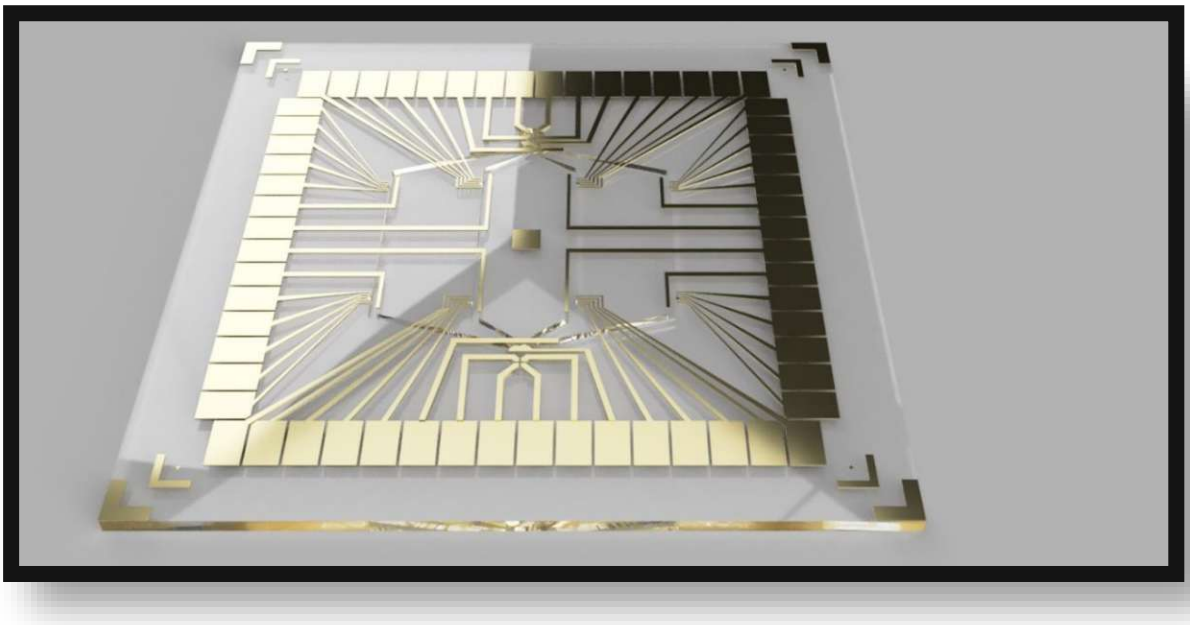

Figure 32: Rendered CAD Model of the DEP Insertion Chip Design. Inlets are positioned at the tips of the four needle electrodes on the top and bottom, designated for future electrorotation measurements. Additionally, eight electrode-surrounded pockets are strategically placed where multiple electrodes converge in front of straight electrode bars.

The third Chip, illustrated in Fig.32, contains one inlet and outlet with a diameter of 2mm. The inlets are located at the tip of the four needle electrodes at the top and bottom in Fig. 32 These electrodes are determined for later electrorotation measurements. In total eight electrode surrounded pockets are designed and visible in Fig. 35 at the locations where multiple electrodes focus in front of straight electrode bars. The electrodes' purpose is DEP insertion in the pockets as well as later impedance measuring the spheroid. Therefore, the electrodes must attract the spheroids utilizing negative DEP explained in chapter 2.1 "Dielectrophoresis". The design challenge for this chip revolved around efficiently accommodating the maximum number of pockets while adhering to a 5 to 1 electrode ratio, allowing subsequent subject measurement using the five electrodes.

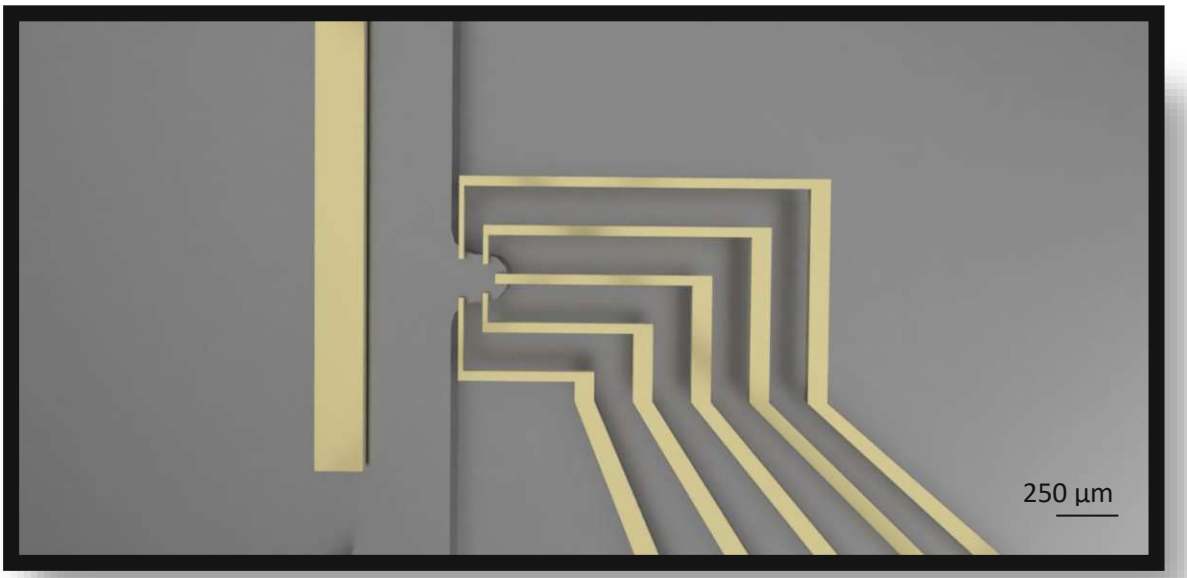

Figure 33: Rendered CAD Model of the DEP insertion chip single pockets. The 2D hemispherical pockets are designed for the deposition of cell clusters. Notably, the pocket width is 250 µm, accommodating spheroids up to 200 µm in size. The narrowest electrode distance between the larger and four smaller electrodes is 400 µm. The bigger electrode on the left has a width of 250µm and reaches 50µm in the channel. The five small electrodes have a width of 50µm.

The dimensions of the pocket for cell cluster deposit were designed in consideration of the cell pocket design by Hye-Jin Jin et al.[20] Observable in figure 15 the pocket width is 250 µm wide to accommodate *spheroids* up to a size of 200 µm. The previous pocket design study by Eilenberger et al. was integrated, resulting in the adoption of a 2D hemispherical pocket style for optimal containment of *spheroids* or *organoids*.[48] The narrowest electrode distance between the larger and the four smaller electrodes, as depicted in Fig. 33, measures 400 µm. The in- and outlets are 2mm wide. Its fundamental objective is to explore the feasibility of utilizing DEP to exclude spheroids from the flow within the channels and subsequently secure them in place. Positioning spheroids within designated pockets offers the anticipated advantage of localized confinement, enabling focused observation and analysis of their behavior under controlled conditions. This approach facilitates the precise manipulation and examination of spheroidal responses to external stimuli, fostering a more detailed understanding of their biological characteristics.

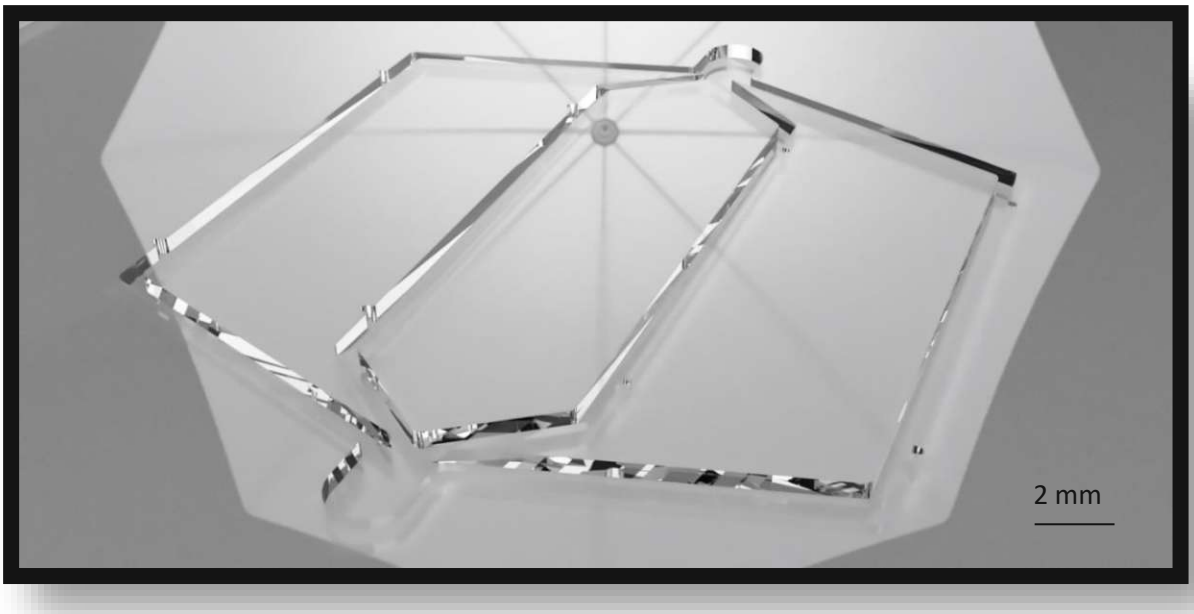

Figure 34: Rendered CAD Model DEP Insertion Chip Microfluidic Channel containing a junction into four separate channels. The channel's outer material visualization is glass, which results in reflections in the render while improving visibility.

The third Chip, illustrated in Fig. 34, contains one inlet and outlet with a diameter of 2mm. The microfluidic channel consists of four 1 mm wide 420 µm high and 15 mm long channels. The purpose of the channels is to evenly distribute spheroids across four channels, thereby maximizing the potential number of spheroids that can be captured, up to eight in total.

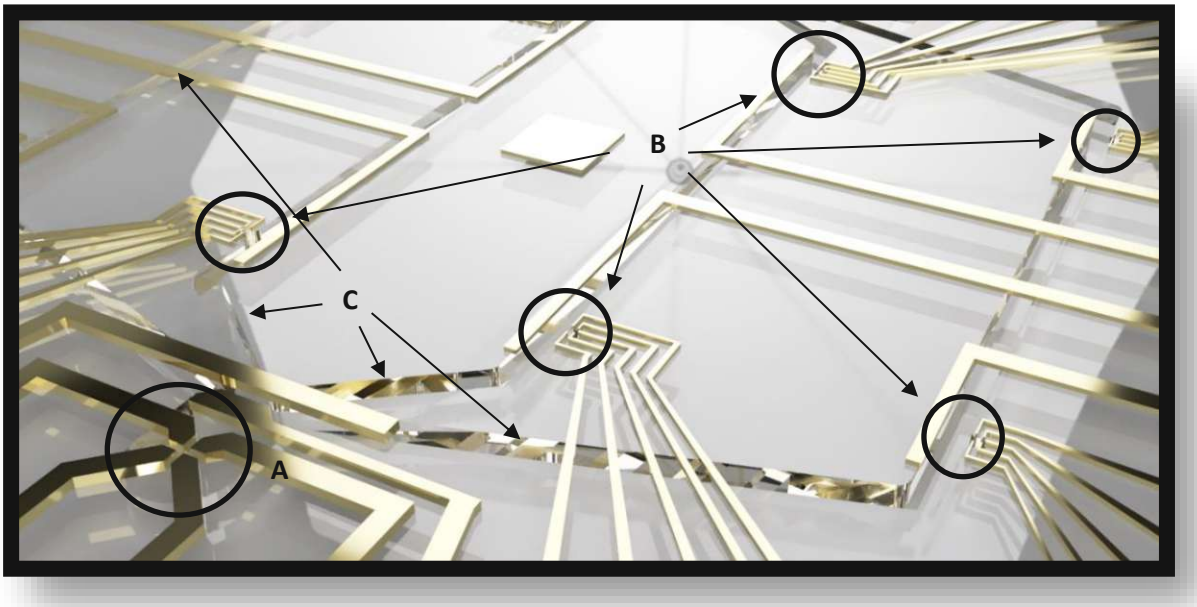

Figure 35: Further rendered Rendered CAD Model of the DEP Insertion Chip Design to clarify positions. The chip is shown in side view. Four needle electrodes for electrorotation measurements (A). DEP electrode pocket locations (B). Microfluidic channels (C). The channel's outer material is illustrated as glass for enhanced visibility.

6.2.4 Inhomogeneous Field Location

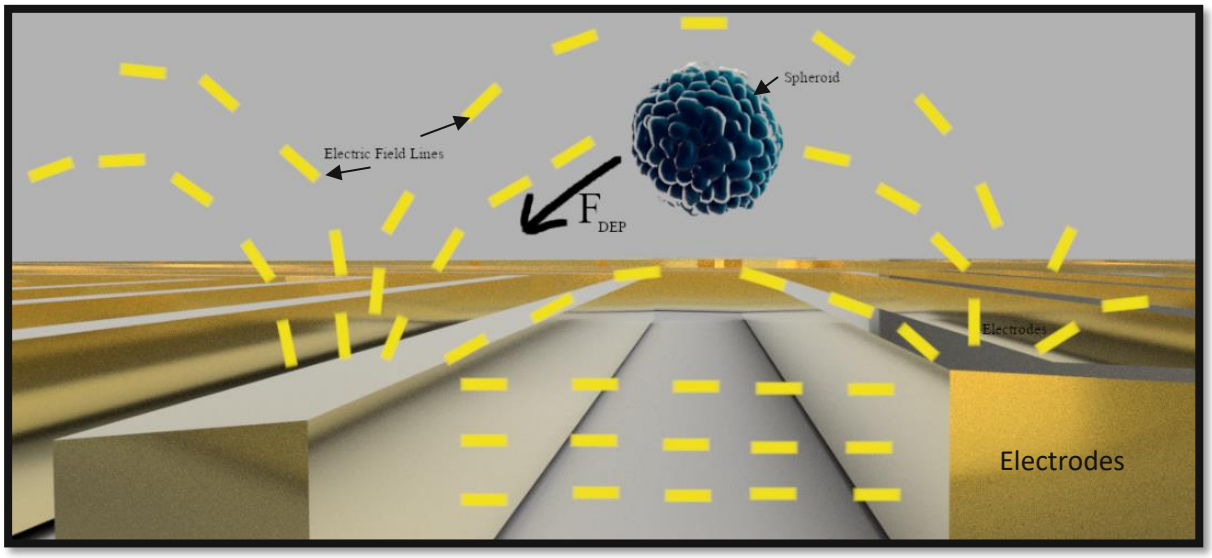

Figure 36: Schematic illustration of the spheroid above the parallel electrode grid with inhomogeneous field lines. The arrow indicates the direction of the resulting dielectrophoresis Force. The yellow lines represent schematically the electric field lines.

In section 2.1 is explained that for DEP an inhomogeneous field is located. Therefore, it's viable to understand where on the designed chip the inhomogeneous field is located, where it is narrower and wider to estimate to direction of the force vector. Usually, an electric inhomogeneous field design is achieved by having spatial variation between the electrode masses like Fig. 3 in section 3.1 the highest field density is then at the edges of the electrodes. The electrodes in the center of DEP Diversion chips are parallel and in between the electrodes is a homogenous field. In a truly homogeneous electric field, the net force experienced by particles or cells would be zero, as there is no spatial variation in the electric field the electric field gradient is zero.[14] However, as in Fig. 36 visible above the electrodes an inhomogeneous field is present. Ideally, the particle doesn't get stuck between the electrodes but travels above the electrodes as shown in Fig. 2, further illustrated in section 3.1 by Song et al. [31]. The yellow stitched lines are the electric field lines influencing the *spheroid*. The p-DEP force directs the particle towards narrower equipotential lines at the electrode surface, consequently, n-DEP repels the sphere from the electrode. [14] This concept is later proven in chapter 6. In a microfluidic approach, the electrodes act as side rails by attracting the cells or *spheroids* via p-DEP and translating them sideways in the microfluidic flow. This works only in a flowing medium, in static the subjects get trapped at positions of narrower or wider field locations. This concludes the design of the chips. The design specifications off all chips are documented in the following table:

Table 2: DEP Chip Overview

	Diversion Chip 1	*Diversion Chip* 2	*Insertion Chip*
Channel Width	2 mm	2 mm	0.5 mm
Electrode gap	50µm	300- 400 µm	400µm

Having discussed the designs and their purpose, let's now shift our focus to the presentation of the finalized products.

6.2 Manufactured Chips

All designs were realized through the application of either xurography, as detailed in section 4.4.2, or PDMS fabrication methods, as explained in section 4.4.3. The finalized products are showcased in the subsequent subchapters for visual reference.

6.2.1 Xurography Chips

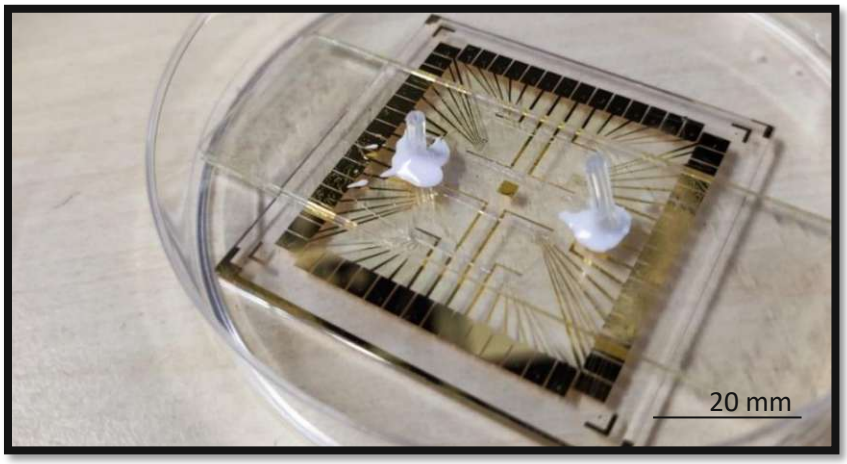

Figure 37: Photograph of the DEP Insertion Chip fabricated by Xurography.

The alignment is hardly visible for the DEP Insertion Chip shown in Fig. 37. The positioning by the case and hand was not sufficient for the complex channel geometry which resulted in no DEP spheroid insertion functionality. Even though the chip was used to investigate side effects like electrolysis described later in chapter 6.4.3. A mask aligner could be used to improve alignment, because of its micro precision positioning ability.

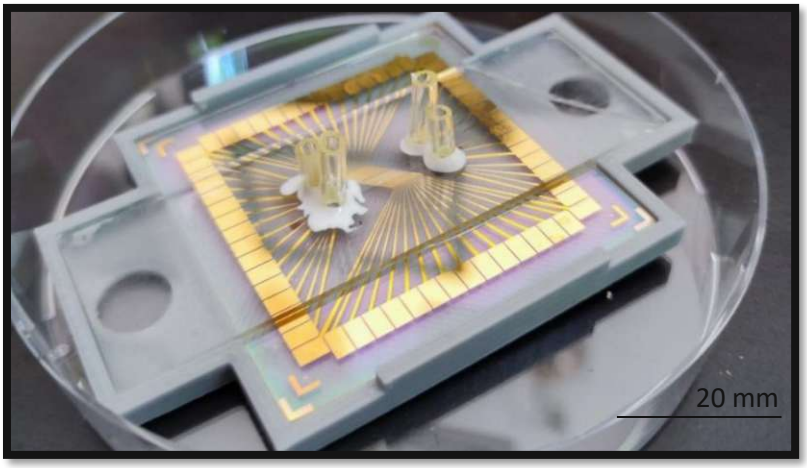

Figure 38: Photograph of the DEP Diversion Chip 1 with ports inside the assembly case fabricated by xurography.

Xurography is only suitable for simple channel structures such as those found in the DEP Diversion Chips with ports shown in Fig. 38, where precise positioning on electrodes is not necessary. The diversion chip microfluidic main channel has a 2 mm wide, 140 µm high and 10 mm long main channel in the xurography version because of fluidic dynamic estimations explained in the methods chapter 4.2. and an adhesion foil height of 140µm.

6.2.2 PDMS Chips

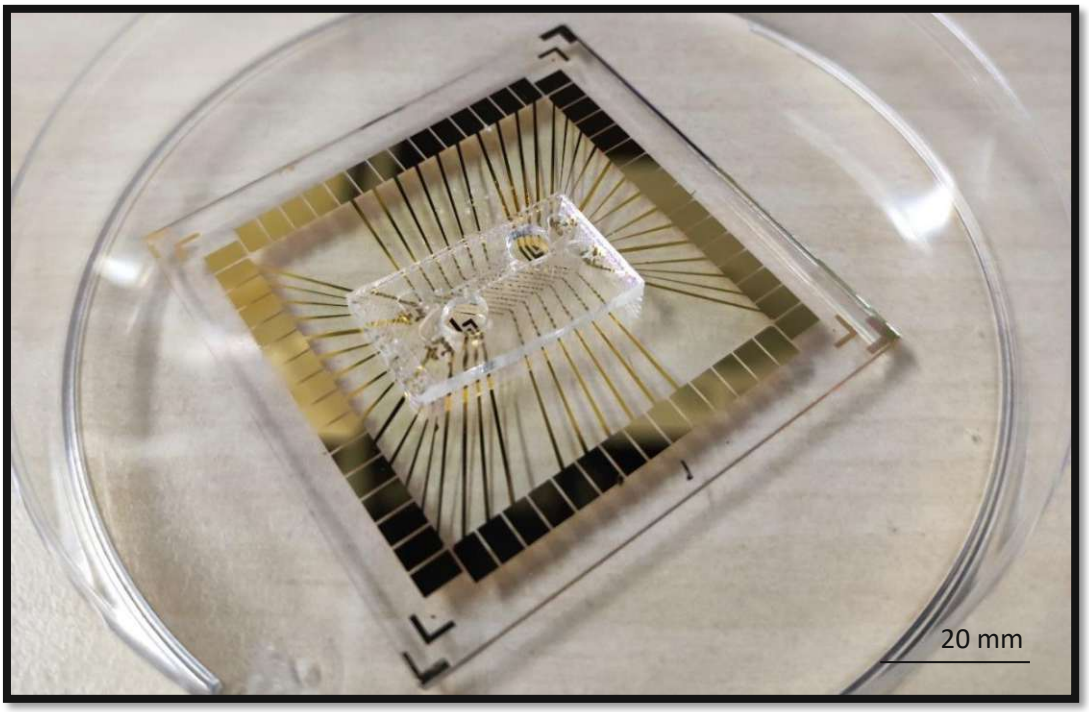

Figure 39: Photograph of the PDMS reservoir block on DEP Diversion Chip 2

The alignment process using a mask aligner was successful and resulted in a LOC shown in Fig. 37, yet certain challenges persist in terms of adhesion between the PDMS and glass slide. The resulting microscope images are somewhat compromised by PDMS-induced light reflections or minor bubbling artifacts. In comparison to xurography, in this chip type all electrode pads are accessible for connection with the specially developed frequency generator adapter explained in the next section.

6.3 Chip-to-Frequency Generator Periphery

DEP depends on a generated AC field between electrodes. To establish a reliable connection between the frequency generator and MEA, three adapters were designed and fabricated, as explained in section 4.4. The finished products are documented here.

6.3.1 Plant Adapter Plug

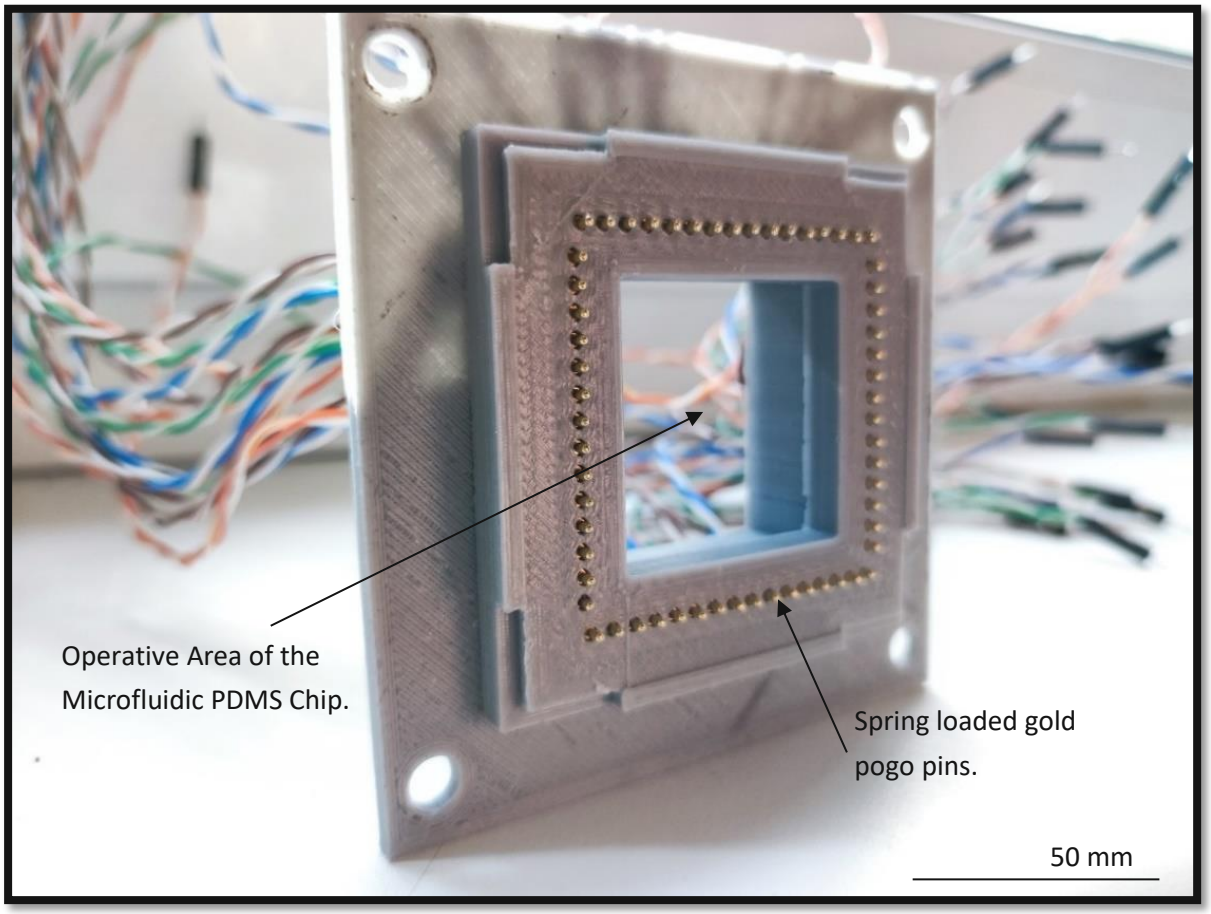

Figure 40: 60-Pin Plant Adapter Plug for the PDMS version of the DEP chips. In front are the opposing spring loaded golden pins visible in the background twisted cable wire with Dupont ends.

The 60-Pin Plant Adapter Top-Plug is designed for the PDMS version of the DEP chips and is visualized in Fig. 40. This adapter can be securely attached to a base using four screws, exerting pressure on the pins that subsequently press against the electrode pads of the Microelectrode Array (MEA). The connection was excellent, only carrying resistance through the cable seen in the background of Fig. 40. Even though the choice of cable and DuPont adapter opens the possibility of connecting the adapter to breadboards and further to an ADC converter to measure resistance or impedance. This ADC converter can then be further connected to a microprocessor.

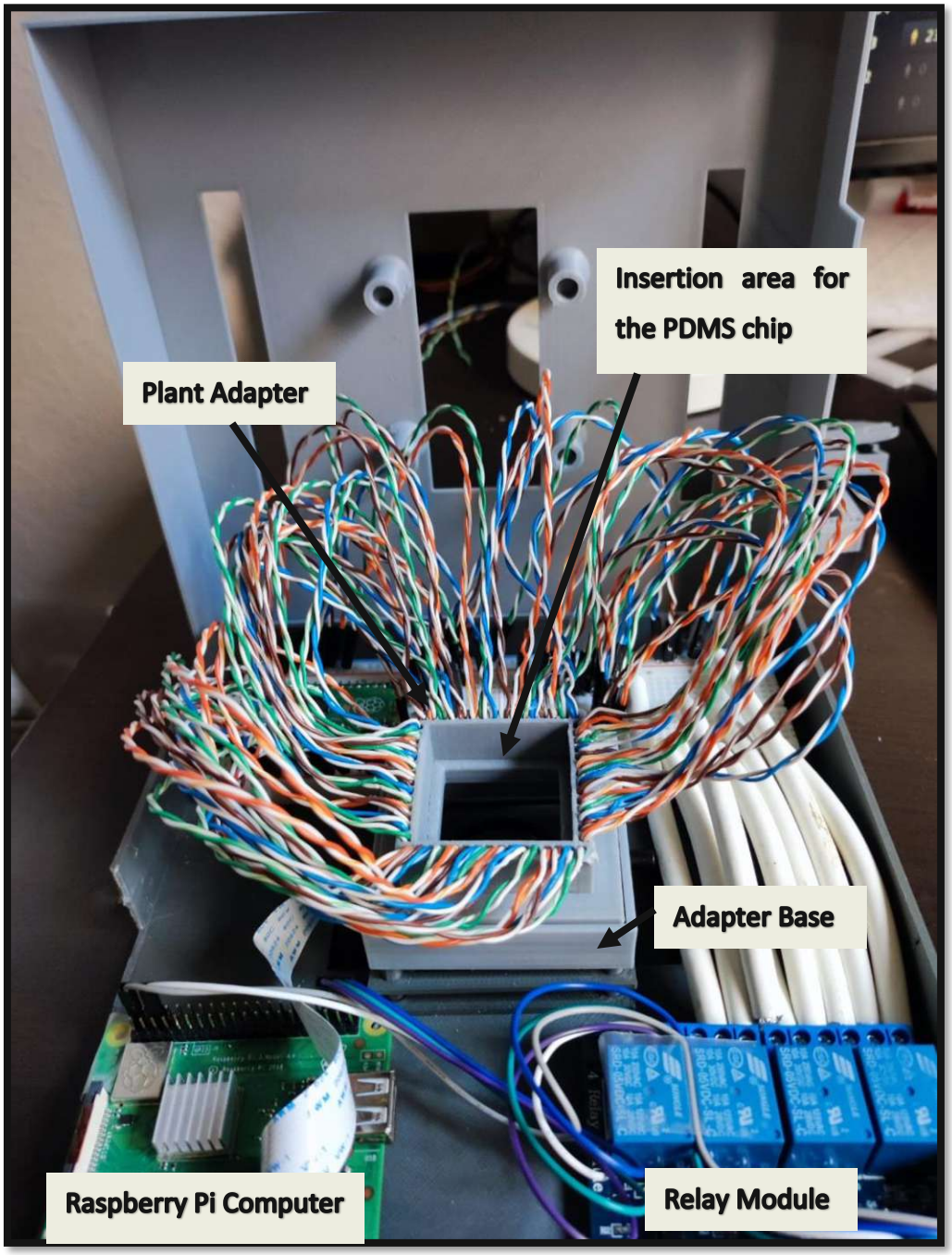

Figure 41: Embedded Set up with the plant adapter containing: A Raspberry Pi model 3A+ on the left, a relay module on the right. The machine is double the size a common laptop.

To fully automate the process or to control it via a Graphical User Interface (GUI), an embedded device was assembled, programmed, and tested (Fig. 41). A Raspberry Pi model 3A+ serves as a standalone computer to capture images with an integrated camera, control, and record over a GUI the pulse length, switch the polarity via the relay module on the right, measure resistance or impedance with an analog-digital-converter (ADC) on the breadboard and access the system via SSH or WIFI inside an incubator. To place it and access it remotely it can be powered by a power bank supply. The full set up is not necessary for this study now but serves as a concept for later studies that require placement inside an incubator or automation. As the Plant adapter worked efficiently with the PDMS style chips there was only the need to design an adapter for the xurography style chips.

6.3.2 Junction Adapter

For chips fabricated using the xurography technique, the initial connector design was the junction adapter. This adapter's concept involved applying pressure manually instead of using screws, allowing for greater movement flexibility akin to using a microscope slide in conjunction with a microscope.

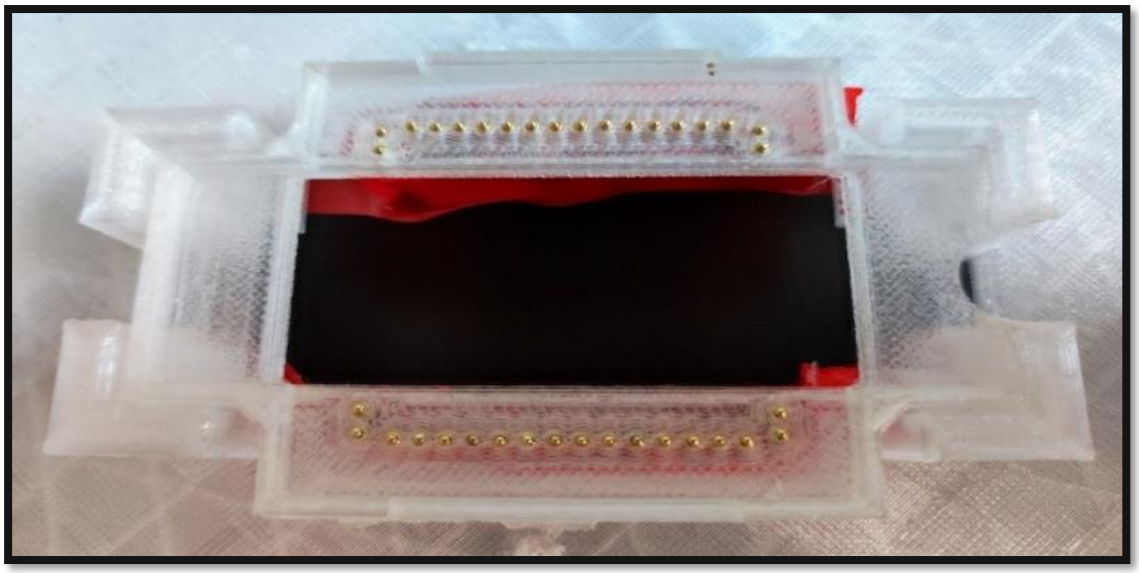

Figure 42: Photograph of the Junction Adapter in close view. Short spring loaded pins are facing upwards the end was insulated using insulation tape visible as red. Some pins contain a lower height than others.

In Fig. 24 is a close view of the Junction adapter for the xurography style chips is displayed. Shorter Pins were incorporated but failed to deliver a stable connection, some even had no connection.

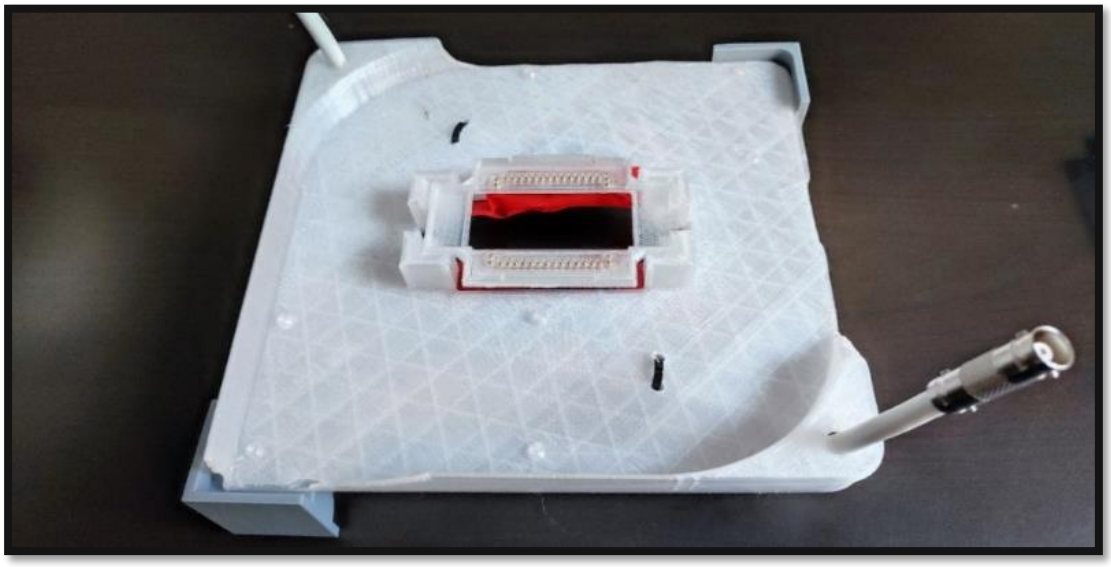

Figure 43: Photograph of the fully displayed Junction Adapter as overhead version. On the right is a BNC Adapter visible, the adapter was implemented for less noise on the connection.

The full display of the Junction Adapter is displayed in Fig. 43. Here the xurography style chips were placed on the Adapter to have the electrodes on top and prevent cells or spheroids from falling between the electrodes of the chip. The focal point was too high for good microscope images. There was a need for another adapter with a more reliable connection to utilize the xurography style chips.

6.3.2 Spider Adapter

Since the initial xurography adapter did not yield the desired outcome, a subsequent adapter was devised, drawing inspiration from the principles of the plant adapter. This new design incorporated the use of screws and elongated spring-loaded pins to achieve the intended functionality.

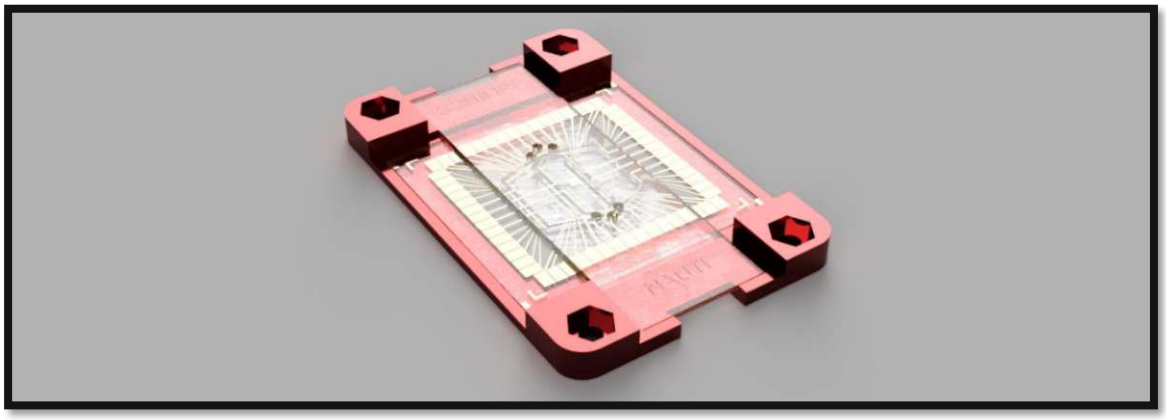

Figure 44: Rendered CAD Model of the Spider Adapter Base, containing an inserted DEP Insertion Chip. Four grooves are located at the edges for screw-nuts to be inserted and fixated by pressing them in.

Fig. 44 depicts a rendered CAD Model of the Spider Adapter Base, featuring an inserted DEP insertion chip. This configuration offers improved focal precision and enhanced flexibility. Due to the compact size of the adapter the chip can be easily handled with a single hand under the microscope.

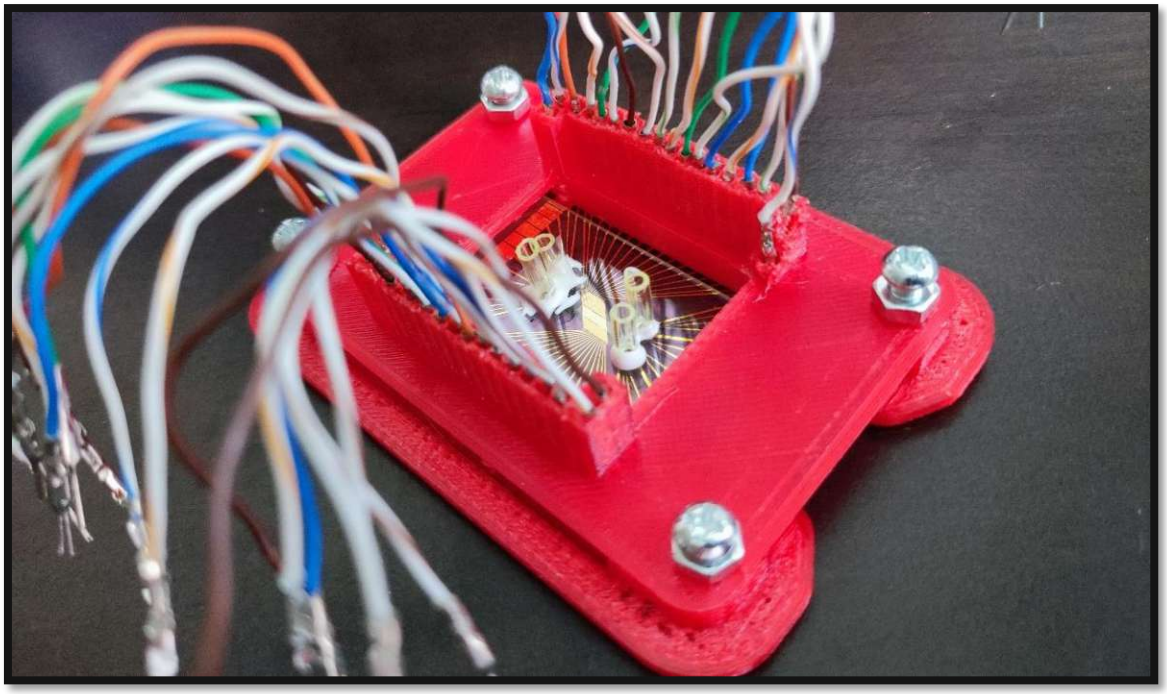

Figure 45: Photograph of the Spider Adapter with inserted DEP Diversion Chip 1. Each of the cables can individually be connected to the frequency generator.

Fig. 45 is a photograph of the finished Spider adapter with inserted DEP Diversion Chip 1. The voltage connection was excellent due to the four screws applying pressure on the chips MEA via the pins. With the presentation of the adapters covered and one adapter for PDMS- and one for Xurography style chips available, the focus shifts to introducing the results of the experiments conducted using these adapters.

6.4 DEP Experimental Results

In this chapter, we delve into the outcomes of the experiments conducted to examine the effect on human tumor spheroids on an AC field frequency variation. First the results of the spheroid DEP analysis are presented, followed by the cellular analysis results and finally side effects are shown.

6.4.1 Spheroid Motions

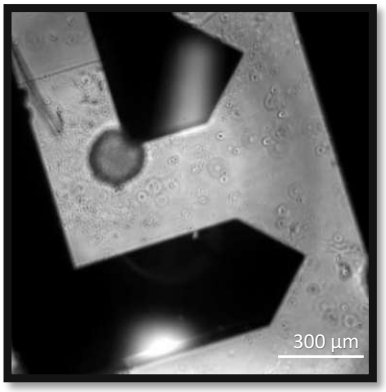

Figure 46: Microscope image of an Spheroid (slight gray) between elcetrodes (black) at 10V 20 Mhz,

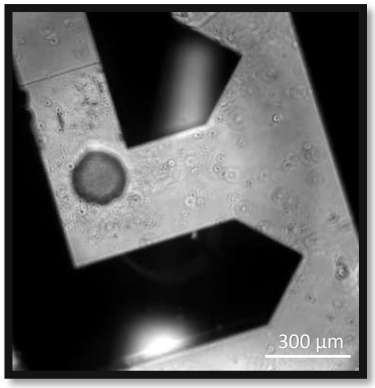

Figure 47: Spheroid at 2 MHz, during 4 s the spheroid moved between electrodes.

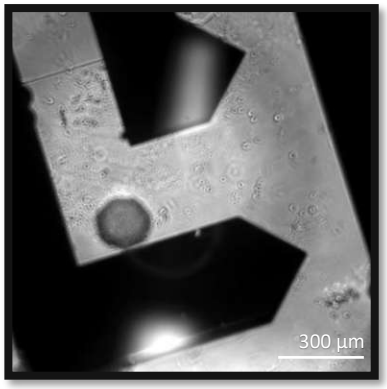

Figure 48: Spheroid between electrodes at 200 kHz, at 11 s the spheroid traveled further.

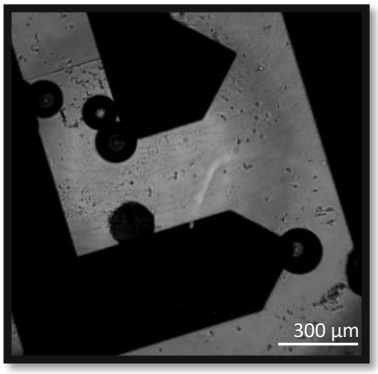

Figure 49: Spheroid and electrolysis bubbles between elcetrodes at 200 kHz. at 22 s.

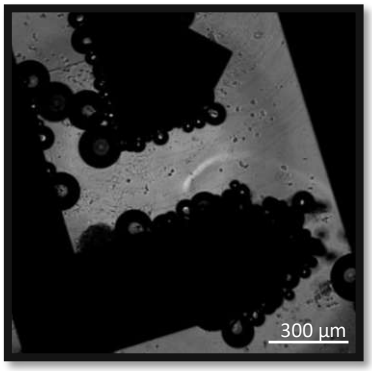

Figure 50: An amount of electrolysis bubbles from the electrodes at 200 kHz, at 23 s.

DEP Diversion Chip 2. experimental results are shown. Fig. 46 represents the initial position of the spheroid in a PDMS surrounded well. Therefore, in the resulting inhomogeneous field, the maximum electrical field density appears at the tip. At the corner the electrical field is the lowest. By n-DEP the spheroid is supposed to repel from the electrode. At 20 MHz the 150 µm spheroid gets repelled from the electrode in about 4s as observable in Fig. 47. The spheroid remains at this position when the field is turned off. When switching the frequency to 2 MHz the surrounding medium begins to turbulently flow but the spheroid remains between the electrodes. Fig. 48 shows the result of switching to 200 kHz, the spheroid is moving further to the corner but gets deflected by the induced fluidic turbulences. As depicted in Fig. 49 and 50, at the electrode edges, gases are slowly produced at 200 kHz at edges and extensively at 20 kHz. The experiment was repeated with spheroids of different diameters to investigate size exclusiveness for the purpose of inserting spheroids in sizes of choice in pockets.

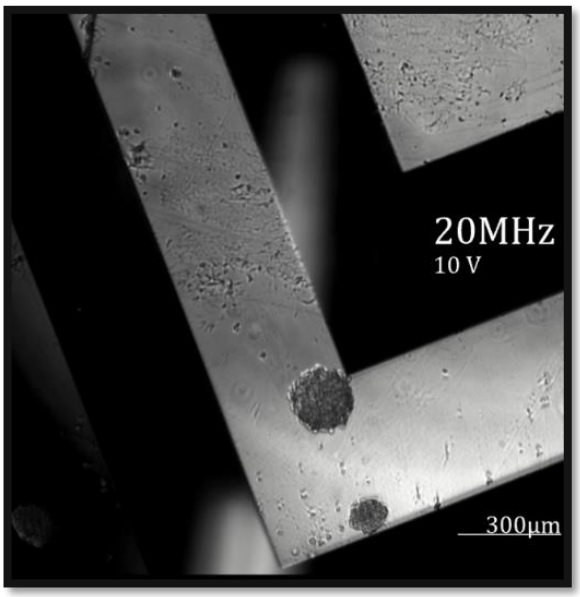

Figure 51: Microscope Image of two Spheroids, 150 µm and 100 µm in diameter. Initial state of experiment.

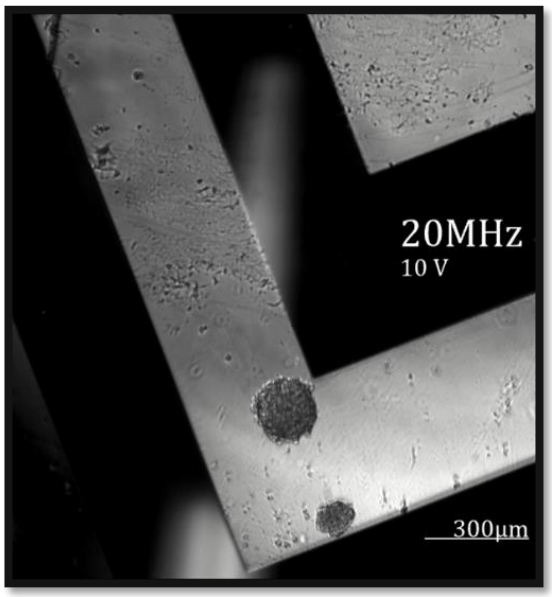

Figure 52: Microscope Image of two Spheroids, 150 µm and 100µm in diameter. AC voltage is applied on elcetrodes at 20 MHz, at the time point of 2 s. The bigger soheroid got slightly detached from the tip.

The initial position of the spheroids is shown in Fig. 51. One spheroid has a size of approx. 150 µm and the other one a size of approx. .100 µm. At 20 MHz only the 150 µm diameter *spheroid* gets repelled (Fig. 52).

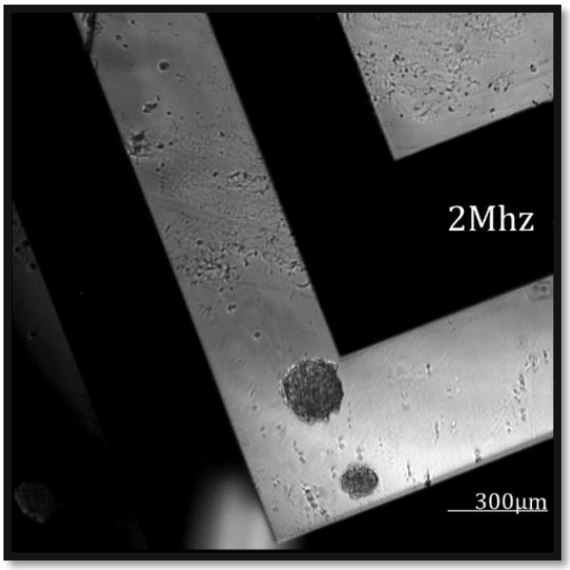

Figure 53: Microscope Image of two Spheroids, 150 µm and 100µm in diameter. 10V AC voltage is applied on elcetrodes at 2 MHz, at the time point of 1 seconds.

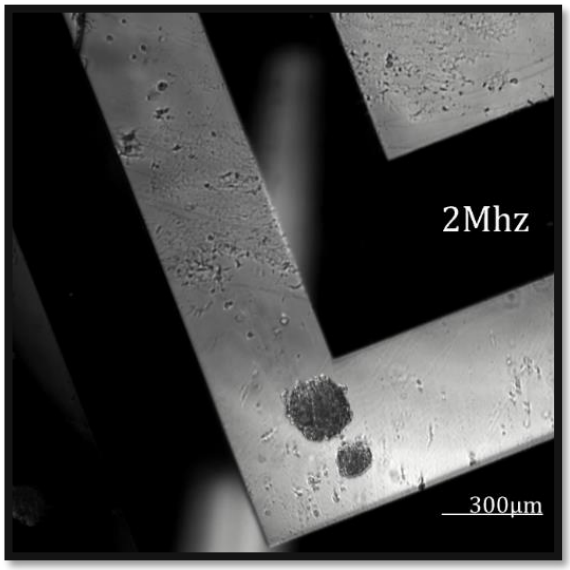

Figure 54: Microscope Image of two Spheroids, 150 µm and 100µm in diameter. 10V AC voltage is applied on elcetrodes at 2 MHz for 4 seconds.

At 2 MHz both *spheroids* get impulsively repelled as visible in Fig. 53. They both travel further and remain between the electrodes as depicted in Fig. 54. The voltage was further reduced what resulted in electrolysis visualized next.

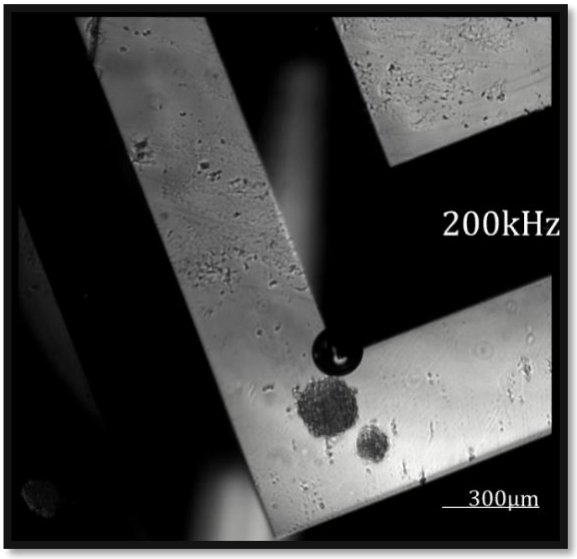

Figure 55: Microscope Image of two Spheroids, 150 µm and 100µm in diameter. 10V AC voltage is applied on elcetrodes at 200 kHz. Bubble growth at the edge of the electrode is shown.

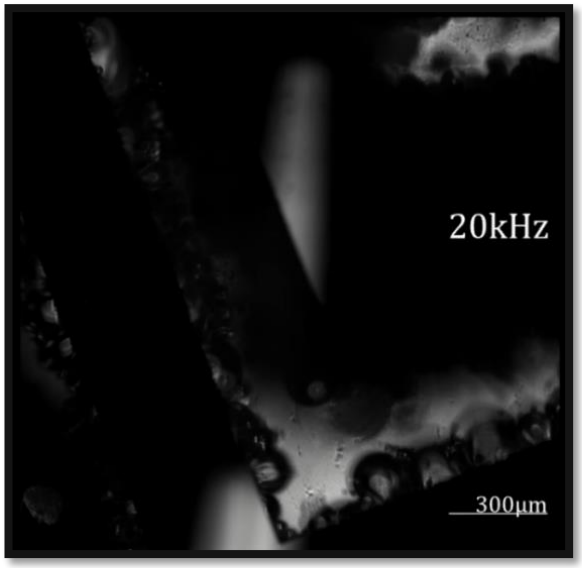

Figure 56: Microscope Image extensive electrodlysis. 10V AC voltage is applied on elcetrodes at 20 kHz.

At 200 kHz the bigger *spheroid* gets attracted towards the electrodes but gets pushed back by an electrolysis bubble at the electrode edge observable in Fig. 54. At 20 kHz extensive electrolysis takes place (Fig. 55). The results show that size exclusive effects are possible at the right frequency and that 10V AC field frequencies below 200 kHz led to electrolysis.

The experiment was repeated with *caco-2 cell cluster* to observe if the effects are the same on non´-aggregate cluster and determine the electrode parallel grid DEP functionality. Hisexperiment was carried by the PDMS Version of the DEP Diversion Chip 2.

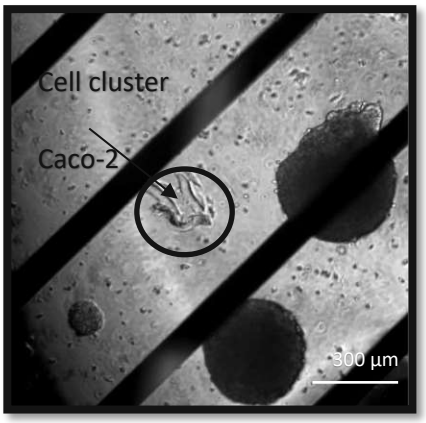

Figure 57: Microscope Image of Spheroids attached to electrodes and caco 2 cell cluster on an electrode grid at 20 MHz 0s

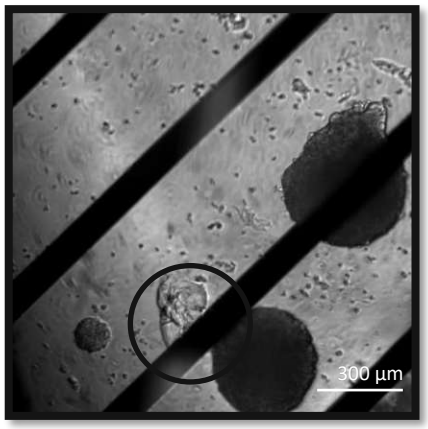

Figure 58: Microscope Image of Spheroids and caco 2 cell cluster attached in an electrode grid at 20 MHz 4s

In this experiment *caco-2* cells formed a cluster observable in Fig. 57. At 20 MHz a combination of generated fluidic flow and attraction from the active electrode where two spheroids are attached, moves the approx. 100 µm in diameter *caco-2* cluster towards the electrode. The cluster folds and remains at the electrode as depicted in Fig. 58.

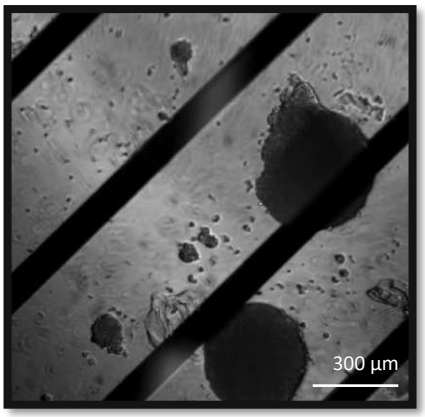

Figure 59: Microscope Image of Spheroids and caco 2 cells cluster attached in an electrode grid at 2 MHz 6s

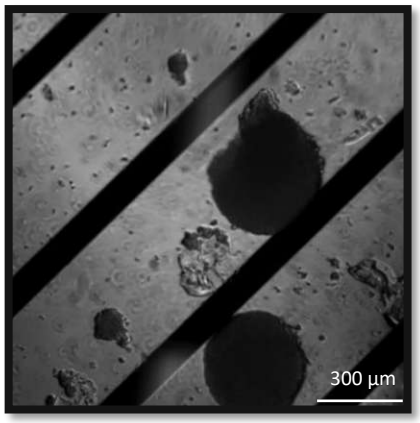

Figure 60: Microscope Image of Spheroids and caco 2 cells cluster reppeled from an electrode grid at 200 kHz 10s

At 2 MHz no further motion is observable (Fig. 59). At 200 kHz the cell cluster gets slowly repelled from the active electrode as observable in Fig. 60.

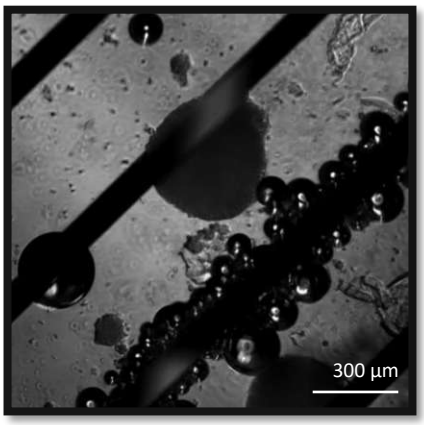

Figure 61: Microscope Image of Spheroids, caco 2 cell cluster and electrolysis bubbles in an electrode grid at 20 kHz 0s

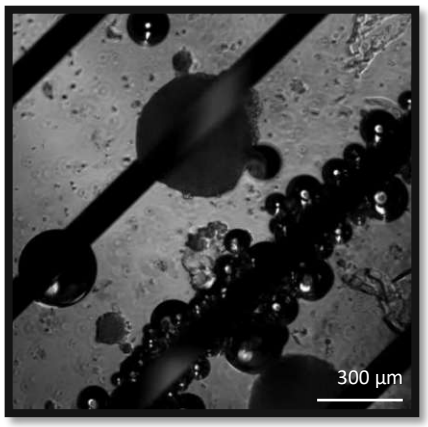

Figure 62: Microscope Image of Spheroids and caco 2 cell cluster extensive reppeled in an electrode grid at 20 200 kHz 2s

Observable in Fig. 61 at 20 kHz electrolysis bubbles appear at the active electrode. Visible in Fig. 62, the electrodes repel generated bubbles and the *spheroids* along with it. Across all the images, a 100 µm-sized spheroid nonchalantly resides within the slightly heated whirlpool, seemingly unimpressed by the emergence of gases, perhaps due to its entrapment via negative dielectrophoresis.

6.4.2 Cellular Motions

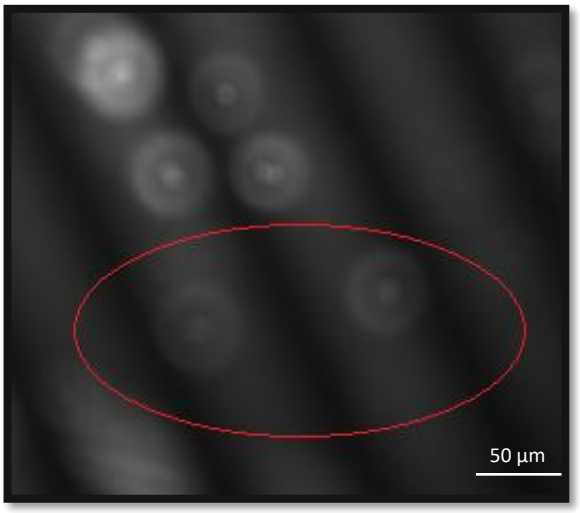

Figure 63: Microscope Image of HT29 Cells in DEP Diversion Chip 1 cells are randomly distributed with no applied AC field.

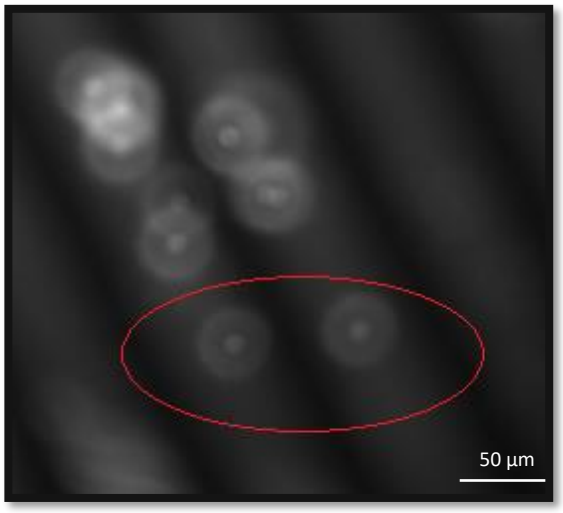

Figure 64: Microscope Image of HT29 Cells in DEP Diversion Chip. The cells are closed to the active electrode, which carries 10V at 200kHz.

To check the DEP functionality cell experiments were conducted. Fig. 63 represents the recorded image with no applied electric field, serving as an initial reference. Fig. 64 depicts the arrangement of *HT29 cells* after 1 second of applying 200 kHz at 10V peak-to-peak. The images are blurred because of the use of a high base for the adapter but they still show that the cells have been expelled from the electrode, which aligns with the expected behavior based on the negative Clausius-Mossotti factor for cells at this frequency. At 4 MHz, no cell movement was observed, which is consistent with the anticipated behavior at this higher frequency. In contrast, at 20 MHz, no contrary movement was observable. It is noteworthy that higher frequency experiments were conducted towards the end of the trial. After approximately 20 minutes of rearranging the cells by pipetting, a large cluster of cells formed, subsequently plugged the channel, and rendered the chip further unusable. Next a bigger electrode distance was observed with the DEP Diversion Chip 2.

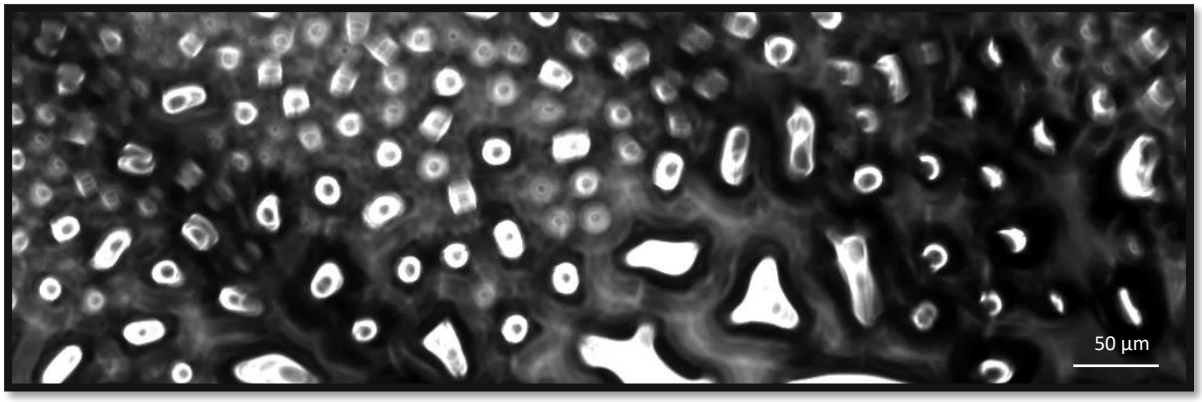

Figure 65: Microscope Image of Chip Surface Droplets on top oft he DEP Diversion Chip 2 microscope glass slides

The next cellular experiment result presented was carried out with the DEP Diversion Chip 2 in the microfluidic set-up to allow controlled insertion of a certain number of cells. The increased spacing between the electrodes to 400 µm resulted in no movement of both human colon adenocarcinoma cells and human mesenchymal stem cells. However, by increasing the cells' velocity stepwise by increasing the applied pressure one of the ports ruptured under a pressure of 200 mbar. This led to the leakage of the cell medium onto the glass layer, as depicted in Fig. 65.

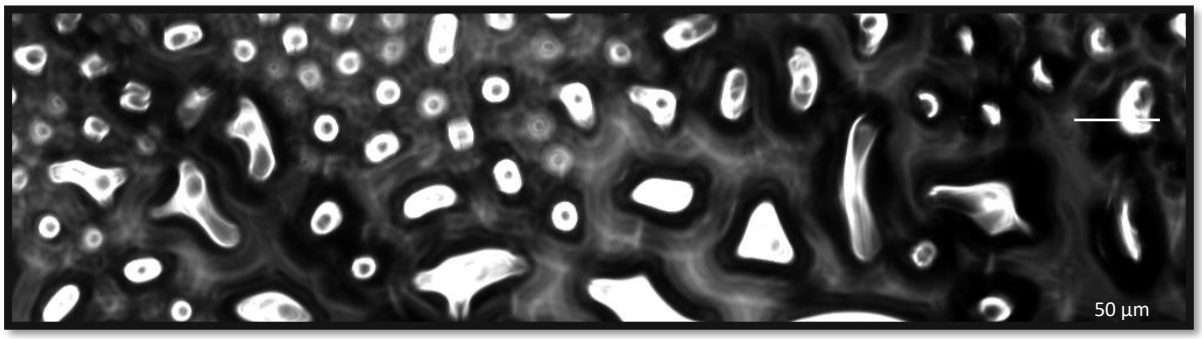

Figure 66: Microscope Image of Merged Droplets by electric field effects on top oft he DEP Diversion Chip 2 microscope glass slides.

Following the leakage, a peak-to-peak voltage of 10V was applied at 20 MHz and the camera was focused on the top of the chip where small droplets of the leaked cell medium exhibited a stepwise alignment, observable in Fig 66. Along the electrode rails, these aligned droplets merged, forming larger droplets. This phenomenon indicates the influence of the electric field even through the glass slide.

The results using the DEP Insertion Chip with *hMSCs* are presented next.

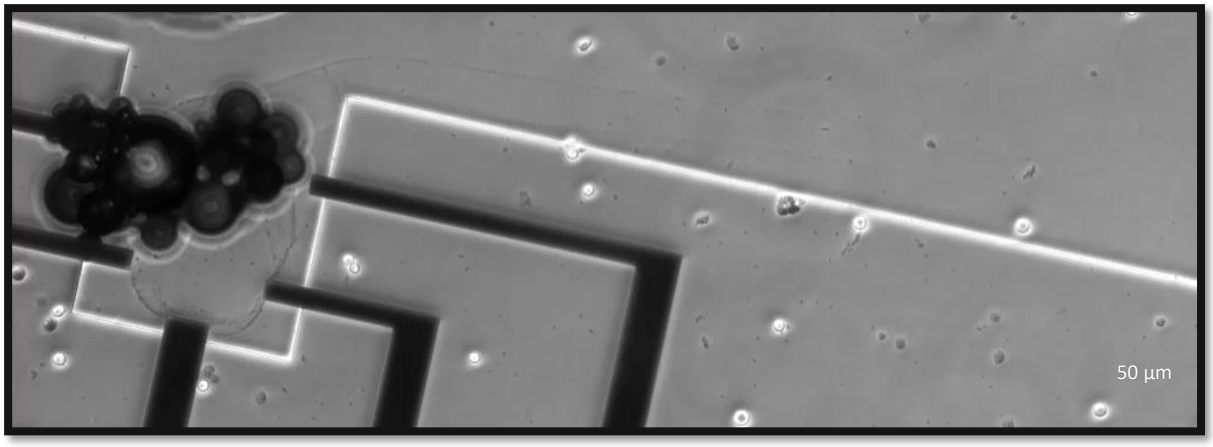

Figure 67: Microscope Image of the DEP Insertion Chip Cluster Formation after 10s at an applied AC field of 20 kHz.

At 5V Amplitude and 20 MHz no visible effect on any cells was pictured at the electrode distance of 400 µm, going stepwise down to 20 kHz and using a lesser electrode distance of 150 µm resulted in a cluster formation at the electrodes visible in Fig. 67.

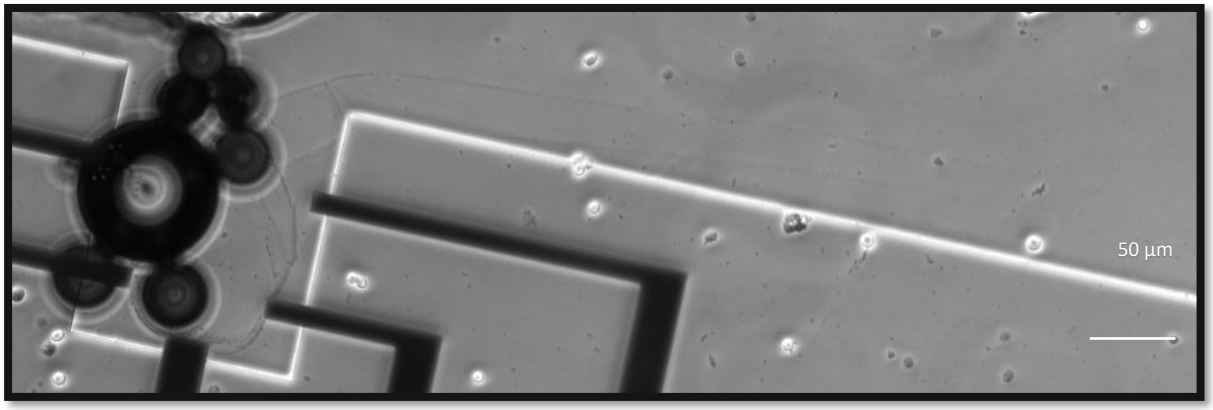

Figure 68: Microscope Image of the DEP Insertion gas introduction after 10s at an applied AC field of 20 kHz 30s later.

The cluster of cells, proteins, cell debris and staining residue rotated after a while and a few more bubbles were formed as depicted in Fig. 68.

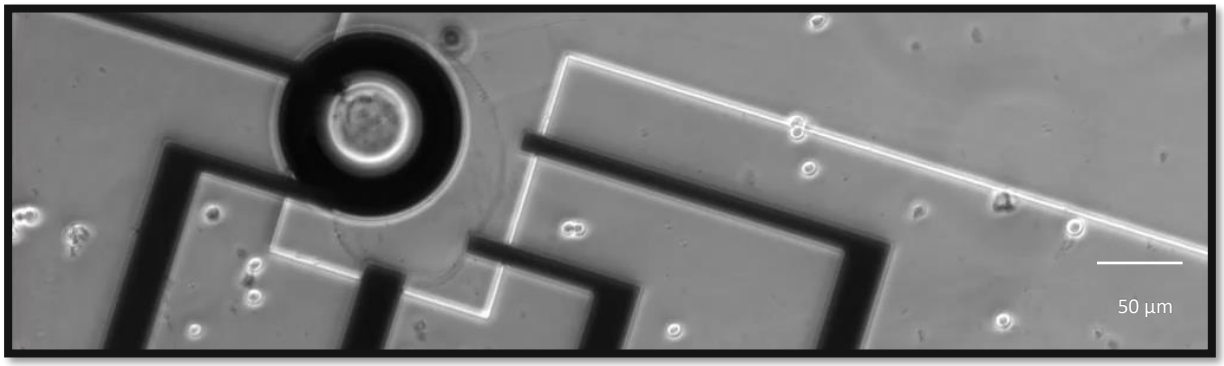

Figure 69: Microscope Image of the DEP Insertion Chip spheriodal arragment with gas inside after 10s at an applied field of 20 kHz.

Approximately 10 minutes later, a spherical arrangement began to take shape, with visible gas inside, observable in Fig. 69.

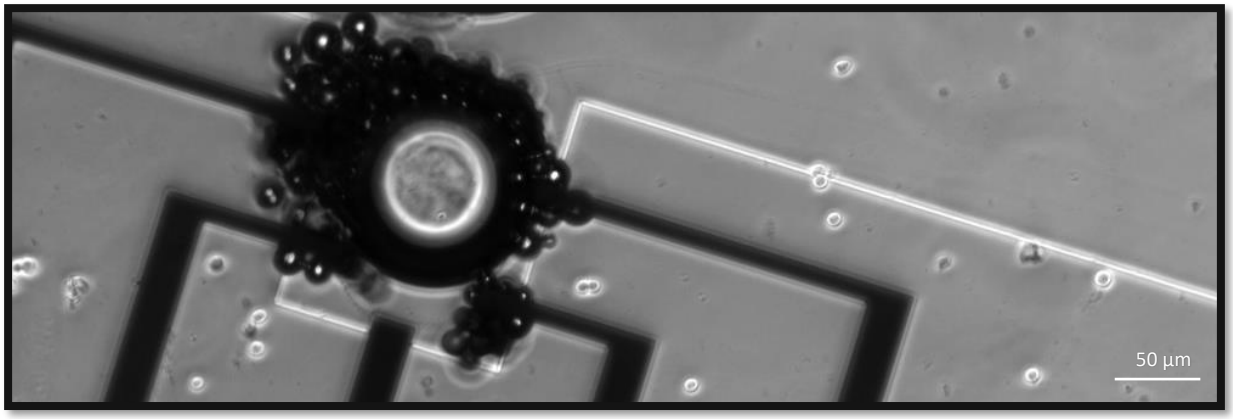

Figure 70: Microscope Image of the DEP Insertion Chip gas-cluster push by DC introduction.

By applying a DC offset of 2 V and switching the polarity of the electrode, an expulsion of bubbles occurred, as shown in Fig. 70.

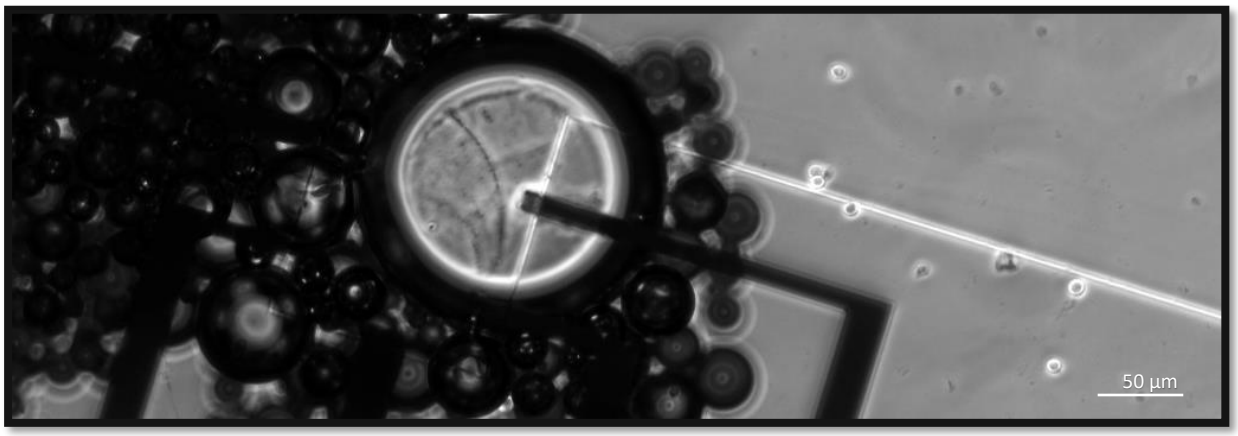

Figure 71: Microscope Image of the DEP Insertion Chip. At any AC frequency an extensive electrolysis took place.

Turning off the DC offset and examining the gas production across a voltage and frequency range of 0 to 5V and 20 kHz to 200 kHz, it was observed that gas production at any frequency above 2 V appeared. The bubbles formed rapidly, filling the channel within 10 seconds (Fig. 71). It is noteworthy that the bubble formation around the electrode finger already altered the conditions. The electrode surface was enveloped by hydrogen, oxygen, and small quantities of cell nutrition media. The electrolysis process proved challenging to replicate at AC voltages below 3 V, regardless of the frequency ranging from 20 kHz to 20 MHz, unless preceded by a DC introduction. This phenomenom was further examined the results are shown next.

6.4.3 Electrolysis and Electrode Degradation

Electrolysis interrupted many experiments and destroyed a range of electrodes.

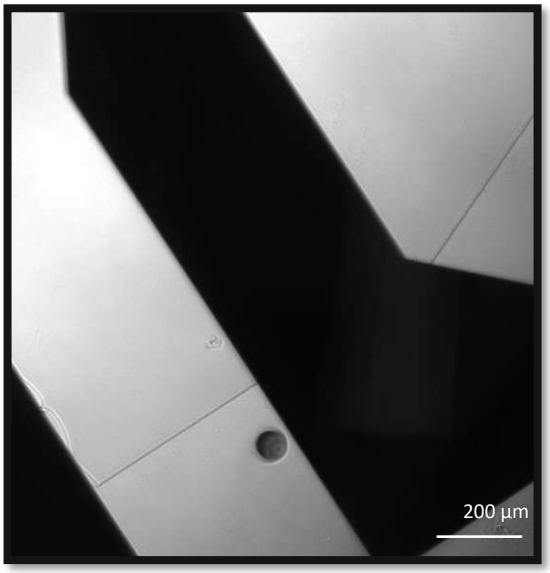

Figure 72: Microscope Image of an electrolysis Bubble

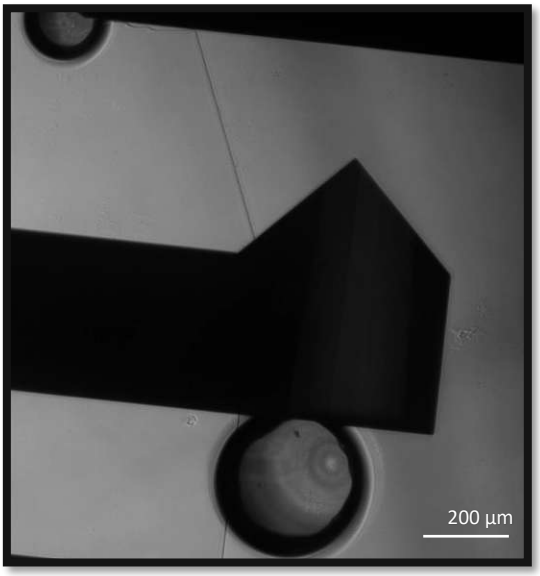

Figure 73: Microscope Image of electrolysis bubble Growth

To prevent electrolysis in further experiments, the electrical parameters of DME were examined using the DEP Diversion Chip needle structure. In Fig. 72, a minor bubble formation can be observed at a 4 V DC offset. Interestingly, the frequency and AC amplitude did not appear to have any noticeable impact on solutions without the cells above. Within 20 seconds, the gas bubble expanded to reach a diameter of 100 µm, and another bubble formed at an insulated location, visible in the left upper corner of Fig. 73.

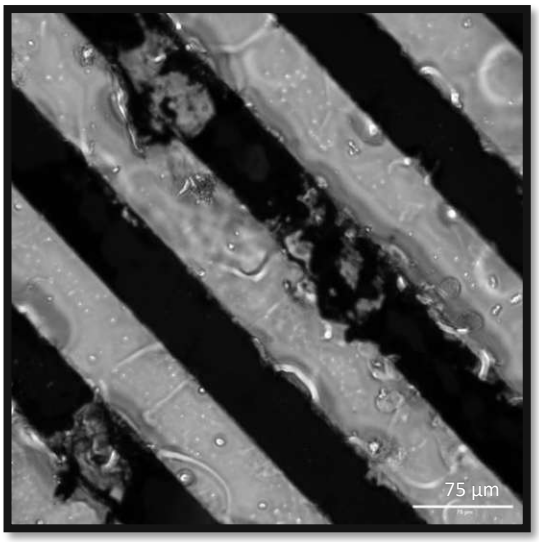

Figure 74: Microscope image of shortcut electrodegradation. The gold (black) is party torn.

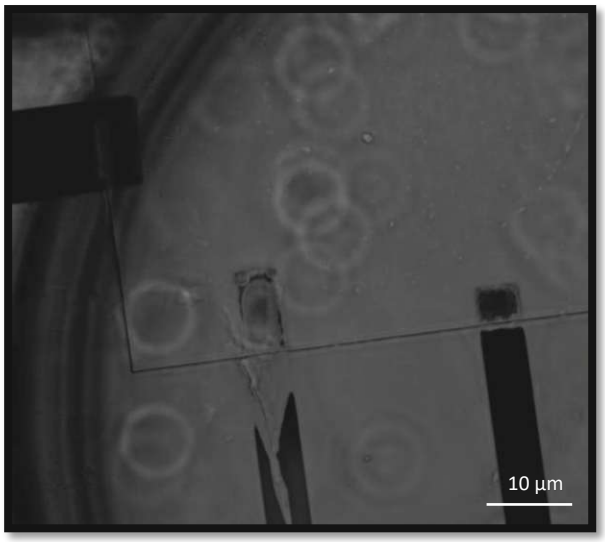

Figure 75: Microscope image of the DC input result. The degradation reached even under the insulation.

Following the completion of the experiments, the electrodes were inspected. Fig. 72 illustrates that the electrodes experienced degradation upon contact with a larger cell accumulation at 5 V AC conditions. The cell accumulation led to a circuit short and disintegration of the electrode film. It is worth noting that in cases where DC voltage was introduced, the electrodes dissolved even below the insulating layer, as shown in Fig. 75.

6.5 C-M Factor Model Fitting to Experimental Results

The results demonstrated that the previously developed model exhibits a minor variation to the experimental results. Therefore, a model fitting was undertaken. The equivalent membrane thickness for the single shell spheroid DEP model was changed from 9 nm to 90 nm. The change results in a model that fits with the experimental results.

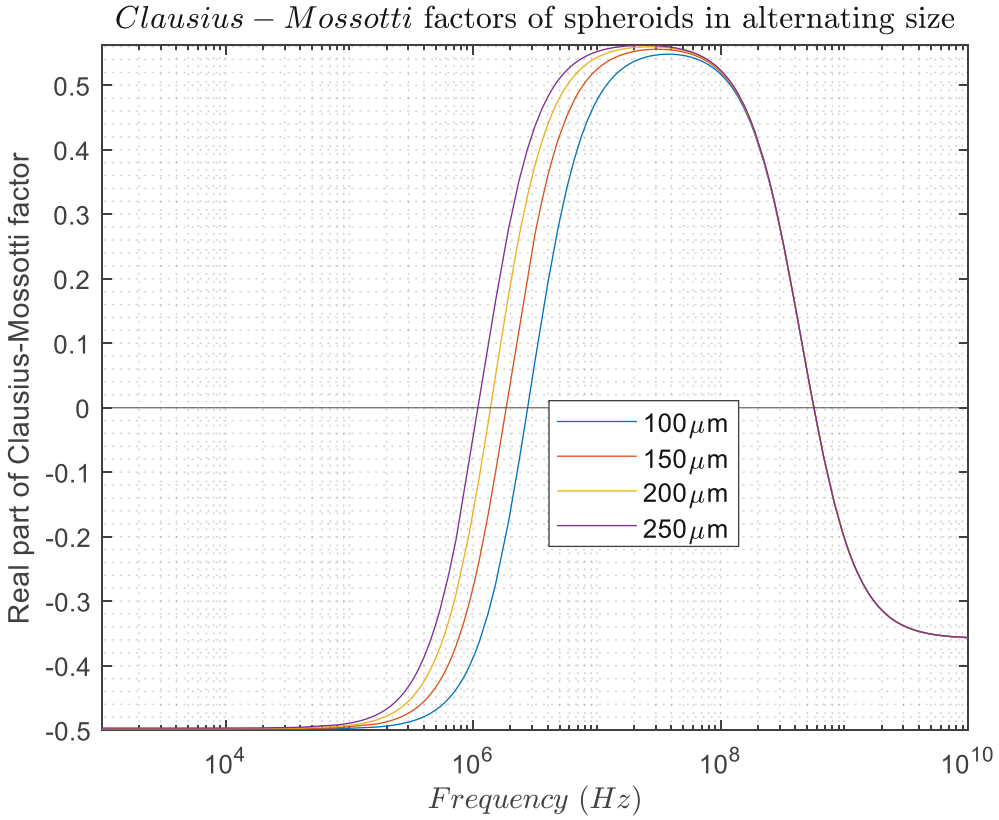

Figure 76: Graph of the resulting CM-Factor Spheroids Modell Fitting. The C-M factors are displayed for spheroids in sizes of 100 µm to 250 µm over a frequency range.

As depicted in Figure 76, the model displays the spheroid DEP behavior on a frequency range that aligns with the experimental results. The crossover frequency for a 150 µm *spheroid* is 2 MHz. Just like in 6.1 Spheroidal Analysis, the 150 µm *spheroid* in this model will not experience any translation but the 100 µm *spheroid* will experience negative DEP as depicted in Fig. 53-54. Furthermore at 20 MHz the 150µm spheroid is modelled to experience positive DEP, as depicted in Fig. 46-47. Finally, at 200 kHz all spheroids are expected to experience n-DEP.

7. Conclusion

"For the less, even as for the greater there is some deed that he may accomplish but once only; and in that deed, his heart shall rest."- J.R.R. Tolkien. The study highlighted the potential to apply DEP-based positioning on *spheroids* and cells. Electrolysis and DEP fluidic flow induction added complexity to the findings. The research encourages refining models, exploring strategies to minimize cell adhesion, and conducting comprehensive experiments to advance our understanding of DEP applications on *spheroids*. First in this chapter the spheroidal analysis evaluation indicates that rolling motion significantly influences spheroid behavior, necessitating refined models and considering fluidic effects for accurate calculations. Furthermore, the cellular analysis evaluation underscores the challenges of cell accumulation, electrolysis, and chip design complexities in achieving effective DEP-based cell manipulation. The chapter concludes by discussing the posibilities of interdigitated electrodes (IDEs) and digital microfluidics for future research.

7.1 Spheroidal Analysis Evaluation

During the spheroid trials, it was observed that rolling motion significantly accelerates the motion of the *spheroids*. This implies that the calculations in section 4.1.2 are rough guidance because they don't take rolling motion into account. It has been shown trough experimental results in section 6.4.1, when an electrode distance of 300-450 µm was used, a 10 V AC at 2 MHz was always sufficient to generate motion and position the spheroids in between the electrodes. Furthermore, the findings indicate that spheroids of varying sizes are influenced in distinct ways at alternating frequencies.

Therefore,

- **DEP has a sufficient translational effect on *spheroids*.**
- **Micro-position the *spheroids* between electrodes is possible.**
- ***Spheroid* of a certain size may be selectively influenced by DEP.**

These findings are consistent with the hypotheses stated in the introduction.

Even though size exclusiveness among the *spheroids* was achieved, both the 100 µm and 150 µm diameter *spheroids* were expected to experience positive DEP at 20 MHz and 2 MHz. The smaller spheroid exhibited no motion at 20 MHz and the 150 µm got repelled which hints at n-DEP. On the other hand, when n-DEP was expected at 200 kHz the *spheroids* were attracted positively. In this study the spheroids were modeled as large single-shell structures. The deviation in the experimental results suggest that a biophysical single shell model isn't suitable for DEP *spheroid* modulation, and a multi shell model should be developed and compared with the results of this study to develop further models. A multi shell model is proposed because the spheroid aggregates as multiple cells in overlapping layers, all with intact membranes. Because each cell is modeled as a capacitor and an AC field is employed, the capacitance of each membrane can be summed. This summation was carried out during the fitting process, aligning the final C-M factor model for *spheroids* with the study's outcomes.

A previously not considered effect is the induction of fluidic flow by DEP. Different fluidic turbulences were generated during the experiments, making it challenging to determine whether the observed DEP was responsible for the motion of the *spheroid* or the fluidic flow.

In section 6.1.1, it appears that the electric field at the edge plays a decisive role. It is important to note that the 150 nm high planar electric field generated by the 150 nm high electrodes only affects the lowest part of the 100-150 µm spheroid. The main responsive electric field, as described in section 4.2.3, is located above the electrodes. With this information further designs might not need an edge design. An opposing parallel electrode alignment with a gap between 300 to 450 µm should be suitable for repelling a 150 µm spheroid using a frequency of 20 MHz, while a 100 µm thick spheroid requires an electrode distance of 300 µm and a frequency of 2 MHz. On the other hand, to attract *spheroids* to the electrodes, a frequency of 200 kHz can be considered. However, it is important to be aware that electrolysis may occur, especially at edges. Frequencies below 20 kHz in electrode distances of 300 to 400 µm are likely to result in extensive gas production.

In summary, the evaluation of the spheroidal analysis highlights the importance of refining the model, electro-rotation measurements are not enough to model the DEP behavior of a spheroid. Even though the successfully determined frequencies can already be applied to position *spheroids*. Size exclusiveness can also be achieved. The influence of fluidic flows on DEP needs to be further examined. The location of the electric field and suitable electrode distances for different spheroid sizes should be considered for further experiments. Finally, this approach is now applicable for future chip design the frequency selection for attracting *spheroids* but must consider the possibility of electrolysis.

7.2 Cellular Analysis Evaluation

Human tumor cells are attracted by DEP at 200 kHz at 10V peak to peak in an electrode gap of 50 µm. The bigger electrode gap of 400 µm in the DEP Diversion Chip 2 resulted in no movement of human mesenchymal stem cells, which implicates that the cells got polarized and attracted towards the electric pole. But after a while the channel got plugged by a cell accumulation, which could be due to the static effects as in microfluidics this didn't occur. For reference in microfluidic, Song et al. approach had heights of 26µm[31] a lesser height than the xurography version of the DEP Diversion Chips, which had heights of 140 µm. Furthermore, at the positions where cells got stuck and accumulated, they shorted the electrodes with up to 200 mA current, destroyed the cell membranes and the electrodes**.** This clustering demonstrates the effectiveness of DEP on cells but highlights the necessity of microfluidic flow and short pulses with fine-tuned voltage amplitude to prevent the accumulation at the electrodes.

Furthermore, the microfluidic set-up experiments with cells showed that it is important to consider the pressure limitations of the chip. When using epoxy glued ports with an inner diameter of 0.5 millimeters, the maximum pressure that can be applied to the chip is approximately 200 mbar. The experiment with the DEP insertion chip showcased that at 20 kHz all cells and byproducts get attracted by the electrodes into the pocket, which led to cluster formation but also electrolysis gas production.

A major obstacle, in a lot of experiments, was that electrolysis took place. The most potential mechanism is that H_2O in the cell medium reacted to oxygen (O_2) and hydrogen (H_2). The observation of electrolysis easily occurring in the DEP insertion chip, but hardly in the Diversion Chips, raises an intriguing question regarding the underlying mechanisms and design differences between the two types of chips. The major difference between the chips might be the current density (A/cm^2). In the experiment the small opposing fingertips of the DEP Insertion Chip were activated which led to 3 A/cm^2 (20 kHz) and 8 A/cm^2 (20 MHz) at 2 V. The thermodynamic voltage at 25 °C is 1.3 V at 0.2–0.5 A/cm^2 for alkaline hydrolysis.[52] In the Diversion chip where all electrodes are in parallel, lower current densities appear. Before connecting single electrodes to the frequency generator, electrolysis should be considered. The output frequency should be at least 200 kHz, and DC offset should be avoided to avoid electrolysis.

7.3 Further Refinements

To address the issue of cells falling in-between the electrodes, a flip-chip design is proposed. This involves drilling holes in the glass wafer where the MEA is microfabricated. By flipping the chips, cells can slide on the glass surface, reducing the risk of shortages caused by cell clusters and improving overall chip functionality. To ensure reliable electrical connections, the electrodes on the top side of the chip can be connected to a 1mm flat printed circuit board (PCB) using pogo pins. This approach simplifies the connection process, replaces the high amount of cable, and opens the possibility of controlled electrode activation via a multiplexer.

In many cases, cells and *spheroids* tended to adhere to the electrodes and glass surfaces, making their removal challenging and giving misleads on DEP effectiveness. To address this issue, strategies to minimize cell adhesion must be explored. Modifying the chip glass and electrode surface will sooner or later become crucial to maintaining cell viability and improving DEP accuracy. By employing appropriate surface treatments or coatings, the biocompatibility of the chip can be enhanced, and adhesiveness of cells and *spheroids* reduced.

While Xurography offers a fast fabrication process, its precision may be compromised, and the minimum achievable channel size using the American Silhouette Plotter is limited to 0.5 mm. It is essential to carefully assess the trade-off between fabrication speed and precision when selecting Xurography as the fabrication technique. Its precision could be improved by utilizing a mask aligner. PDMS blocks offer the advantage of accommodating more complex geometries. However, surface bonding PDMS to glass through plasma treatment can be challenging because it requires a mold with low surface roughness.

7.4 Outlook

To improve reproducibility and deepen the understanding of *spheroid* DEP in the short term, it is imperative to conduct additional experiments. By systematically varying the electrode arrangements, voltages, and frequencies a comprehensive table or database can be developed, correlating *spheroid* reactions with specific experimental conditions. This information will provide valuable insights into the behavior of *spheroids* and opens the possibility of improving the model in section 6.1.1 and its fitting in section 6.5. Furthermore, the electrodes at the in- and outlet of the DEP Insertion Chip can be used for electro-rotation measurements to validate and further improve *spheroid* DEP models. Finally, before DEP is going to be used in *spheroid* or cell position or isolation for genetic analyses, the effects of the electric field on the transcriptome should be investigated and taken into consideration.

Returning to the starting point to something that had previously been presented solely as a measurement tool: IDEs. Interdigitated electrodes are integrated into the MEA on the Diversion Chips and electrowetting-on-dielectric (EWOD) devices. Digital microfluidics have already a wide range of applications from sample preparation to DNA Assays.[53] The recent breakthrough in AI and the signing of the FDA Modernization Act 2.0 are steps into fully automated high throughput biological analysis of *spheroids* and *organoids* in digital microfluidic.

8. Bibliography

1. Mauro, A. Dielectrophoresis: The Behavior of Neutral Matter in Nonuniform Electric Fields. Herbert A. Pohl. *Q Rev Biol* **55**, 68–69 (1980).

2. Pamme, N. Continuous flow separations in microfluidic devices. *Lab on a Chip* vol. 7 1644–1659 Preprint at https://doi.org/10.1039/b712784g (2007).

3. Iyer, V., Yang, Z., Ko, J., Weissleder, R. & Issadore, D. Advancing microfluidic diagnostic chips into clinical use: a review of current challenges and opportunities. *Lab on a Chip* vol. 22 3110–3121 Preprint at https://doi.org/10.1039/d2lc00024e (2022).

4. Scalise, M. *et al.* From spheroids to organoids: The next generation of model systems of human cardiac regeneration in a dish. *International Journal of Molecular Sciences* vol. 22 Preprint at https://doi.org/10.3390/ijms222413180 (2021).

5. Zhao, Z. *et al.* Organoids. *Nature Reviews Methods Primers* **2**, (2022).

6. Leung, C. M. *et al.* A guide to the organ-on-a-chip. *Nature Reviews Methods Primers* vol. 2 Preprint at https://doi.org/10.1038/s43586-022-00118-6 (2022).

7. Park, S. E., Georgescu, A. & Huh, D. Organoids-on-a-chip. *Science* vol. 364 960–965 Preprint at https://doi.org/10.1126/science.aaw7894 (2019).

8. Spitz, S. *et al.* Development of a multi-sensor integrated midbrain organoid-on-a-chip platform for studying Parkinson's disease. doi:10.1101/2022.08.19.504522.

9. Thomas, C. A., Springer', P. A., Loeb, G. E., Berwald-Netters, Y. & Okunj, L. M. *A MINIATURE MICROELECTRODE ARRAY TO MONITOR THE BIOELECTRIC ACTIVITY OF CULTURED CELLS*. *Experimental Cell Research* vol. 74 (1972).

10. Charwat, V. *et al.* Monitoring dynamic interactions of tumor cells with tissue and immune cells in a lab-on-a-chip. *Anal Chem* **85**, 11471–11478 (2013).

11. Park, Y. *et al. Park et al A P P L I E D S C I E N C E S A N D E N G I N E E R I N G Three-dimensional, multifunctional neural interfaces for cortical spheroids and engineered assembloids*. *Sci. Adv* vol. 7 (2021).

12. Huang, Q. *et al. Shell microelectrode arrays (MEAs) for brain organoids*. *Sci. Adv* vol. 8 (2022).

13. Schuster, B. *et al.* Automated microfluidic platform for dynamic and combinatorial drug screening of tumor organoids. *Nat Commun* **11**, (2020).

14. Castellarnau, M., Errachid, A., Madrid, C., Juárez, A. & Samitier, J. Dielectrophoresis as a tool to characterize and differentiate isogenic mutants of Escherichia coli. *Biophys J* **91**, 3937–3945 (2006).

15. Kang, Y., Li, D., Kalams, S. A. & Eid, J. E. DC-Dielectrophoretic separation of biological cells by size. *Biomed Microdevices* **10**, 243–249 (2008).

16. Jones, T. B. *Electromechanics of Particles*. (Cambridge University Press, 1995). doi:10.1017/CBO9780511574498.

17. Lou, Y. R. & Leung, A. W. Next generation organoids for biomedical research and applications. *Biotechnology Advances* vol. 36 132–149 Preprint at https://doi.org/10.1016/j.biotechadv.2017.10.005 (2018).

18. Velasco, V., Shariati, S. A. & Esfandyarpour, R. Microtechnology-based methods for organoid models. *Microsystems and Nanoengineering* vol. 6 Preprint at https://doi.org/10.1038/s41378-020-00185-3 (2020).

19. Ren, T., Steiger, W., Chen, P., Ovsianikov, A. & Demirci, U. Enhancing cell packing in buckyballs by acoustofluidic activation. *Biofabrication* **12**, (2020).

20. Jin, H. J., Cho, Y. H., Gu, J. M., Kim, J. & Oh, Y. S. A multicellular spheroid formation and extraction chip using removable cell trapping barriers. *Lab Chip* **11**, 115–119 (2011).

21. Suehiro, J. & Pethig, R. *The dielectrophoretic movement and positioning of a biological cell using a three-dimensional grid electrode system*. *Journal of Physics D: Applied* vol. 31 (1998).

22. Lee, A. P., Aghaamoo, M., Adams, T. N. G. & Flanagan, L. A. It's Electric: When Technology Gives a Boost to Stem Cell Science. *Current Stem Cell Reports* vol. 4 116–126 Preprint at https://doi.org/10.1007/s40778-018-0124-x (2018).

23. Sexton, B. A., Feltis, B. N. & Davis, T. J. Characterisation of gold surface plasmon resonance sensor substrates. *Sens Actuators A Phys* **141**, 471–475 (2008).

24. Arshavsky-Graham, S. & Segal, E. Lab-on-a-Chip Devices for Point-of-Care Medical Diagnostics. in 247–265 (2020). doi:10.1007/10_2020_127.

25. Bastian Rapp. *Microfluidics: Modeling, Mechanics and Mathematics*. vol. 1 (ELSEVIER, 2016).

26. Han, J. J. FDA Modernization Act 2.0 allows for alternatives to animal testing. *Artif Organs* **47**, 449–450 (2023).

27. Ergir, E., Bachmann, B., Redl, H., Forte, G. & Ertl, P. Small force, big impact: Next generation organ-on-a-chip systems incorporating biomechanical cues. *Frontiers in Physiology* vol. 9 Preprint at https://doi.org/10.3389/fphys.2018.01417 (2018).

28. Abaci, H. E. & Shuler, M. L. Human-on-a-chip design strategies and principles for physiologically based pharmacokinetics/pharmacodynamics modeling. *Integrative Biology (United Kingdom)* **7**, 383–391 (2015).

29. Spitz, S., Jordan, C., Wanzenboeck, H. D. & Haddadi, B. Microvasculature-on-a-Chip: Bridging the interstitial blood-lymph interface via mechanobiological stimuli Minimal Invasive Liquid

Lung (MILL) View project Doctoral College 'CO2Refinery' View project. (2021) doi:10.1101/2021.04.08.438936.

30. Giesler, J., Weirauch, L., Thöming, J., Baune, M. & Pesch, G. R. Separating microparticles by material and size using dielectrophoretic chromatography with frequency modulation. *Sci Rep* **11**, (2021).

31. Song, H. *et al.* Continuous-flow sorting of stem cells and differentiation products based on dielectrophoresis. *Lab Chip* **15**, 1320–1328 (2015).

32. Lee, D., Hwang, B. & Kim, B. The potential of a dielectrophoresis activated cell sorter (DACS) as a next generation cell sorter. *Micro and Nano Systems Letters* vol. 4 Preprint at https://doi.org/10.1186/s40486-016-0028-4 (2016).

33. Mathew, B., Alazzam, A., Khashan, S. & Abutayeh, M. Lab-on-chip for liquid biopsy (LoC-LB) based on dielectrophoresis. *Talanta* **164**, 608–611 (2017).

34. Trainito, C. I., Bayart, E., Subra, F., Français, O. & Le Pioufle, B. The Electrorotation as a Tool to Monitor the Dielectric Properties of Spheroid During the Permeabilization. *Journal of Membrane Biology* **249**, 593–600 (2016).

35. Descamps, L., Roy, D. Le & Deman, A. L. Microfluidic-Based Technologies for CTC Isolation: A Review of 10 Years of Intense Efforts towards Liquid Biopsy. *International Journal of Molecular Sciences* vol. 23 Preprint at https://doi.org/10.3390/ijms23041981 (2022).

36. Zhuang, J. *et al.* Recent advances in integrated microfluidics for liquid biopsies and future directions. *Biosensors and Bioelectronics* vol. 217 Preprint at https://doi.org/10.1016/j.bios.2022.114715 (2022).

37. Eslami-S, Z., Cortés-Hernández, L. E. & Alix-Panabières, C. Epithelial Cell Adhesion Molecule: An Anchor to Isolate Clinically Relevant Circulating Tumor Cells. *Cells* vol. 9 Preprint at https://doi.org/10.3390/cells9081836 (2020).

38. Alves, J. M. *et al.* Comparative analysis of capture methods for genomic profiling of circulating tumor cells in colorectal cancer. *Genomics* **114**, (2022).

39. Miller, M. C., Robinson, P. S., Wagner, C. & O'Shannessy, D. J. The Parsortix™ Cell Separation System—A versatile liquid biopsy platform. *Cytometry Part A* **93**, 1234–1239 (2018).

40. Shim, S. *et al.* Antibody-independent isolation of circulating tumor cells by continuous-flow dielectrophoresis. *Biomicrofluidics* **7**, (2013).

41. Gascoyne, P. R. C. & Shim, S. Isolation of circulating tumor cells by dielectrophoresis. *Cancers (Basel)* **6**, 545–579 (2014).

42. COPAS Union Biometrica, Inc. Union Biometrica BioSorter Platform Overview. *https://www.unionbio.com/biosorter/* (2023).

43. Zhao, S. *et al.* ElectroTaxis-on-a-Chip (ETC): An integrated quantitative high-throughput screening platform for electrical field-directed cell migration. *Lab Chip* **14**, 4398–4405 (2014).

44. Berthier, J. Introduction to Liquid Dielectrophoresis. in *Micro-Drops and Digital Microfluidics* 303–324 (Elsevier, 2013). doi:10.1016/b978-1-4557-2550-2.00006-7.

45. Adams, T. N. G., Turner, P. A., Janorkar, A. V., Zhao, F. & Minerick, A. R. Characterizing the dielectric properties of human mesenchymal stem cells and the effects of charged elastin-like polypeptide copolymer treatment. *Biomicrofluidics* **8**, (2014).

46. Lang, Q. *et al.* AC Electrothermal Circulatory Pumping Chip for Cell Culture. *ACS Appl Mater Interfaces* **7**, 26792–26801 (2015).

47. Elveflow Elvesys. OB1 MK4 Microfluidic Flow Controller. *https://www.elveflow.com/microfluidic-products/microfluidics-flow-control-systems/ob1-pressure-controller/* (2023).

48. Eilenberger, C. *et al.* A Microfluidic Multisize Spheroid Array for Multiparametric Screening of Anticancer Drugs and Blood–Brain Barrier Transport Properties. *Advanced Science* **8**, 2004856 (2021).

49. Jungreuthmayer, C., Birnbaumer, G. M., Zanghellini, J. & Ertl, P. 3D numerical simulation of a lab-on-a-chip-increasing measurement sensitivity of interdigitated capacitors by passivation optimization. *Lab Chip* **11**, 1318–1325 (2011).

50. Shabestani Monfared, G., Ertl, P. & Rothbauer, M. An on-chip wound healing assay fabricated by xurography for evaluation of dermal fibroblast cell migration and wound closure. *Sci Rep* **10**, (2020).

51. Adhesive Research. *Product Information Sheet ARcare® 90106NB*. https://www.adhesivesresearch.com/wp-content/uploads/2020/06/ARcare%C2%AE-90106NB-Product-Information-Sheet-2.pdf (2023).

52. Millet, P. & Grigoriev, S. Water Electrolysis Technologies. in *Renewable Hydrogen Technologies: Production, Purification, Storage, Applications and Safety* 19–41 (Elsevier B.V., 2013). doi:10.1016/B978-0-444-56352-1.00002-7.

53. Barman, S. R. *et al.* Electrowetting-on-dielectric (EWOD): Current perspectives and applications in ensuring food safety. *Journal of Food and Drug Analysis* vol. 28 595–621 Preprint at https://doi.org/10.38212/2224-6614.1239 (2020).

9. List of Figures

10. List of Tables

11. List of Abbreviations

Abbreviation	Full Form
AC	Alternating Current
ADC	Analog-Digital-Converter
BNC	Bayonet Neill-Concelman
CAD	Computer-Aided Design
CFD	Computational Fluid Dynamics
C-M	Clausius-Mossotti
CTC	Circulating Tumor Cells
DAPI	4',6-Diamidino-2-Phenylindole
DC	Direct Current
DEP	Dielectrophoresis
n- p-	Negative / Positive
DEP-FFF	Dielectrophoretic Field-Flow-Fractionation
DME	Dulbecco's Modified Eagle Medium
EpCAM	Epithelial Cell Adhesion Molecule
Eq	Equation
EWOD	Electro-Wetting-on-Digital-Device
FACS	Fluorescence-Activated Cell Sorting
HMSCs	Human Mesenchymal Stem Cells
h	Hour
ISO	International Organization for Standardization
MEA	Multi Electrode Arrays
PBS	Phosphate-Buffered Saline
PDMS	Polydimethylsiloxane
PETG	Polyethylene Terephthalate Glycol
PECVD	Plasma-Enhanced Chemical Vapor Deposition
PLA	Polylactic Acid
RIE	Reactive Ion Etching
SiN	Silicon Nitride
UV	Ultraviolet

12. Declaration of AI-Integration in Thesis

I, Max Schimpf, hereby declare that in the preparation of this diploma thesis titled "Dielectrophoresis of human tumor spheroids," I have utilized artificial intelligence (AI) technologies to enhance and augment various components of this research work.

I have harnessed AI in the following ways:

Abstract Illustrations: (Dall-E 2, GPT-3, OpenAI)

AI has been instrumental in generating abstract illustrations that visually represent complex concepts related to spheroids and organoids (Fig. 1). These visual representations facilitate the understanding of intricate ideas, aiding readers in grasping the fundamental principles underlying this research.

Text Rewriting: (ChatGPT and Grammarly, GPT-4 API, OpenAI)

The integration of AI in the text rewriting process has allowed for the refinement and optimization of written content fully automated in the background. By utilizing the self-sustaining AI algorithms, I have enhanced the clarity, coherence, and readability of the thesis, ensuring that the conveyed information is effectively communicated to the audience.

Maintaining a Coherent Thread: (ChatGPT, GPT 4, OpenAI)

Throughout the thesis, I have employed AI to analyze thematic connections and ensure a consistent red thread that ties together different sections seamlessly. This strategic application of AI has aided in maintaining a logical progression of ideas, enhancing the overall coherence and flow of the thesis.

Research: (Bart \ Bing (GPT4), Google \ Microsoft)

AI has helped me revolutionize research by swiftly and accurately identifying pertinent academic papers amidst the vast sea of information, streamlining literature reviews, and enabling researchers to access crucial knowledge efficiently.

Information Extraction (Petal.org)

I hereby declare the utilization of AI to extract intricate information from research papers, followed by insightful discussions with the AI, fostering a symbiotic exchange that enriched the depth and breadth of my research endeavors.

I acknowledge that while AI technologies have significantly contributed to the enhancement of various components of this research work, they have been employed as tools to complement and amplify my expertise in the field of biomedical engineering. I've chosen transparency over covering the usage of AI with tools like undetectable.ai to uphold the authenticity. Rigorous review and manual refinement were conducted to ensure the accuracy and relevance of the AI-generated content, thereby upholding the integrity of this thesis.

In conclusion, the integration of AI technologies in this thesis underscores my commitment to academic rigor. By blending my expertise with AI capabilities, I have strived to create a comprehensive research work that advances our understanding of the dielectrophoresis of spheroids.

13. Appendix

The appendix includes the script for calculating the Clausius-Mossotti factor, which is a vital element in the thesis due to its fundamental role and the detailed step by step clean room processes with all parameter.

13.1 Clausius Mossotti Factor Code

The code utilized the MATLAB Toolbox Symbolic Math. The fitting is described within the code.

```
%% Simulation of a spheroids Clausius Mossotti factor and Movement based on
'The Electrorotation as a Tool to Monitor the Dielectric Properties of Spheroid
During the Permeabilization' %%
%% Clear Workspace
preamble;
%
%% Constants:
%% Physical Constants
epsi_0 = 8.854e-12;  % Field constant [C/Vm]
%
%% measured by (C. I. Trainito et al 2016):
% Inner layer
epsi_in0 = 16.7; %(relative)
sigma_in0 = 0.5; %(S/m)
% Outer layer
epsi_out0 = 4.9; %(relative)
sigma_out0 = 1.5e-7; %(S/m)
%% Medium
sigma_med0 = 0.1; %(S/m)
epsi_med0 = 80; %(relative)
% Geometrical factors
e0 = 90e-9; % thickness of the equivalent membrane(usually 9 nm) ! FITTING to 90!!
%% XCROSS ************************************************************************
x_cross=20*10^6;
%
%% Variables
syms w
syms epsi_in sigma_in epsi_out sigma_out epsi_med sigma_med
syms R_sph e
%
%% Star-Transformation
epsi_in_star(w) = epsi_in - 1i*(sigma_in/(epsi_0*w));
epsi_out_star(w) = epsi_out - 1i*(sigma_out/(epsi_0*w));
epsi_med_star(w) = epsi_med - 1i*(sigma_med/(epsi_0*w));
%% Average complex permittivity of the spheroid, stands as (Huang et al. 1992)
epsi_sph_star(w) = epsi_out_star(w)*((((R_sph/(R_sph-e))^3+2*((epsi_in_star-
epsi_out_star)/(epsi_in_star+2*epsi_out_star)))/((R_sph/(R_sph-e))^3-
((epsi_in_star-epsi_out_star)/(epsi_in_star+2*epsi_out_star)))));
%
%% Clausius Mossotti factor
Chi(w) = (epsi_sph_star-epsi_med_star)/(epsi_sph_star+2*epsi_med_star);
%
%% alternating sizes
for n=1:4
R_sph0 = (100+50*(n-1))*10^-6; % Radius of Spheroid
%% Substitution and imaginary to real transfer
K(w) = subs(Chi(w),{epsi_in sigma_in epsi_out sigma_out epsi_med sigma_med R_sph
e},{epsi_in0 sigma_in0 epsi_out0 sigma_out0 epsi_med0 sigma_med0 R_sph0 e0});
```

```
realK(w) = real(K(w));
%
%% Plot
figure(1)
Kfun=matlabFunction(realK);
p(n)=fplot(@(w) Kfun(w),[10^3 10^10]);
hold on
set(gca,'XScale','log')
end
set(gca,'XScale','log')
%% Visualize figure 1
figure(1)
str = '$Clausius-Mossotti$ factors of spheroids in alternating size';
title(str,'Interpreter','latex','FontSize',12)
xlabel('$Frequency$ $(Hz)$','Interpreter','latex')
ylabel('Real part of Clausius-Mossotti factor')
legend([p(1),p(2),p(3),p(4)],'100{\mu}m'
,'150{\mu}m','200{\mu}m','250{\mu}m','Location','best', fontsize = 10)
grid minor
% Find perfect Frequency
yline(0,'HandleVisibility','off')
%
%% DEP Force Calculation
%% Electrical components:
U = 20; % Voltage between the electrodes [V]
%% Particle information:
m = 1e-6;% Mass of Particle (1mg)
r = 100e-6;
%% Variables
syms t % Bewegungszeit (seconds)
%% Konstanten
epsi0 = 8.854e-12;  % Feldkonstante [C/Vm]
%% Calculation %%
for n = 1:5
    % different electrode distances
    d = (250+50*(n-1))*10^-6; % [micrometer]
    grad_E_rms = U/d;
    %
%% Compute Force DEP
F = 2*pi*r^3*epsi0*80*Cmf(3)*grad_E_rms^2;
%% Compute acceleration
a = F/m;
%% Compute and plot distance at best freq.
figure(2)
Distance(t) = -a/2*(t^2)*10^6; % [µm]
fd = matlabFunction(Distance);
pm(n) = fplot(@(t) fd(t),[0 60]);
hold on
end
xlabel('time $[s]$',Interpreter='latex')
ylabel('Distance traveled [µm]')
legend('250{\mu}m','300{\mu}m','350{\mu}m','400{\mu}m','450{\mu}m','Location','bes
t', fontsize = 10)
title('By dielectrophoresis moved organoids','fontsize',12)
subtitle('in alternating electrode distances',fontsize = 10)
grid on
yline(-200, HandleVisibility="off")
% Set the desired y-axis limits
yLimits = [-100, 0];  % Your desired lower and upper limits
ylim(yLimits);
```

13.2 Step-by-Step Clean-Room Processes

The provided instructions outline the detailed step-by-step processes for different tasks within the clean room environment of the center for micro and nano structuring, including sputtering, photolithography, lift-off, PECVD (Plasma-Enhanced Chemical Vapor Deposition), and RIE (Reactive Ion Etching). These processes are commonly employed in microfabrication and semiconductor manufacturing. They require a systematic approach to maintain precision and reproducibility. The processes are bounded to the machines and guidelines of the technical university so some steps may vary at other machines.

Sputtering:

1. **Logbook Entry**: Record process details.
2. **Argon On**: Activate argon supply at the backside of the machine.
3. **Vent Chamber**: Ensure proper chamber venting.
4. **Displace Substitutes**: Remove substitutes and organize.
5. **Wafer Placement**: Place wafer and establish vacuum.
6. **Target Conditioning**: Condition target with Ti for 60s: P = 50W, p base = 2 * 10^-5, p work = 8 * 10^-3.
7. **Silver Deposition**: Deposit Ag 3 times for 60s each: P = 50W, p base = 2 * 10^-5, p work = 8 * 10^-3 (nominal deposit height = 10nm).

After Sputtering:

1. **Reposition Substitutes**: Return substitutes in original order.
2. **Close Lid**: Securely close chamber lid.
3. **Apply Vacuum**: Create vacuum in chamber.
4. **Pump and Arrow**: Wait for pump to reach 250Hz, then press double arrow button.
5. **Argon Pump Off**: Turn off argon pump at the backside.

Photolithography - Image Reversal:

1. **Logbook Entry**: Document process details.
2. **Air Pressure and Argon**: Activate air pressure and argon supply.
3. **UV Lamp**: Power on UV lamp and wait for self-check.
4. **Lamp On**: Turn on lamp.
5. **Preheat**: Preheat for 30 minutes.
6. **Heat-plates**: Activate heat-plates at 100°C and 120°C.
7. **Light Intensity Check**: Measure light intensity with photodiode; adjust exposure time if needed.
8. **Prepare Photoresist**: Gather AZ 5214 photoresist and developer (MIF).
9. **Wafer Preparation**: Place wafer on spin coater, activate vacuum, load recipe.
10. **Spin Coating**: Spin coat with acceleration: 500rpm/s, max velocity: 3500rpm, duration: 35s.
11. **Soft Bake**: Place wafer on 100°C heat-plate for 60s.
12. **UV Exposure**: Expose wafer using UV lamp and mask.
13. **Mask Alignment**: Align wafer edges with mask.
14. **Exposure**: Expose for calculated time.
15. **Hard Bake**: Place on 120°C heat-plate for 60s.
16. **Flood Exposure**: Expose without mask for full dissolution.
17. **Development**: Develop for 75s - 90s in MIF Developer.

18. **Rinse and Dry**: Rinse in Deionized water and dry.

After Photolithography:

1. **Turn Off**: Deactivate heat-plates, spin coater, UV lamp (maintain air pressure and argon for cooling).
2. **Clean Equipment**: Thoroughly clean spin coater.
3. **Restock Materials**: Return AZ 5214 and MIF Developer to storage.
4. **Turn Off UV Lamp**: After cooling down, turn off air pressure and argon supply for UV lamp.

Lift-Off:

1. **Gold Sputtering**: Sputter gold onto prepared sample.
2. **Power On Bench**: Activate bench equipment at full power.
3. **Prepare Flasks**: Fill flasks with acetone and isopropanol.
4. **Ultrasonic Bath**: Place sample in acetone ultrasonic bath for 3 min.
5. **Lift-Off Process**: Gently lift off photoresist along with gold using a pipette.
6. **Transfer Sample**: Transfer to isopropanol, avoid acetone drying.
7. **Expelled Particle Solution**: Pass solution through cloth in rinse.
8. **Rinse and Empty**: Rinse sample and empty rinse via bench button.

PECVD - Si3N4 Passivation:

1. **Logbook Entry**: Document PECVD process details.
2. **Loadlock Preparation**: Prepare loadlock for process.
3. **Parameter Entry**: Cylinder pressure 1kTOR, 280°C, 87.5% [SiH4 SiNH3], RF 9.2 nm/s CVD Plasma W=20.
4. **Grid Paper Recording**: Note bridge pressures on grid paper.
5. **Sample Loading**: Insert sample into loadlock and evacuate.
6. **Recipe Load and Run**: Load recipe, adjust settings, initiate process.

RIE - Reactive Ion Etching:

1. **Logbook Entry**: Document RIE process details.
2. **Cooling Activation**: Turn on machine cooling.
3. **Pressure Recording**: Record pressures inside bridge on grid paper.
4. **Initial Checks**: Check C- concentration and chamber temperature.
5. **Loadlock Venting**: Vent loadlock.
6. **Recipe Loading**: Load etching recipe for desired duration.
7. **Sample Insertion**: Insert sample, ensure stability, proceed.

After RIE - Clean Process:

1. **Clean Process**: Execute cleaning process at 60°C.
2. **Recipe Loading**: Load chamber cleaning recipe.
3. **Step Duration Edit**: Adjust step duration for sum of etches.
4. **Temperature Check**: Wait for stable temperature, then run process.